Dissertation

Supramolecular interactions as an effective tool for fabrication of stimuli-responsive architectures and sensors

Miroslava Čonková

Supervisor: Prof. dr hab. Artur R. Stefankiewicz

The work was carried out in the Laboratory of Functional Nanostructures

Faculty of Chemistry/Center of Advanced Technology

University of Adam Mickiewicz in Poznań

Poznań 2023

„I became insane, with long intervals of horrible sanity."

— Edgar Allan Poe

Acknowledgments

I would like to express my sincere gratitude to **Professor dr hab. Artur R. Stefankiewicz** for his scientific supervision, commitment to my research, substantive guidance, and help throughout my doctoral studies.

I would like to thank the **entire team of the Functional Nanostructures Laboratory** for several years of cooperation, for daily scientific discussions and interesting conversations inside and outside of the laboratory. My thanks go especially to Filip Perlitius, Anna Brzechwa-Chodzyńska, Piotr Cecot and Marcin Konopka.

I would like to thank all our **collaborators from the Université de Strasbourg** for their professional and fruitful collaboration.

I would like to especially thank **dr Łukasz Majchrzycki** for very interesting and rewarding conversations and fruitful collaboration.

I wish to express my sincere thanks to **Professor Samori and visiting Professor Ciesielski** for welcoming me to the Institute of Supramolecular Science and Engineering (Université de Strasbourg) and **Professor Tiefenbacher** for a very warm welcome to the University of Basel, on my internships.

Last but not least I would like to thank **my family and my closest friends** especially Patrik and Sylwia for always lending me a helping hand, always being there for me and keeping me strong and as sane as possible during the whole doctoral study and during writing this thesis.

Table of Contents

Scientific achievements

Publications in international journals

- **included in the Ph.D. thesis**

A1. Miroslava Čonková, Wojciech Drożdż, Zygmunt Miłosz, Piotr Cecot, Jack Harrowfield, Mikołaj Lewandowski, Artur R. Stefankiewicz* *Influencing prototropy by metal ion coordination: supramolecular transformation of a dynamer into a Zn-based toroidal species,* Journal of Materials Chemistry C, **2021**, *9*, 3065-3069.
IF = 7.393

A2. Miroslava Čonková#, Verónica Montez-Garcia#, Marcin Konopka, Artur Cieselski*, Paolo Samori*, Artur R. Stefankiewicz* *Schiff base caped gold nanoparticles for transition metal cations sensing in organic media*, Chemical Communications, **2022**, *58 (38)*, 5773-5776.
IF = 6.065

- **not included in the Ph.D. thesis**

A3. Filip Perlitius, Anna Walczak, Miroslava Čonková, Grzegorz Markiewicz, Jack Harrowfield, Artur R. Stefankiewicz* *Dimeric capsule vs. columnar polymer: structural factors determining the aggregation behavior of amino acid-functionalized BTA derivatives in solution and in the solid-state*, Journal of Molecular Liquids, **2022**, *367,* 120511.
IF = 6.633

* corresponding author
# these authors contributed equally
impact factor from the year of publishing, source: Journal Citation Reports

Contributions to international conferences

- **oral communications**

1. „From single molecule to responsive aggregate: multiresponsive photoswitch in non-polar solvent“
   Solutions in Chemistry 2022
   8-11th November 2022, Sveti Martin na Muri, Croatia

- **poster presentations**

2. „Schiff base caped gold nanoparticles for transition metal cations sensing in organic media”
   44th Conference on Coordination Chemistry 2022
   28th August-2nd September 2022, Rimini, Italy

3. „From single molecule to responsive aggregate: multiresponsive photoswitch in chlorinated solvent“
   22nd Tetrahedron Symposium 2022
   28th June-1st July 2022, Lisbon, Portugal

4. „Influencing prototropy by metal ion coordination: supramolecular transformation of a dynamer into a Zn-based toroidal species”
   14th International Symposium on Macrocyclic and Supramolecular Chemistry
   2-6th June 2019, Lecce, Italy

5. „Synthesis of a new generation of bio-inspired and multifunctional supramolecular nanocapsules for use in the deactivation of toxic substances“
   NanoTech Poland 2018
   6-9th June, Poznań, Poland

6. „Fully reversible multi-stimuli-responsive switch between dynamer and metallodynamer“
   Supramolecular Chemistry @ work – Supr@Lyon 2018
   12-14th December Lyon, France

7. „Stereoselective synthesis of an advanced intermediate of clavaminol A and homoclavaminol A“
   Advances in Organic Chemistry 2016
   4-7th September 2016, Smolenice, Slovakia

Contribution to scientific grants

1. **Principal Investigator** Minigrant for PhD students, Adam Mickiewicz University in Poznań 017/02/SNŚ/0012: „Flexible covalent capsules: olefin metathesis leading to adaptable confined spaces”.
2. **Investigator** LIDER/024/391/L-5/13/NCBR/2014: Synthesis, physicochemical properties and application of dynamic metal-organic frameworks
3. **Investigator** SONATA-BIS/UMO-2018/30/E/ST5/00032: Self-associating porous capsules as multifunctional nanomaterials.
4. **Fellow** of the project No. POWR.03.02.00-00-I032/16: „Środowiskowe interdyscyplinarne studia doktoranckie w zakresie nanotechnologii”.

Internships

University of Basel, Switzerland

Konrad Tiefenbacher Group

05-06/2022 (2 months)

Supramolecular Science and Engineering Institute, University of Strasbourg, France

Paolo Samori Group

02-03/2019 (2 months)

Abstract

The presented thesis encompasses a brief summary of current literature discussing the application of supramolecular interactions in the generation of responsive supramolecular systems, as well as two reports/publications describing investigations of such systems. The research was approached interdisciplinary, implementing knowledge from various fields and techniques typical for organic chemistry and nanotechnology. The highly interdisciplinary nature of the research conducted within the frame of this thesis meant that the findings encompassed not only the design and synthesis of organic components and multi-faceted physicochemical characterization but also the recognition of application possibilities. The aim of the thesis was to design structures that were tailor-made to deliver the desired type of response.

The first report (*Chapter 2*; reprint A1) presents how hydrogen and coordination bonds within one type of functional group of the same molecule lead to morphologically different architectures. In both solution and on the surface of HOPG (highly oriented pyrolytic graphene), molecules of the discussed 2-pyridone derivative in amide tautomeric form generate complementary hydrogen bonds that allow the molecules to assemble into helical arrays. The tautomeric equilibrium does, however, shift toward iminol form when the metal ion (Zn^{2+}) is present, and the molecule forms an ML_2 type complex, which on the HOPG surface forms toroidal-shaped, non-covalently bound dimers. The molecule can be used as a colorimetric test for Zn^{2+} sensing since straightforward spectrophotometric studies revealed that both helical arrays and the ML_2 complex have distinct fluorescence responses. Colorimetric detection of metal ions was a subject of study in *Chapter 3* (reprint A2), in which ligand possessing acylhydrazone coordination pocked was deposited on the surface of spherical gold nanoparticles and used for detection of Ni^{2+}, Cu^{2+} and Fe^{3+}. The purpose of this section of the PhD thesis was to demonstrate how coordination interactions can be used for very effective and quick detection of metal ions. Additionally, our sensor outperforms similar systems that also operates in organic solvents, with nanomolar detection limits for all examined ions. We used a nickel-catalyzed Kumada coupling process, used in the production

of the active pharmaceutical component PDE472, to demonstrate the potential of our sensor. We evaluated the metal content in post-catalytic organic waste by ICP-MS and our sensor. Our finding shows that ICP-MS results show comparable value to result obtained from sensing experiment. However, whilst the process with our sensor only took a few minutes, the procedure with ICP-MS required pre-treatment of the sample and took several hours or even an entire day.

Chapter 1: Introduction

"Dear Colleague, abandon your idea of large molecules, organic molecules with molecular weights exceeding 5000 do not exist. Purify your products such as rubber, they will crystallize and turn out to be low molecular weight compounds."

friendly advice in the early 1920s from H. Wieland to H. Staudinger[1-2]

When Staudinger's macromolecular theory was finally accepted and later supported by Carothers (the first synthesis of nylon[3-4]), the world of science was fascinated by the development of new high molecular weight polymers, and many researchers made ground-breaking advances in the field. Conventional polymers mainly consist of long molecular chains, consisting of low molecular weight monomers, and have been widely used in contemporary technologies and industries because of their mechanical, thermal, and/or electronic properties. Nowadays, these polymers are having a great impact on our day-to-day lives. Their use ranges from food packaging[5] to advanced drug-release systems[6]. However, in such systems, almost all polymers are held together by irreversible covalent bonds, which have undesired consequences, such as being non-recyclable or being very hard to recycle, which leads to pollution and causes major negative environmental issues. When external stimuli are applied, the properties of these materials change and they cannot be further reused. The continuing demand for materials with divergent but specific properties was the driving force behind implying principles of supramolecular chemistry in material science. Supramolecular chemistry, by nature constitutionally dynamic[7], enriches the properties of polymeric materials with dynamic features. Material dynamicity originates from the presence of non-covalent interactions capable of undergoing formation or cleavage in distinct conditions, therefore having the capacity to vary in structure by exchange, incorporation, or rearranging of constituents. Reversible noncovalent interactions allow the development of stimuli-responsive supramolecular materials at the most fundamental level, and these materials also have the capacity for recyclability.

1.1 Types of interactions in supramolecular architectures

In the last three decades, we have witnessed the emergence of so-called smart materials based on nanocomposites and/or polymers. To correctly define and recognize smart polymers, one has to keep in mind that the polymer has to be stimuli-responsive, which means to be able to change macroscopically their structure and properties upon stimulus, but furthermore, after the stimulus is removed, these transitions have to be reversible and the system returns to its original state. Transitions that can occur, but are not limited to, are sol-gel transitions, the formation or disassembly of molecular architectures, and changes in solubility, shape, or surface characteristics.

It is still a great challenge to design supramolecular architectures with defined structures, and it is important to understand the interactions responsible for supramolecular polymerization. It allows the preparation of architecture with desired characteristics imprinted into the monomer. The driving forces for supramolecular polymerization are typically recognized as multiple hydrogen bonding, metal-coordination bonds, π-π interactions, and other non-covalent interactions such as host-guest interactions or hydrophobic effects. In the scope of this thesis, multiple hydrogen bonding and metal-coordination bonds are relevant and will be discussed.

1.1.1 Multiple hydrogen bonding

Inspired by DNA base pairing, hydrogen bonding has been extensively used in supramolecular polymer chemistry. Hydrogen bonds are perfect for building supramolecular architectures since they combine relatively high strength, which can be tuned with excellent reversibility, yielding stimuli-responsive behavior.[8-10] What is useful about H-bonds is that they are directional and complementary. An H-bond donor interacts with an H-bond acceptor, and *vice versa*.

The average strength of a single bond is typically insufficient to form a polymer because they are significantly weaker than ordinary covalent bonds (E = 5–30 kJ/mol). The most efficient and frequently used method to increase the strength of hydrogen bonds is by using multiple H-bonds in the formation of the supramolecular arrays, despite a few incredible reports that

describe supramolecular polymers based on a single hydrogen bond as a result of enhancing the bond strength by liquid crystallinity or phase separation. It was found (Jorgenson and Zimmerman) that not only a number but also an order of hydrogen bond donors (D) and acceptors (A) play a crucial role in enhancing the strength of H-bonds, as illustrated in Scheme 1 below. This phenomenon was explained by the importance of secondary electrostatic interactions. While in ADA-DAD systems, diagonally opposed sites repel each other, decreasing the binding constant, in AAD-DAA complexes, attractive electrostatic interactions play a role, increasing the binding constant severalfold.[11]

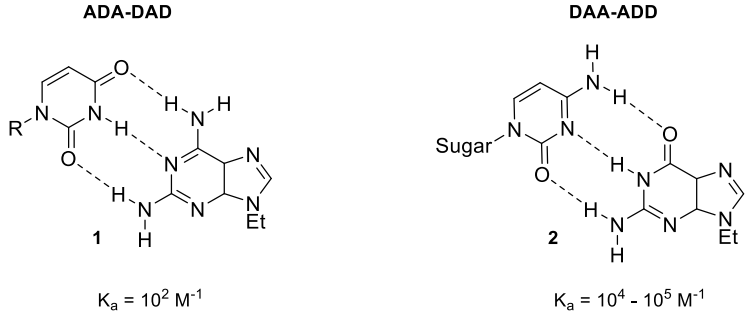

Scheme 1 Example of triple-hydrogen-bonding arrays and their binding constant.

According to the Gulliver principle, to prepare a highly stable supramolecular assembly, the next step is to increase the number of H-bonds within the binding motifs.[12-14] A nice example of a rigid binding motif that consists of eight hydrogen bonds was developed by the group Zimmerman.[15] This ureido-naphthyridine dimer **3** presents a self-complementary AADDAADD H-bond acceptor and donor pattern. Dimerization via eight hydrogen bonds occurs, in chloroform, as demonstrated by concentration-dependent NMR experiments. The ^{1}H NMR spectrum was unchanged in a concentration range of 423 μM to 13.5 mM in 10% DMSO in $CDCl_3$. A dimerization constant of $K_a = 4.5 \times 10^5\ M^{-1}$ was set as a lower limit. However, when DMSO content was increased to 20%, K_a dropped dramatically to a value of 40 M^{-1}, which demonstrates the substantial effect of the polarity of the solvent on the self-assembly of H-bonded complexes. In high-DMSO-content solutions and in pure DMSO, no dimerization occurs. The same was observed for protic solvents such as MeOH or water. This fact can also be an advantage since, as an illustrative example, it shows that K_a and, by all means, the strength of the hydrogen bond can be easily modulated by the polarity of the

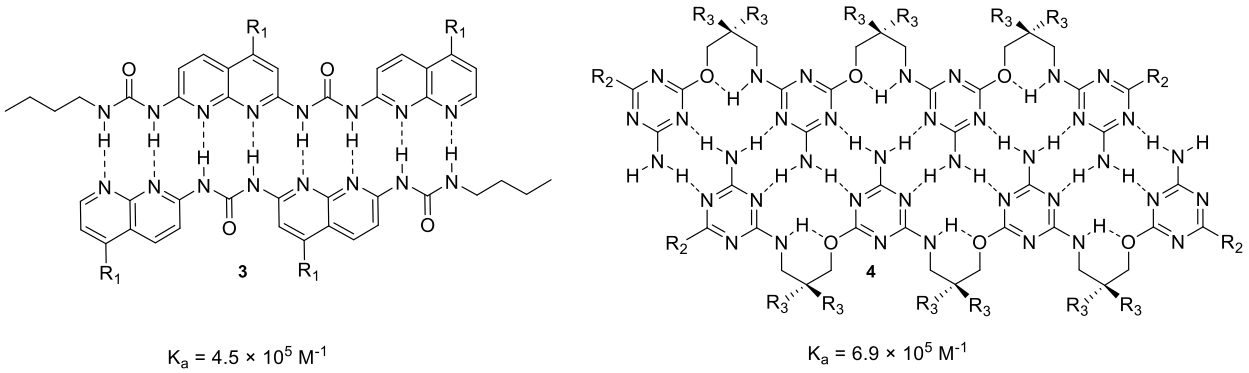

Scheme 2 Left: Self-complementary eight-fold hydrogen bonding pattern of dimer **3** and its dimerization constant (R_1 = $C_6H_4O(CH_2)_2C_6H_3(t\text{Bu})_2$); Right: Self-complementary ten-fold hydrogen bonding pattern of dimer **4** and its dimerization constant (R_2 = *N*-morpholinyl; R_3 = 4-decyloxybenzyl).

solvent. Conveniently, exact polarity can be achieved simply by mixing less and more polar solvents in defined proportions. An example of other factors affecting K_a was provided by Krische group who introduced duplex oligomers based on oligo aminotriazines. These flexible oligomers are built up from smaller subunits with a distinct H-bond pattern.[16] Trimer **4** (Scheme 2) is formed by ten hydrogen bonds between the oligomers and has an association constant of $6.9 \times 10^8\ M^{-1}$ in 1,2-dichloroethane. Surprisingly, when a tetramer is formed by fourteen hydrogen bonds, the association constant is extremely low, only $K_a = 1.1 \times 10^3\ M^{-1}$. The value is practically smaller than when the dimer is formed by only six H-bonds ($K_a = 2.3 \times 10^3\ M^{-1}$). This is due to intramolecular self-folding in the tetrameric strand, which competes with the self-assembly, showing how much the internal structure of the monomer affects the strength of the H-bonds forming the supramolecular assembly, not only the sequence and number of the hydrogen bond donors and acceptors.

Factors that influence the stability, morphology, or length of the arrays of the supramolecular structures based on hydrogen bonds, depends on the exact structure of the monomer unit. Other external factors that affect the self-assembly process include temperature, concentration, light, presence of metal ion and others. The interplay of factors influencing the assembly results in complete control over the architecture, which may play distinct functions and have different properties/morphologies in different environment.

1.1.2 Supramolecular architectures based on H-bonds

Aromatic amides such as naphthalenediimides (NDIs) and benzene-1,3,5-tricarboxamides (BTAs) are highly investigated compounds because of their distinctive behaviour in different environments and intriguing properties. In 2007, Pantoş et al.[17] (Sanders group) reported the unique behaviour of amino acid-decorated NDI **5**, see Figure 1.

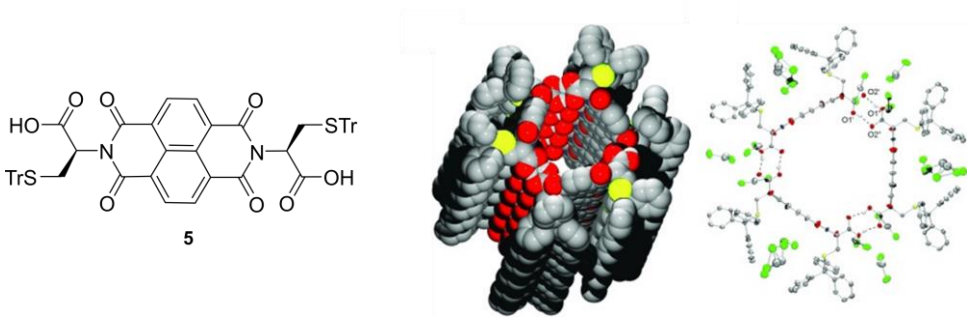

Figure 1 Left: molecular structure of **5**[17]; Right: Side and top views of the hydrogen-bonded nanotubular structure formed by **5**. Most of the hydrogen atoms and solvent molecules have been removed for clarity. Partially reprinted from Ref. 17 with permission from Wiley-VCH GmbH.

The free carboxylic groups in compound **5** formed a linear network of hydrogen bonds, which resulted in a tubular structure with an inner cavity lined by these interactions, as demonstrated by the X-ray structure of the compound. Circular dichroism showed that solid-state structure is interestingly preserved in chloroform solution. Above 300 nm, CD measurements showed a substantial cotton effect, which is consistent with the NDI core's UV/Vis absorption. The formation of a chiral supramolecular structure, similar to that seen in the solid state, in which NDI cores are organised in helical matter carrying *M*-chirality, has
been suggested as the explanation for the cotton effect. The same group reported in the same year that these supramolecular polymers do not exhibit any π-π stacking between the NDI cores, indicating that these electrons are still free to interact with aromatic compounds. In this report[18], authors describe filling the cavity of the nanotubes with C_{60} fullerene. It is also important to note that a number of other L-, D-amino acid derivatives of **5** were synthesised and demonstrated the same behaviour.

BTA derivatives form non-covalent helical architectures in apolar solvents via 3-fold intermolecular hydrogen-bonding interactions, which are reinforced by additional π-π stacking.[19] When present in a more polar solvent, or when the ester moiety is in close proximity

to the BTA core, dimers are formed[20-21], and if the carboxylic group is present in relatively close proximity to the BTA core, octameric capsules[22] are present in the solution. As already mentioned, BTA self-assembles in apolar organic solvents, although there are several interesting reports of BTA columnar assemblies in water.[23-25] Bochicchio et al. reported the effect of concentration on the self-assembly of BTA derivative in water.[26] The complexity of the assembly largely increases in water; therefore, simulations have been used as a useful tool to gain molecular-level insight into supramolecular polymers in various media, including water. The responsive character of polymeric arrays also formed in water by structurally complex BTA monomers was described by Fuentes et al.[27] The authors report the responsiveness of a linear, fibrous supramolecular polymer formed predominantly by multiple hydrogen bonds and π-stacks and stabilized by hydrophobic interactions. As can be seen in Scheme 3, monomer **6** consists of a BTA core, an azobenzene moiety at the periphery of the molecule, a PEG moiety, and (*S*)-lysine. All particular moieties imprinted specific properties and responsiveness of self-assembled supramolecular polymer.

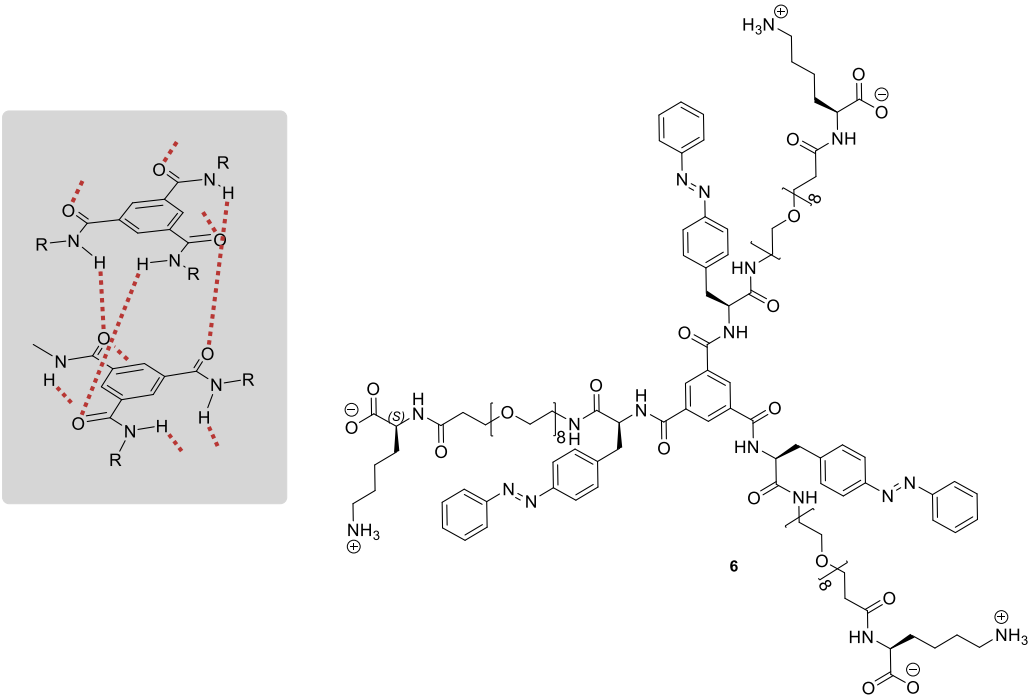

Scheme 3 Representation of typical 3-fold intermolecular hydrogen-bonding interactions of BTA derivatives forming columnar assemblies. Chemical structure of monomer **6**[27].

In particular, the BTA core was responsible for the 3-fold intermolecular hydrogen-bonding pattern, and azobenzene gave the polymer light responsiveness. Due to the PEG moiety, the molecule was soluble in water, and (*S*)-lysine gave the assembly responsiveness to pH and enhanced water solubility. The above-mentioned polymer disassembled as a response to UV light due to *trans*-to-*cis* isomerization of the azobenzene moiety. Irradiation caused major geometric change, which weakened the hydrogen bonding, and prevented effective overlapping of orbitals of the BTA core. TEM pictures showed that the number and length of the fibres increased as the system was heated above room temperature (75 °C). Assembly into longer arrays was then confirmed by a temperature cycling experiment performed with SLS. Aggregate **6** can be considered a smart material because this trend can be reversed (as seen by both TEM and SLS). This unusual temperature-enhanced polymerization was the result of the combined effect of the azobenzene moiety and PEG chain. The distribution of *trans*- and *cis*-isomers of the azobenzene moiety, is influenced by temperature, favouring the *EEE*-isomer, which is more thermodynamically stable. In comparison to isomers containing *Z*-azobenzene, this isomer is more likely to aggregate, hence by raising the temperature, additional aggregation might have taken place. Furthermore, due to the loss of solvating water molecules, temperature also enhanced the hydrophobicity of PEG, which increased the driving forces for self-assembly. Based on the pK_a values of the carboxylic and amine functional groups of (*S*)-lysine, three pH ranges were defined in which the molecule underwent significant changes. Between pH = 3.9 and 9.6, monomers were zwitterionic, having all three carboxylate groups and all three ammonium groups, with a net charge of 0. By decreasing pH to the 2.2 threshold, protonation of carboxylates took place, resulting in an increase in the positive charge of the molecule, which destabilised the supramolecular polymer and caused disassembly. On the other end, when the pH has been increased to pH = 12, deprotonation of ammonium and an increase in negative charge follow. This change of charge has the exact same effect as increasing the positive charge; thus, disassembly of the aggregate took place (Figure 2). A careful change of pH thus ensures the specific length of the fibrous polymer as observed by TEM.

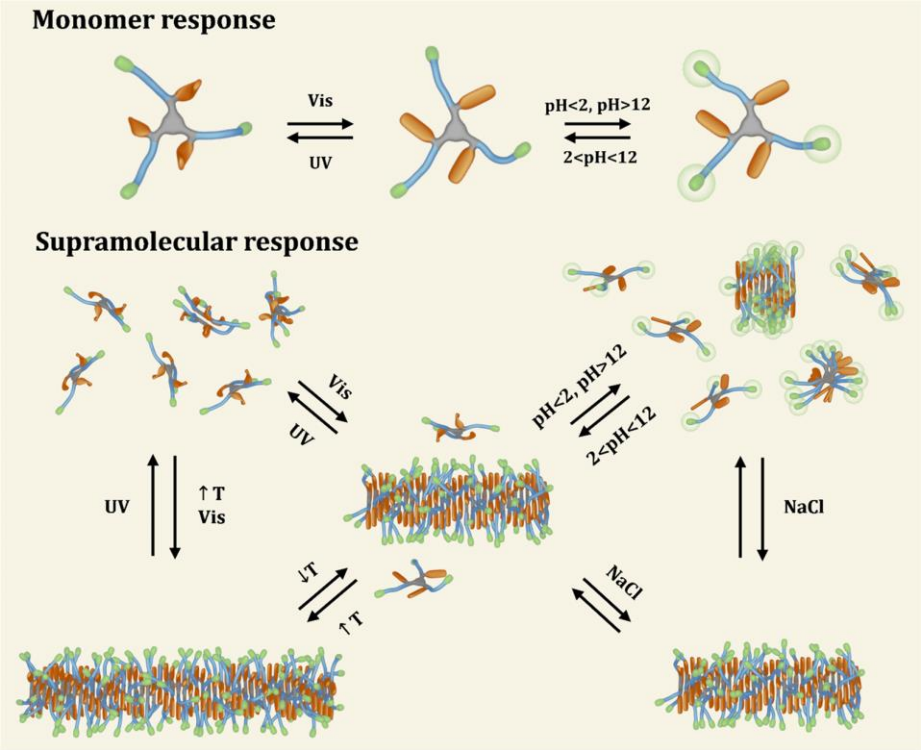

Figure 2 Schematic representation of the stimuli-responsiveness of the system based on **6**. Above, molecular responsiveness to light and pH. Below, supramolecular responsiveness to light, pH, ionic strength and temperature. Reprinted with permission from https://pubs.acs.org/doi/10.1021/jacs.0c02067. Copyright © 2020 American Chemical Society.

A wonderfully unique approach to responsive BTA materials has had Yano et al. under the umbrella of the Aida group.[28] BTA derivative was dissolved in liquid crystalline (LC) medium and columnar assembly formed by BTA directed the organisation of the previously nematic phase of LC into columnar. BTA not only acted as a template but also was included in the columnar phase of LC forming core-shell structure. This system used for an optoelectrically rewritable device, exploiting optically and electrically responsive properties.

The AD−DA hydrogen bonding motif of dimers formed by 2-pyridone derivatives has been known for several decades, but yet, they are still attracting a lot of attention, as witnessed by numerous studies published till today. Similarly, to NDIs and BTAs, Stončius et al. (2006) tried to prepare helical assemblies using the AD−DA hydrogen bonding motif of 2-pyridone[29]. The authors prepared C_2-symmetric molecules **7a-c** (Scheme 4) with the possibility to associate end-to-end. Molecular modelling showed that molecule **7a** should be able to self-assemble into helical tubular structures. It suggested that the diameter of this architecture

should be 12-14 Å, enough to host small organic molecules. Nevertheless, **7a** was only soluble in DMF and AcOH, and solid-state studies revealed competitive hydrogen bonds with the solvent and −NH (pyrol) group of the second **7a** molecule. To increase solubility and chance of preparing helical supramolecules, *N*-alkyl compounds **7b** and **7c** were prepared. A compound with a shorter alkyl group formed infinite supramolecular hydrogen-bonded networks via four A−D bonds between 2-pyrol moieties, unfortunately without helical morphology. The most promising molecule in the quest towards helical polymers was **7c**. In solution studies, including ^{1}H NMR spectroscopy, vapour pressure osmometry (VPO), UV-Vis, and CD measurements, revealed intermolecular association via the 2-pyridone motif. Molecules assemble according to an isodesmic model with an association constant of K_E = 77 M^{-1} (311 K, ^{1}H NMR dilution experiment) and 120 M^{-1} (313 K, VPO) and n = 3.7 ± 0.3, which refutes a dimer model. The standard enthalpy of the association process is similar to the enthalpy of dimerization of 2-pyridone itself, strongly suggesting that only an AD−DA hydrogen bonding motif is present, leading to helical assemblies, although the authors have not definitively concluded that this is the case.

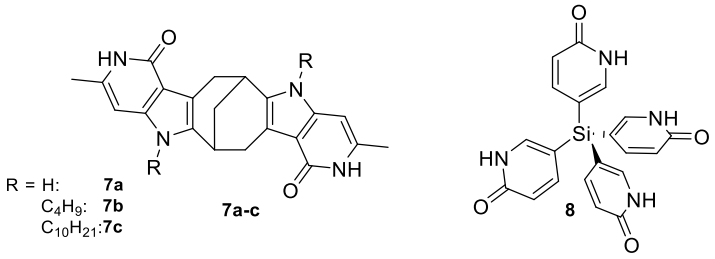

Scheme 4 Molecular structure of **7**[29] and **8**[30-31].

Silicon−2-pyridone derivative **8** on the other hand forms doubly interpenetrated highly ordered supramolecular network[31] in which each tecton forms a total of eight AD−DA hydrogen bonds with neighbouring molecules. Crystal structure shows that approximatelly 60% of volume is available for possible guests (solvent). In 2003[30], authors showed how different solvent guest molecules can influence the cell parameters, without destroying the structure (single-crystal to single-crystal transformation). For example, when crystal obtained from isovaleric acid is immersed in butyric acid for 5 hours, the replacement of guest molecules yield in ≥98% replaced crystals. The cell parameters are nearly identical, altought the crystals

are different that that obtained directly from butyric acid. Interestingly, when the contact with butyric acid is prolonged to 24 hours, crystals contract giving the same crystals as obtained directly from butyric acid. Authors showed that porosity of network build from **8** is adaptive, placing guest molecules with very close to walls of channels. This enforced contact, may provide transfer of information between host and guest.

1.1.3 Metal-ligand coordination

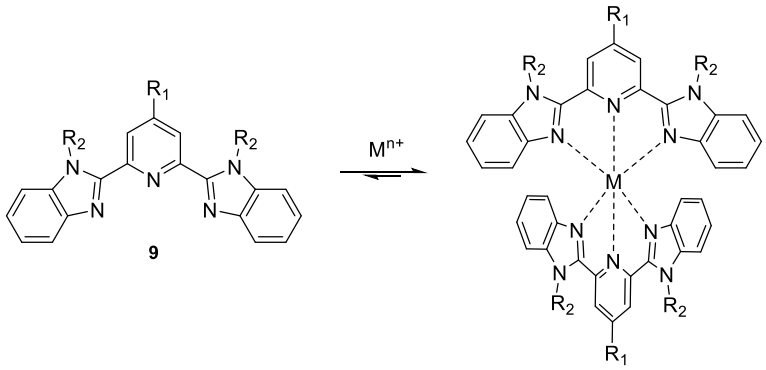

Scheme 5 Structure and metal ion coordination representation of ligand **9**[32] (R_1 = $O(CH_2)_4[O(CH_2)_4]_n$-**9**; R_2 = Me).

Coordination bonds are highly directional, strong interactions that are frequently used to build coordination polymers, metal-organic frameworks (MOFs), and other types of architectures.[33-34] The strength of a coordination bond between a metal cation and an organic ligand can easily approach the stability of a normal covalent bond. Coordination bonds, however, typically have enhanced kinetic lability, thus ability to break and reform, at the expense of lower thermodynamic stability. The frequency at which these bonds ought to break (dissociation rate) can be used to evaluate the lability of each metal-coordination bond. The advantage of coordination bonds is that they can be tailored more easily than ordinary covalent bonds or other non-covalent bonds, in terms of their bond strength and dissociation rate, just by varying pH or metal ion. Metallosupramolecular aggregates are stable in a variety of solvents, unlike exclusively H-bonded assemblies, however the properties of metallosupramolecular polymers (MSPs) and MOFs might vary depending on the solvent due to, for example, the solvatochromic effect.[35-36] In supramolecular architectures containing metal ions, the properties of organic polymers are combined with the electronic, optical, or catalytic potential

of metals. Metal-ligand coordination is a reversible, noncovalent interaction that facilitates the construction of stimuli-responsive MSPs. Since coordination compounds of different metals with the same ligand exhibit different properties, such as binding constants and thermodynamic behaviour, metallosupramolecular polymers are highly versatile materials. The tuneable coordination binding strength, as well as the fascinating redox and photophysical properties of the metal ions and ligands, provide opportunities for the application of metallosupramolecular polymers in materials science.

In chemical community, the Rowan group is one of leading groups for the development of stimuli-responsive supramolecular coordination materials. As an example, they demonstrated the utilisation of a tridentate ligand based on bisimidazole-pyridine (**9**, Scheme 5) in the generation of a thermoresponsive material that was employed for triethyl phosphate detection.[32] The same group employed the same ligand in a study of chemo-responsiveness of the material, which changed liquid crystalline characteristics when different metal ions were added.[37] This example demonstrates versatility of ligand **9** in the development of stimuli-responsive supramolecular polymeric materials.

Apart from responsive metallosupramolecular systems, devices utilising coordination bonds are sensors for metal ions. Sensing schemes can be based on, e.g., the optical properties of analytes or the chromogenic and fluorogenic properties of chelators. The fist type relies on the intrinsic optical properties of metals. In this instance, quantification is carried out either through luminescence or measurement of absorption (including the UV as well as near infrared). Copper, cobalt, nickel, the lanthanide ions along with the radionuclides are examples of suitable metals for this type of sensing.[38] The second sensing scheme employs sensors that interact with ions, which is typically accompanied by a change in the sensors' fluorescence or absorption. Changes in colour can be visible along with spectral changes, with one band appearing as the other disappears. Contrarily, the majority of fluorescent indicators are yes-or-no devices, with only one species being fluorescent. This approach is widely used in the generation of powerful sensors used for the detection of trace metal ions in various media, from organic solvents to water, for example, in testing real water samples.[39] Heavy metals above a certain threshold limit are toxic to humans and are responsible for a number of life-

threatening diseases. Sensors that are able to detect dangerous metal ions such as Hg^{2+}, Cd^{2+}, Pd^{2+}, or Ni^{2+} are of importance in environmental and general health studies since even a small amount of toxic metals has a major negative effect on living systems.[40-42] Such sensors can give a colorimetric response visible to the naked eye or a response easily measurable by the fluorescence of UV/Vis spectroscopy, since the spectroscopic properties of complexes and their metal-free counterparts are usually tremendously different, making the testing process extremely quick. Because the coordination bond is reversible, recycling of the sensor is often observed either by heating the system or by adding acid or competitive chelating agents to the sample.[43-45] The following section of the thesis will focus on literature examples of sensors based on 2-pyridone ligands and Schiff bases.

1.1.4 Optical sensors for metal ions

As already mentioned earlier in this chapter (*1.1.2 Supramolecular architectures based on H-bonds),* 2-pyridone forms AD-DA hydrogen bonds; however, this molecule is able to undergo a tautomerism reaction. From the first synthesis of 2-pyridone (1883)[46] to the present day, the nature and determination of keto-enol tautomerism of this compound have been areas of intense research activity over several decades.[47-49] This dual character has opened a new perspective on using derivatives of 2-pyridone in dynamic supramolecular chemistry for their possible ability to switch between different architectures and properties. 6-pyridinyl-2-pyridone compounds are especially intriguing because, while in the amide form free hydrogen bond acceptor and donor are present in the structure, the iminol form possesses a 2,2'-bipyridine coordination pocket, one of the most widely used ligands for the coordination of various metal ions (e.g., Os^{2+}, Ru^{2+}, Pt^{2+}, Pd^{2+}, and Zn^{2+}). The ability of 6-pyridinyl-2-pyridone compounds to bind metal ions in their iminol form, leading to sensitive Zn^{2+}

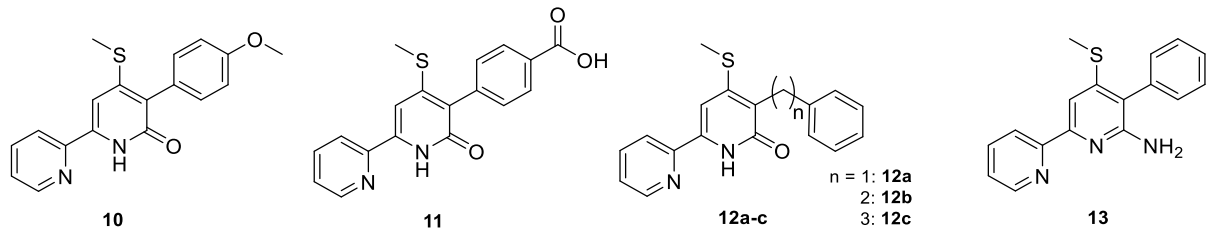

Scheme 6 Molecular structure of 2-pyridone derivatives **10**[50], **11**[51], **12a-c**[52] and **13**[53].

detection, was nicely presented by Higamori and Saji[50-53] (see Scheme 6). First, it was discovered that the 6-pyridinyl-2-pyridone derivative **10** interacts with Zn^{2+} in the iminol form and the −OH proton is required for the chelation-enhanced fluorescence (CHEF) effect.[50] Then, more compounds with the same 6-pyridinyl-2-pyridone skeleton were synthesised using various, both electron-donating and electron-withdrawing substituents in the 3-position.[51] Fluorescence was only observed in compounds with the so-called push-pull electron effect; in all other cases, fluorescence was either faint or absent until Zn^{2+} ions were added. A compound with little to no fluorescence (**11**) shown good fluorescence ON/OFF switching capabilities with Zn^{2+} with LoD = 0.5 μM for $ZnCl_2$.[51] Job's plot indicated that the complex between **11** and Zn^{2+} forms 1:1 stoichiometry, and the dissociation constant K_d was calculated to be 3×10^{-5} M. This complex was stable at pH > 6, suggesting that it can be used under physiological conditions in the process of imaging living cells.[51]

Derivatives **12a–c** with different spacers were prepared to understand the role of the phenyl ring.[52] All three compounds were soluble in water, and all spectroscopic measurements were carried out in HEPES buffer. The emission of all compounds was measured, and quantum yields suggested that when a phenyl ring is directly attached and acts as the electron donor, the quantum yield is the highest. Compounds with methylene spacers exhibited a lower quantum yield; on the other hand, the emission intensity ratio in the presence and absence of Zn^{2+} was higher than that of 1. Specifically, in the case of **12b**, an 18-fold fluorescence enhancement

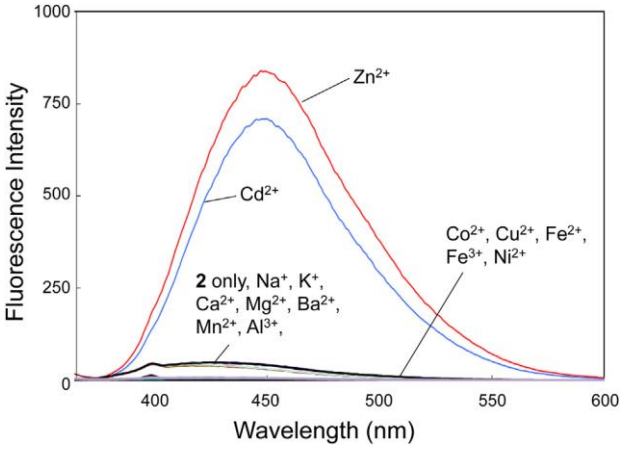

Figure 3 Fluorescence spectra of **12b** upon the addition of different metal cations in HEPES buffer (100 mM, 5% DMSO, pH = 7.4, excitation wavelength: 351 nm). Reprinted from ref. 52 with permission from Elsevier. Copyright © 2015 Elsevier.

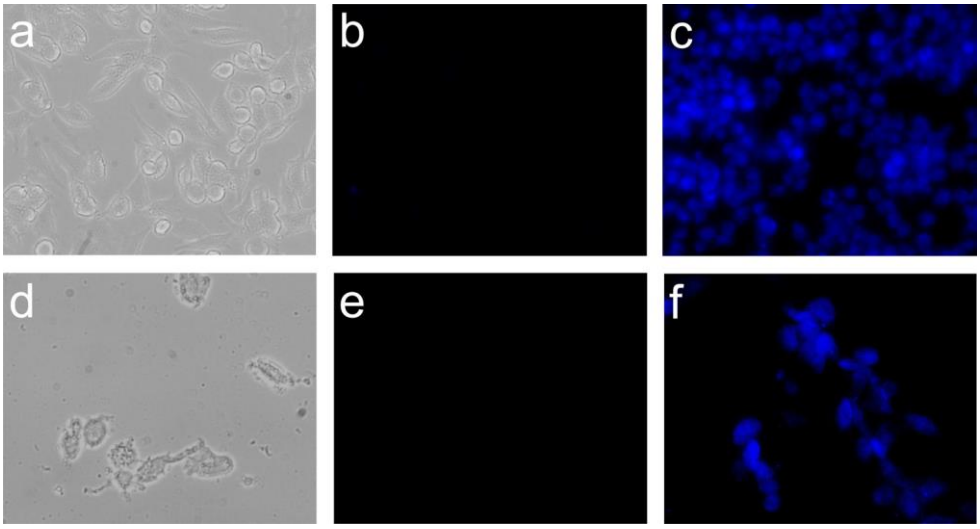

Figure 4 Fluorescence images in RAW 264 and HepG2 cells: (a) bright-field images of cells with **12b** (30 mM) in RAW 264 cells; (b) fluorescence image of (a); (c) fluorescence images incubated with **12b** (30 mM) and Zn^{2+}/pyrithione (100 mM) in RAW 264 cells; (d) bright-field images of cells with **12b** (30 mM) in HepG2 cells; (e) fluorescence image of (d); (e) fluorescence images incubated with **12b** (30 mM) and Zn^{2+}/pyrithione (100 mM) in HepG2 cells. Pyrithione is a zinc-selective ionophore. Reprinted from ref. 52 with permission from Elsevier. Copyright © 2015 Elsevier.

was observed. The dissociation constant K_d for this compound was calculated to be 7×10^{-5} M, and the ratio M:L was determined to be 1:1. When other metal ions (Al^{3+}, Ca^{2+}, Cd^{2+}, Co^{2+}, Cu^{2+}, Fe^{2+}, Fe^{3+}, K^{+}, Mg^{2+}, Mn^{2+}, Na^{+}, and Ni^{2+}) were introduced to the HEPES solution of **12b**, selective behaviour was observed, and fluorescence enhancement took place only in the case of Cd^{2+} and Zn^{2+} (Figure 3).This experiment also shown that the metal ions Na^{+}, K^{+}, Mg^{2+}, and Ca^{2+}, which are found at millimolar amounts in living systems, do not affect the CHEF effect with Zn^{2+}. To evaluate possible biological uses, fluorescence microscopy images of two types of living cells containing **12b** (mouse macrophage-like cells; RAW 264; and hepatocellular carcinoma cells; HepG2) were acquired. When Zn^{2+}/pyrithione and compound **12b** were present in both cell lines, strong intracellular fluorescence occurred, suggesting a sensitive response to Zn^{2+} under physiological conditions (Figure 4). Therefore, compound **12b** might be useful for understanding biological functions of Zn^{2+}.[52]

Once pyridine-pyridone tautomerism is supressed, like in case of **13**[53], the affinity of the whole system towards Zn^{2+} increases, which results in a lower K_d value (2.2 Nm) and more efficient imaging in the living cells. However, the dual nature of 2-pyridone derivatives is crucial to achieve both the coordination of metal ions and hydrogen bonding. The ability of various 2-

pyridone derivatives to form hydrogen-bonded dimeric structures was described by Forlani[49] and then confirmed by DFT calculations by Jia[54]. In 2011, our group investigated hydrogen-bonded structures formed by the pyrimidine-pyridone derivative, which in amide form dimerizes, and these dimers further organised into helical arrays on the surface of highly oriented pyrolytic graphite (HOPG), as witnessed by STM (*detailed description of structure and behaviour in Chapter 2).*[55] Nevertheless, neither the coordination ability of the mentioned 2-pyridone derivative nor its responsiveness were exploited. We recognised this and decided to study the intriguing switching mode of this compound and the responsiveness of both the hydrogen-bonded structure and the Zn^{2+} complex, which is described in *Chapter 2*.

Schiff bases are an another type of powerful and versatile sensors. These compounds, whether in the form of acylhydrazones or salen ligands, include a reversible imine bond (Scheme 7) responsible for their dynamic character.

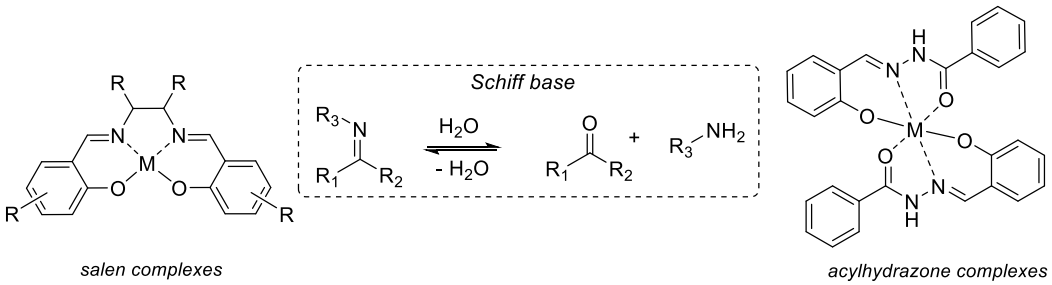

Scheme 7 General structure of Schiff bases and representative examples of Schiff base metal complexes.

They represent a very effective chelating system for binding metal cations throughout the *p*-, *d*-, and *f*-block[56-57] and they have been used for colorimetric ion sensing, sometimes with detection limits in the micromolar range.[39,58-60] Schiff base ligands **14a** and **14b** (Scheme 8) were introduced by Gupta et al.[58] as flexible yet selective sensors for metal cations: Co^{2+}, Ni^{2+}, Zn^{2+}, Cd^{2+}, Cu^{2+} (no interaction was observed with ions like Ca^{2+}, Mg^{2+}, Mn^{2+}, Hg^{2+}, Cr^{3+},

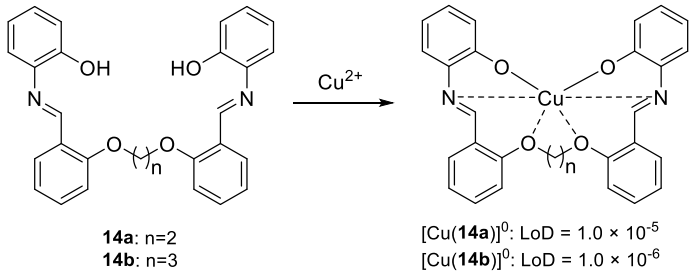

Scheme 8 Molecular structure of **14a**[58] and **14b**[58] and possible binding mode with Cu^{2+} ion with indicated limits of detection (LoD).

Table 1 K_f and LoD values of **14a** and **14b** in the presence of different metal ions.

No.	Metal cation	Formation constant		Limit of detection [M]	
		14a	14b	14a	14b
1	Cd^{2+}	1.46×10^5	1.59×10^5	1×10^{-4}	1×10^{-5}
2	Co^{2+}	3.49×10^4	6.78×10^4	1×10^{-4}	1×10^{-5}
3	Cu^{2+}	1.26×10^6	1.44×10^6	1×10^{-5}	1×10^{-6}
4	Ni^{2+}	1.98×10^5	2.02×10^5	1×10^{-4}	1×10^{-5}
5	Zn^{2+}	1.44×10^5	1.20×10^5	1×10^{-4}	1×10^{-5}

Pb^{2+}, and Fe^{2+}). The highest affinity for Cu^{2+} ions was demonstrated by low limits of detection values and a high metal-ligand formation constant K_f (see Table 1). UV/Vis measurements in methanol were used to assess the performance of the sensor, and the authors even went as far as to demonstrate practical colorimetric detection. Filter papers were immersed in separate 0.01 M MeOH solutions of both receptors to create the first test strips, which were then air-dried. As-prepared strips were used to detect various metal cations. Test strips were submerged in solutions of Co^{2+}, Ni^{2+}, Cd^{2+}, Zn^{2+}, and Cu^{2+} cations and the obvious colour changes were observed. Strips prepared from both **14a** and **14b** solutions were used for metal sensing at different ion concentrations and exhibited colorimetric changes visible to the naked eye in methanol (0.1 mM and 1 mM, respectively) and water (10 mM and 100 mM, respectively) solutions of all tested cations.

A Schiff base colorimetric sensor for Fe^{3+} ions, which also acts as a fluorescent sensor for Zn^{2+} ions, was described by Zhang Group[61]. Simple ligand **15** forms M:L = 1:1 complex with Fe^{3+} and Zn^{2+} perchlorate salts (Scheme 9) in a selective manner, since from all tested metal ions (Fe^{3+}, Hg^{2+}, Ag^{+}, Ca^{2+}, Cu^{2+}, Co^{2+}, Ni^{2+}, Cd^{2+}, Pb^{2+}, Zn^{2+}, Cr^{3+}, and Mg^{2+}), only these two cations caused a change in the UV/Vis or fluorescence spectrum in DMSO solution. Sensor **18** exhibited a strong absorption band from 413 to 480 nm when 20 equivalents of Fe^{3+} ions were added to the solution. After 95 minutes, **15** responded with a dramatic colour change, from yellow to colourless, which could be easily detected by the naked eye. Sensor **15** alone displayed a weak, single fluorescence emission band at 483 nm when it was excited at 370 nm. Upon addition of 10 equivalents of Zn^{2+} to a DMSO solution of **15,** an obvious fluorescence enhancement was observed, indicating Zn^{2+}-selective OFF/ON fluorescent signalling.

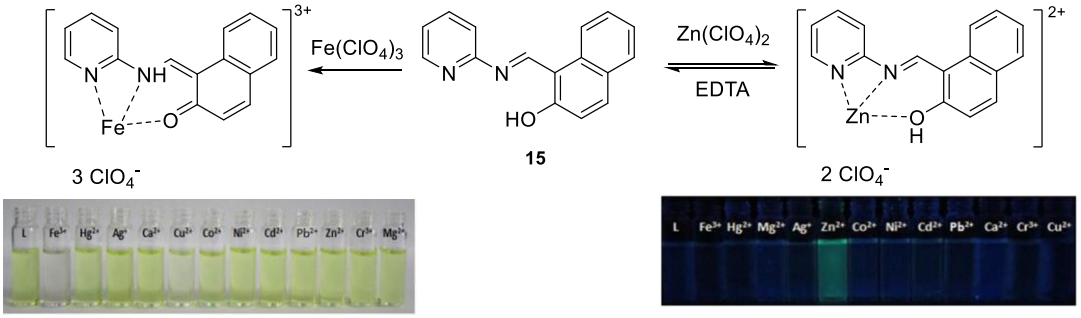

Scheme 9 Molecular structure of Schiff base **15**[61], its binding mode and colorimetric response to Fe^{3+} (left) and Zn^{2+} ions (right).

The enhancement of planarity and rigidity driven by coordination, which reduces the non-radiative decay of the excited state and increases fluorescence, appears to be the reason for this fluorescence behaviour. Since the coordination reaction was completed immediately after Zn^{2+} addition, it is possible to utilise **15** for real-time detection (see Scheme 9). Interestingly, the reversibility of the sensor **15** was tested by titration of the [Zn(**15**)$(ClO_4)_2$] complex with EDTA. Upon addition of 0.6 equivalents of EDTA, the fluorescence emission intensity increased to match that of free **15**.

Fluorescent Schiff-based sensors could be utilised for cell imaging similarly to 2-pyridone-based sensors, as shown by the Zheng group.[60] Acylhydrazone **16** (Scheme 10) is not fluorescent in DMSO, but when water was added, DLS and SEM detected aggregation-induced emission (AIE). To access the „off' state of the sensor, solvent mixture DMSO-H_2O (9:1 v/v) was selected since the fluorescence of **16** is very weak in these conditions. Upon addition of different ions (Li^+, Na^+, K^+, Ca^{2+}, Mg^{2+}, Al^{3+}, Zn^{2+}, Fe^{3+}, Pb^{2+}, Cu^{2+}, Hg^{2+}, Mn^{2+}, Cr^{3+}, Cd^{2+}, Co^{2+}, Ni^{2+}), sensor **16** showed selective coordination of Al^{3+} ions and fluorescence enhancement was observed. However, when it came to Fe^{3+} ions, interesting behaviour was observed. The paramagnetic nature of this ion prevented fluorescence changes, but an apparent colour change was noted. This can be utilized for colorimetric detection of this ion. Once the solvent composition was changed to THF-H_2O (9:1 v/v), fluorescence of sensor **16** also increased in the presence of Zn^{2+} ions.

The combined effects of excited state intramolecular proton transfer (ESIPT) and chelation-enhanced fluorescence (CHEF) may be responsible for Al^{3+} and Zn^{2+} sensing, while the colorimetric detection of Fe^{3+} ions is explained by ligand-metal charge transfer (LMCT).

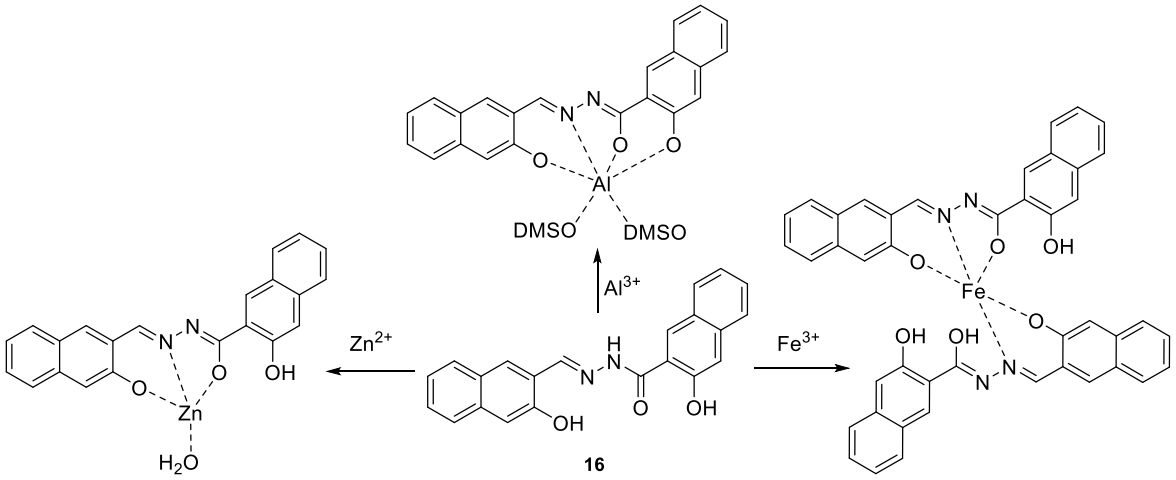

Scheme 10 Molecular structure of sensor **16**[60] and its binding mode with Zn^{2+}, Al^{3+} and Fe^{3+}.

According to the Job plot, the binding stoichiometry for both Al^{3+} and Zn^{2+} is M:L = 1:1, and in the case of Fe^{3+}, it is 2:1, as presented in Scheme 10. Detection limits (LoD) for all three tested ions are very low in micromolar concentrations (LoD_{Al} = 3.66 μM, LoD_{Zn} = 1.01 μM, and LoD_{Fe} = 0.34 μM). Both zinc and aluminium metal ions play an important role in living organisms, which is why intercellular imaging was studied. For cellular imaging, the SH-SY5Y cells were first incubated with $Al(ClO_4)_3$ and $Zn(ClO_4)_2$ separately, then **16** was added. The images obtained by a confocal laser scanning microscope showed no fluorescence emissions before the addition of the sensor; however, after the addition of acylhydrazone **16**, green fluorescence was observed, clearly demonstrating intracellular Al^{3+} and Zn^{2+} detection.[60]

To enhance the sensitivity of Schiff base sensors, different approaches were undertaken, although the most attention-grabbing was utilising the surface plasmon resonance of gold nanoparticles (GNP). GNP have fascinated people since ancient times because of their intense colour and distinctive photo-physical properties. When a gold nanoparticle is exposed to light, a collective coherent oscillation of the free electrons of the metal is induced. This oscillation around the particle surface causes a charge separation, forming a dipole oscillation along the direction of the electric field of the light. The amplitude of the oscillation reaches its maximum at a specific frequency, which is called surface plasmon resonance (SPR).[62] Over the last two decades, the plasmon resonance of gold nanoparticles has been the subject of intense research efforts and has found applications ranging from sensing to cell imaging.

To functionalize the gold nanoparticle surface, N-Au electrostatic interactions or strong covalent-like S-Au interactions are utilised. Consequently, several capping agents for gold nanoparticles, including 11-mercaptoundecanoic acid[63-64] or α-lipoic acid derivatives[65-66], contain a thiol, sulphide, or disulfide group. In 2015, Jimoh et al.[67] deposited Schiff base ligand with free thiol group **17** (Scheme 11) on the surface of spherical gold nanoparticles to prepare an active sensor for Fe^{3+} ions.

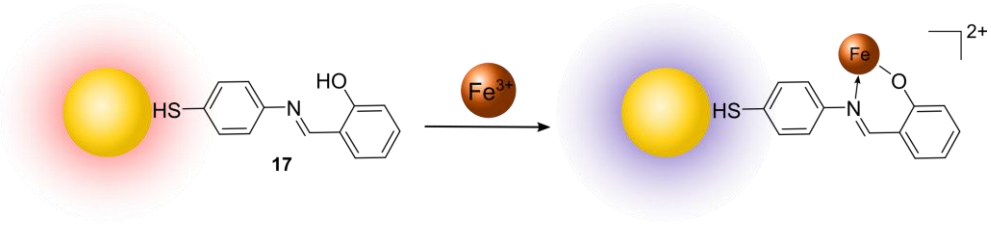

Scheme 11 Molecular structure of ligand **17**[67] and its binding mode.

For the synthesis of **17**@AuNPs, it was essential to optimise the GNP-to-ligand molar ratio because an excess of ligand caused the GNP to aggregate and precipitation from the dispersion. As anticipated for small (8–10 nm) spherical GNPs, after surface modification, the SPR band in the UV/Vis spectrum was at 530 nm. The plasmonic absorption peak shifted from 530 to 559 nm in the presence of Fe^{3+} ions, which can be observed by the naked eye as a change of colour from red-pink to deep purple.

Interestingly, the UV-Vis spectra were not affected by the presence of other metal ions (Al^{3+}, Ni^{2+}, Cu^{2+}, Co^{2+}, Hg^{2+}, Zn^{2+}, Na^{+}, K^{+}, Ca^{2+}, and Rb^{+}), demonstrating that no aggregation had occurred, showing excellent selectivity for Fe^{3+} ions. The binding mode was determined as M:L = 1:1, with constants calculated from both absorption ($8.5 \times 10^5\ M^{-1}$) and emission ($2.9 \times 10^5\ M^{-1}$) titrations. The selectivity of the sensor towards ferric cations is explained by the difference in the coordinative interaction energy for various cations that otherwise do not substantially differ in ionic size. The detection limit of the sensor for Fe^{3+} cations is very low and was estimated as LoD = 1.2 μM. The value compared to Schiff base sensors in the literature is, in some cases, two-fold lower due to the enhanced sensitivity. However, much higher sensitivity can be achieved, as demonstrated by Ghaedi group.[68] An asymmetric Schiff base ligand was specifically synthesised for Hg^{2+} detection in aqueous media for real water sample analysis (Figure 5). The practical feasibility of this colorimetric sensor for monitoring

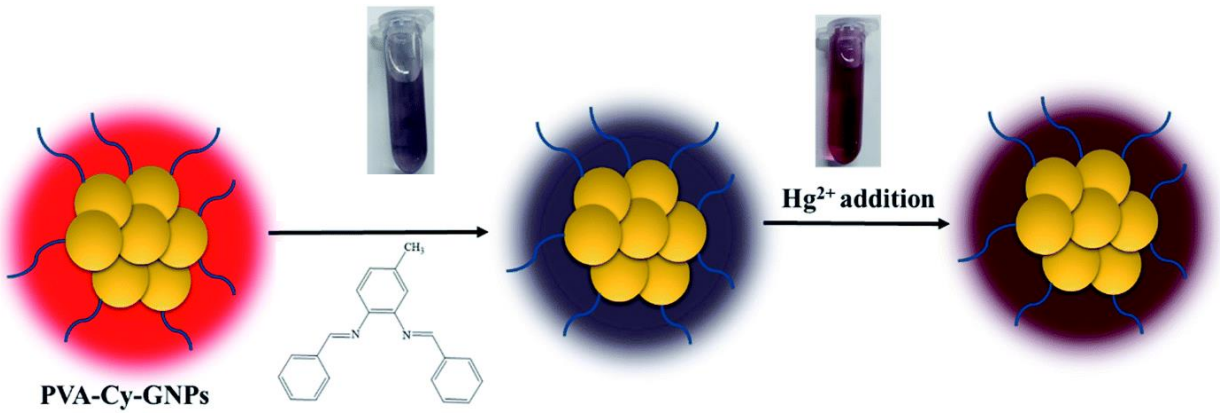

Figure 5 Schematic representation of the sensing assay for Hg^{2+} ions. Reproduced from Ref. 68 with permission from the Royal Society of Chemistry.

Hg^{2+} ion concentration was tested using two actual water samples: mineral water and river water. The results obtained by the authors show excellent accuracy and precision for the quantification of the Hg^{2+} ion concentration in these real samples. The detection abilities of the sensor were evaluated by UV/Vis spectroscopy. Upon addition of Hg^{2+} ions to the solution of the sensor, a red shift and broadening of the SPR band of the sensor were observed as a result of aggregation, which was also accompanied by a visible colour change. This colorimetric response was subjected to a selectivity study, and numerous metal ions were tested (Cd^{2+}, Ni^{2+}, Co^{2+}, Ag^{+}, Zn^{2+}, Cu^{2+}, Pb^{2+}, Fe^{3+}, Mn^{2+}, Na^{+}, Mg^{2+}, and Ba^{2+}). The sensor has not shown high affinity for any of the tested ions, illustrating how specific the sensor is towards Hg^{2+} ions. The detection limit was determined as LoD = 0.619 nM, which is at least another 3-fold higher sensitivity compared to Schiff base-capped nanoparticles described by Jimoh et al[67].

As illustrated by this handful of examples, Schiff bases have a great potential for trace metal ion detection and, in some cases, even quantification. It was also showed that a potent and sensitive colorimetric sensor could be created by combining the strong metal ion coordination displayed by Schiff bases with the high sensitivity of the gold nanoparticle surface. Although it is important to broaden the spectrum of potential sensing media since it can lead to new potential applications for Schiff base-caped nanoparticles, a substantial portion of research is still focused on sensing in aqueous media. In order to detect trace metal ions in

organic products like active pharmaceutical ingredients (APIs), organic waste, or post-catalytic reaction mixtures, we decided to prepare Schiff base-capped nanoparticles specifically designed for sensing in organic solvents. This challenging task is described in *Chapter 3*.

Research objectives

The ultimate goal of the research conducted in the scope of this thesis was to prepare systems in which the response is based on specific non-covalent interactions.

Individual goals were to:

I. Design molecules that will be able to form intermolecular supramolecular interactions, in particular, hydrogen bonds (A1), coordination bonds (A1 and A2), or both at the same time (A1). The design was focused on delivering a specific response of the system, and the molecular structures of the components were fully adapted to this goal. The desired response had to be: a) unique and new to the literature, filling the gaps in the literature (see *Chapter 1: Introduction*); b) easily measurable by benchtop spectroscopic methods and/or the naked eye (A1 and A2); c) suitable to produce stimuli-responsive architecture for either the development of smart materials (A1) or sensors (A1-A2).

II. Synthesise desired molecules in a step-saving and highly optimised manner using known procedures or in-house-made protocols.

III. Characterise synthesised molecules in their monomeric „off" state and, when supramolecular interactions are allowed, their „on" state. Characterization in solution by spectroscopic methods (e.g., UV-Vis, CD, NMR) was as important as characterization on the surface by various microscopic methods (SEM, TEM, STM).

IV. Determine stimuli and mechanism of the response of prepared supramolecules in solution and on the surface by a wide range of spectroscopic and microscopic techniques.

V. Test the application potential of prepared supramolecular architectures.

Chapter 2: Stimuli-responsive system based on 2-pyridone

Stimuli-responsive materials are currently one of the most appealing parts of materials science.[69] These materials have capacity to change their structure on a macroscale, but these transitions are also reversible, and the system returns to its original state once the stimulus is removed. They have the ability to change how they assemble, which influence sol-gel transitions, as well as shape, size, solubility, and surface properties. Supramolecular noncovalent systems reversibly assemble and disassemble through external physicochemical stimuli that enable the „on" and „off" states. Metal ions are the most versatile of the several stimuli that have been utilised to influence self-assembly of various compounds. Since different metal ions exhibit different binding patterns as well as general thermodynamics, in principle, the properties of these entities can be specifically tuned. Interesting ligands used for dual metal coordination are ambidentate ligands, able to coordinate through either different atoms or functional groups of the molecule. Due to the tautomerism, **22** (Scheme 12), which is a C_2-symmetric derivative of the 6-pyridinyl-2-pyridone, also possesses this dual character similar to that of ambidentate ligands. **22**, in its pyridone (amid) state, forms a highly stable non-covalent organic polymer. Using acid-base titration, responsiveness of the polymer was demonstrated. The polymer disassembles when exposed to a chemical stimulus (base), however reassembly of the polymer was observed after the stimulus was removed (by neutralisation with acid). Given the reactivity of 6-pyridinyl-2-pyridones (*Chapter 1*), we were especially interested in how **22** behaved when metal ions were present. Metal ions shifted the tautomeric equilibrium towards the pyridine form of **22** (iminol), which caused the disassembly of the original polymer and simultaneous coordination into the ML_2 complex. These complexes further assemble into toroidal dimers through additional hydrogen bonds. This change was accompanied by changes in properties such as solubility, fluorescence, and overall morphology.

2.1 Synthesis of 22

22 was prepared according to the known procedure in three steps.[55] In detail, commercially available 2-bromo-6-methoxypyridine (**18**) was first transformed into 2-methoxy-6-

(tributylstannyl)pyridine (**19**) by reaction with *n*-butyllithium and tributyltin chloride at −78 °C in dry tetrahydrofuran. After an overnight reaction, **19** was collected as light yellow oil and was directly used in the next step. A coupling reaction with 4,6-dichloro-2-phenylpyrimidine (**20**) in toluene in the presence of $Pd^0(PPh_3)_4$ afforded 4,6-bis(6-methoxypyridin-2-yl)-2-phenylpyrimidine (**21**) in a very good 89% yield. The final deprotection step (HBr, AcOH) yielded in **22** a good 70% yield (see Scheme 12). **22** was isolated as a yellow powder, and the structure was confirmed by NMR spectroscopy and compared with the literature data.[55]

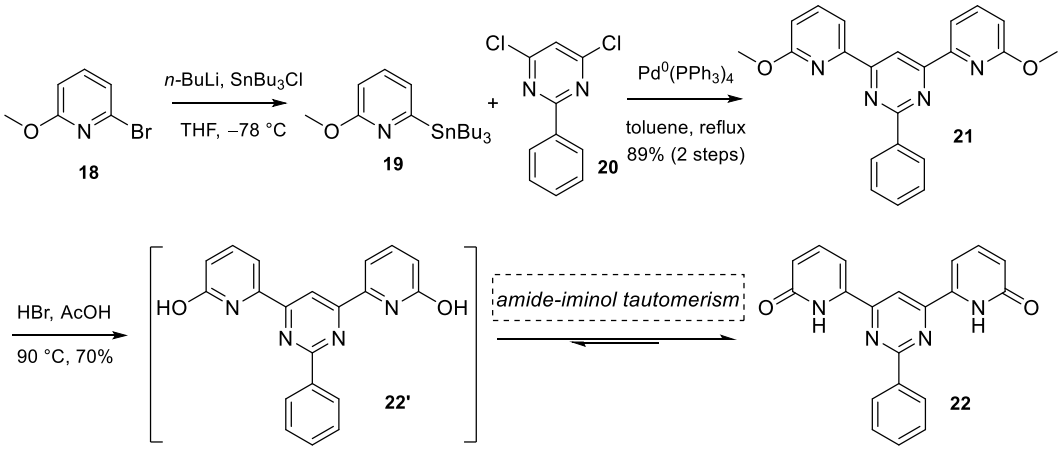

Scheme 12 Synthesis of **22**.

The solubility of **22** is very limited, and the compound can only be dissolved in borderline polar organic solvents such as dimethylformamide (DMF) and dimethylsulfoxide (DMSO). According to both computational and experimental research, the amide and iminol forms of 2-pyridone have comparable energies, which means that both forms are equally accessible depending on the chemical environment.[70-71] In the case of **22**, the amide form is dominant in the solution since, in polar solvents like alcohols or DMSO, tautomeric equilibrium usually shifts in favour of the amide form.[49]

By simply rotating the pyrimidine and pyridine moieties around a single bond, at least three distinct conformations of **22** are possible (Scheme 13) each of which permits a different intra- and intermolecular H-bond. Both the literature and the collected NMR data indicate that only the *C* form is present in the DMSO solution. Further investigation by several techniques revealed that intermolecular interactions between NH···O=C stabilize this conformation and lead to supramolecular aggregation.[55]

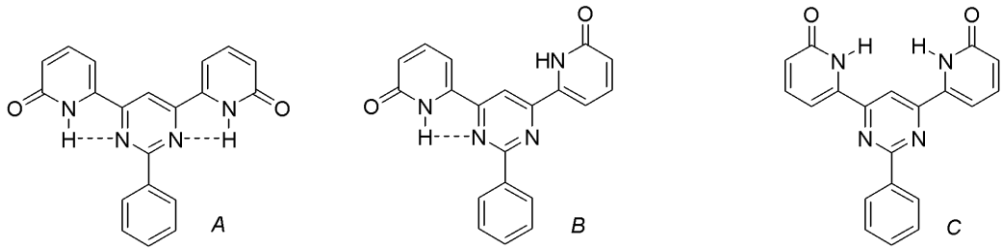

Scheme 13 Conformations of molecule **22**.

2.2 Self-assembly and responsiveness of 22

The formation of H2L dimers by six complementary NH···O=C hydrogen bonds, followed by the formation of helical dynamer by two additional CH^{ar}···O=C bonds on HOPG (DMSO-1,2,4-trichlorobenzene solution), has already been described.[55] To confirm that synthesised **22** self-assembles in the same manner, matrix-assisted laser desorption ionisation (MALDI) mass spectra were recorded, which revealed monomer, dimer, and trimer of **22**, similarly to those reported.[55] To match the reported data, we attempted to observe the dynamer by scanning tunnelling microscope, and we were able to obtain the same helical structures as seen in the literature. Unreported before, the ^{1}H NMR spectra of DMSO-d_6 showed relatively broad peaks and a low-field NH resonance at 11.5 ppm. These observations also indicate involvement in the described H-bonding, which is crucial for the self-assembly of helical structures.

Also unreported, the behaviour of the **22** solution in DMSO-d_6 upon HCl (aq.) addition revealed that protonation does not take place, which can be explained by the weak basicity of both pyrimidine and amide moieties. However, the acidity of 2-pyridone in DMSO is well known, and pK_a in DMSO was determined at pK_a = 17[72]. To obtain an iminolate form that would be able to form metal complexes, the **22** solution in DMSO-d_6 was treated with sodium hydroxide solution and observed by NMR spectroscopy.

The addition of two molar equivalents of NaOH yielded the visual change of the solution, which was vibrant yellow and dramatically changed the overall look of the NMR spectrum. Peaks were very well resolved and sharp, indicating the monomeric nature of $\mathbf{22}^{2-}$. NaOH both disturbed hydrogen bonding and generated an iminolate anion. This process is fully reversible by simply counteracting the NaOH with hydrochloric acid, as demonstrated in

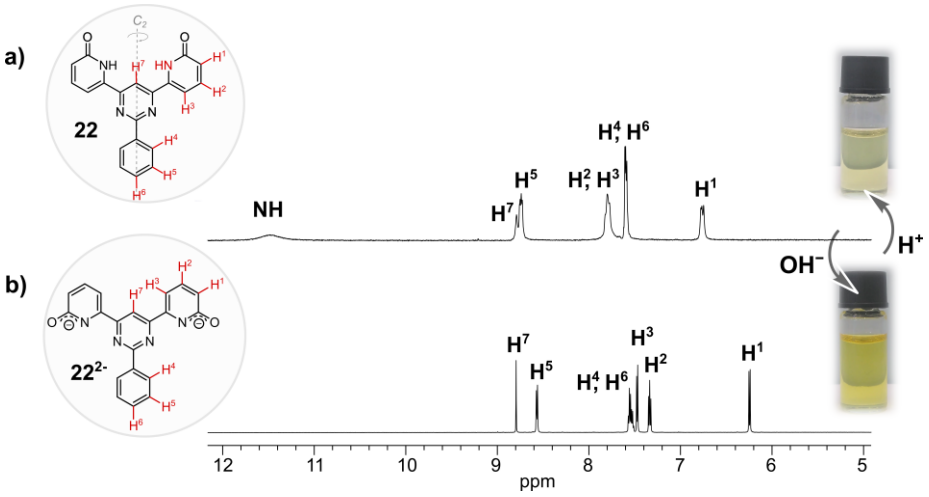

Figure 6. ^{1}H NMR (600 MHz) spectra at an ambient temperature of: (a) fully organic dynamer **22**; (b) **22**$^{2-}$ in form of a disodium salt.

Figure 6. Reversible changes in spectral characteristics, observed by both NMR and the naked eye, demonstrate the stimuli-responsiveness of the **22** polymer. Due to immediate colour change and no need for specific setup, this simple experiment shown the applicability of **22** as a colorimetric sensor for OH^- ions.

2.3 Coordination of 22 with metal ions

The anionic ligand **22**$^{2-}$ obtained by reaction with NaOH should react more strongly with a metal cation. More interestingly, the structure of complexes derived from amide anions is closer to iminolate than that of an amidate.[72-73] To test this hypothesis, the solution of **22**$^{2-}$ was treated with zinc tetrafluoroborate ($Zn(BF_4)_2$). After careful addition of HCl to neutralise the NaOH, the solution lost its colour vibrancy, and the NMR spectrum revealed very broad peaks with no recognisable multiplicity and two new broad signals at 11.3 and 11.8 ppm (see Figure 7). To explore the coordination possibilities of **22'**, a series of complexes were synthesised. Cu^{2+}, La^{3+}, Er^{3+}, and Zn^{2+} were first tested, and of the several methods, two were effective. Method A: Ligand **22** in DMSO was treated with metal salt, and the suspension was stirred at 130 °C for two days.

Method B: Ligand **22** in DMSO was first deprotonated by NaOH (aq), and after stirring at ambient temperature for 30 minutes, metal salt was added to the mixture. The mixture was then stirred for 1 day at ambient temperature

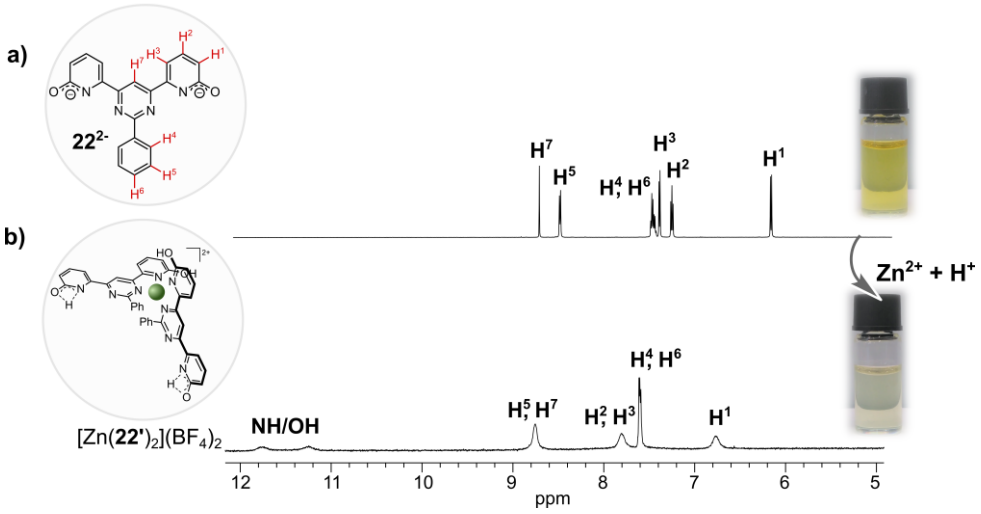

Figure 7. ^{1}H NMR (600 MHz) spectra at an ambient temperature of: (a) $\mathbf{22}^{2-}$ in form of disodium salt; (b) complex $[Zn(\mathbf{22'})_2](BF_4)_2$ in DMSO-d_6.

.

It was possible to isolate all four complexes as powders, but their solubility was even more limited than that of **22**; hence, their characterization and further investigation were much more challenging. The only characterization that was possible for all four complexes was the determination of their morphology by scanning electron microscopy (SEM; see Figure 8). Micrographs obtained from the Cu^{2+} complex sample revealed rather irregular blocks of different sizes; on the other hand, the Zn^{2+} complex consists of isolated elongated flat and thin blocks. Similar morphology was found within the La^{3+} complex, but the shape can be more accurately described as short and isolated needles. In the case of Er^{3+} it showed densely packed shapes similar to those of La^{3+} and Zn^{2+} complexes. To further investigate the composition of the prepared complexes, NMR and mass spectroscopy (MS) studies were performed. Unfortunately, due to the very low solubility, well-resolved NMR and MS spectra were obtained only from Zn^{2+} complex, and further investigation was focused on this complex.

As already mentioned, the NMR spectrum showed very broad peaks, with two new peaks at 11.3 and 11.8 ppm. At this chemical shift, peaks can be assigned to -NH of the amide form or -OH of the iminol form.

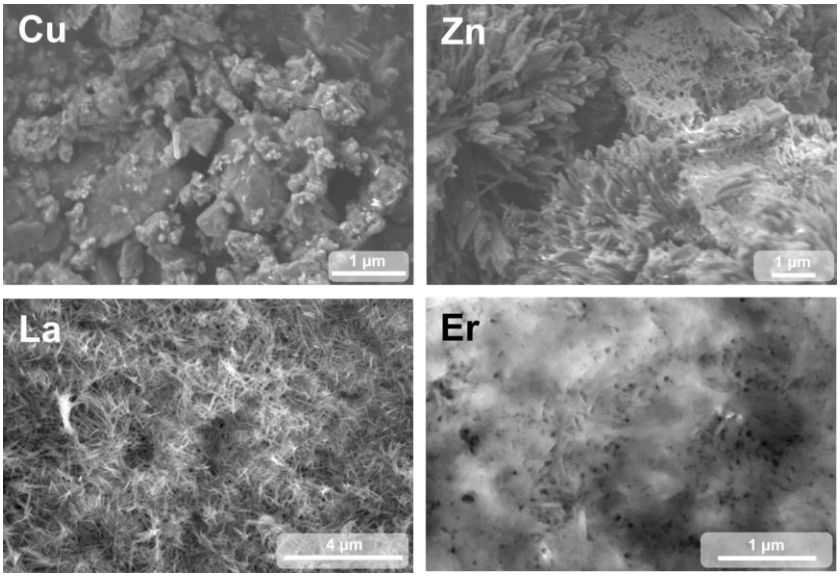

Figure 8 SEM micrographs of complexes formed by **22'** and metal cations (Cu^{2+}, La^{3+}, Er^{3+} and Zn^{2+}).

Existence of both means that, one 2-pyridone moiety is in the iminol form and is coordinated to the Zn^{2+} ion while the other moiety is still in the amide form. This partial tautomerization leading to desymmetrization of the molecule also explains the spectral width of the peaks. Concomitantly, in MALDI mass spectra, only the ML_2 type of complex has been identified.

We also noticed that the powders of **22** and $[Zn(\mathbf{22'})_2](BF_4)_2$ have slightly different colours under UV light. That led us to the thought that **22** can act as a sensor for Zn^{2+} cations. It was very important to show that switching between dynamer $(\mathbf{22})_n$ and complex $[Zn(\mathbf{22'})_2](BF_4)_2$ can be observed easily by a technique with an immediate answer, such as fluorescence spectroscopy. Since the solubility of both dynamer and complex is very low, fluorescence spectra were recorded in a solid state (Figure 9). $(\mathbf{22})_n$ fluorescence band maximum is centred at 555 nm, and after the complexation reaction with the Zn^{2+} metal ion, the band shifts to 578 nm. This simple experiment demonstrated how easy it is to distinguish between both species and that, basically, only a UV lamp is necessary to quickly confirm the presence of Zn^{2+} ions. Due to extremely low solubility, we were unable to grow a suitable crystal of $[Zn(\mathbf{22'})_2](BF_4)_2$, but it was crucial to determine the morphology and precise structure of this newly synthesised complex. B3LYP/6-31+G(d,p) molecular geometry optimisation provided some insights into the structure of the complex $[Zn(\mathbf{31'})_2](BF_4)_2$ and both **22** and **22'**. First, the method for **22** optimalization was perfected until the results matched the literature data. This method was

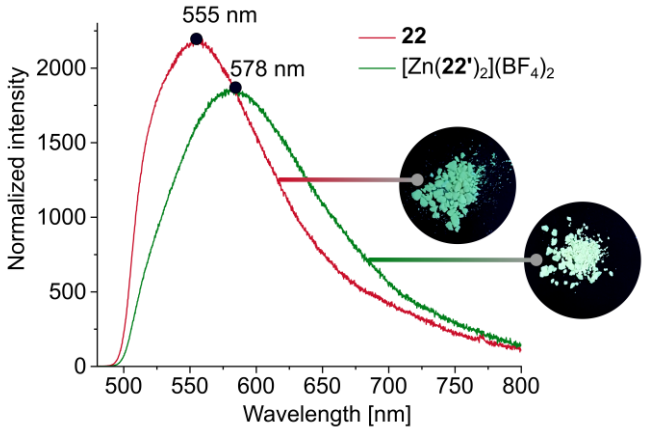

Figure 9 Fluorescence spectra of $(\mathbf{22})_n$ and $[Zn(\mathbf{22'})_2](BF_4)_2$ and photographs of both powders under λ = 365 nm light.

then used for **22'** optimalization. Using the stepwise method, the structure of the $[Zn(\mathbf{22'})_2]^{2+}$ ion was determined. These results showed that two **22** molecules coordinate the Zn^{2+} cation by pyrimidine-pyridine nitrogens to form a distorted tetrahedron with angles N(pyr)–Zn–N(pyr) 153°, N(py)–Zn–N(py) 105°, and N(pyr)–Zn–N(py) 81.5° and Zn–N(py) and Zn–N(pyr) bond lengths of 2.08 Å and 2.01 Å, respectively. Energy levels and the shape of the HOMO and LUMO orbitals can predict the properties of the molecule and also explain the overall look of the STM images (*vide infra*). According to our calculations, the orbitals of **22** have a symmetrical character. On the other hand, when coordination of Zn^{2+} ions occurs, the electron density of HOMO orbitals shifts towards the metal centre, and electron density of LUMO orbitals, is located on the outer part of the ligands (see Table 2).

Table 2 HOMO and LUMO orbitals of **22**, **22'** and $[Zn(\mathbf{22'})_2]^{2+}$

MO	22	22'	$[Zn(\mathbf{22'})_2]^{2+}$
LUMO	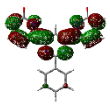	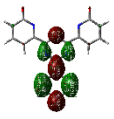	
HOMO	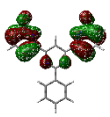	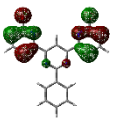	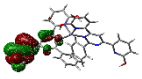

Curious about the secondary structure of $[Zn(\mathbf{22'})_2](BF_4)_2$, STM spectra were acquired. Images obtained by drop casting onto the HOPG surface revealed a well-ordered, repeating array of toroidal species (Figure 10). Overlaying the SMT image with calculated LUMO orbitals showed that the dark spots on the STM image represent part of the complex with the lowest electron density, and the bright rings around it represent part of the complex with high electron density. The measured in-plane lattice parameters of this structure are ~ 3.6 nm, which also fits well with the LUMO orbital analysis. As seen in Figure 10, a single ring consists of two molecules of the complex $[Zn(\mathbf{22'})_2](BF_4)_2$, that form a dimer by hydrogen bonds. These bonds are accessible since there are two 2-pyridone moieties in amide form present in the structure of $[Zn(\mathbf{22'})_2](BF_4)_2$ that are not involved in the Zn-coordination.

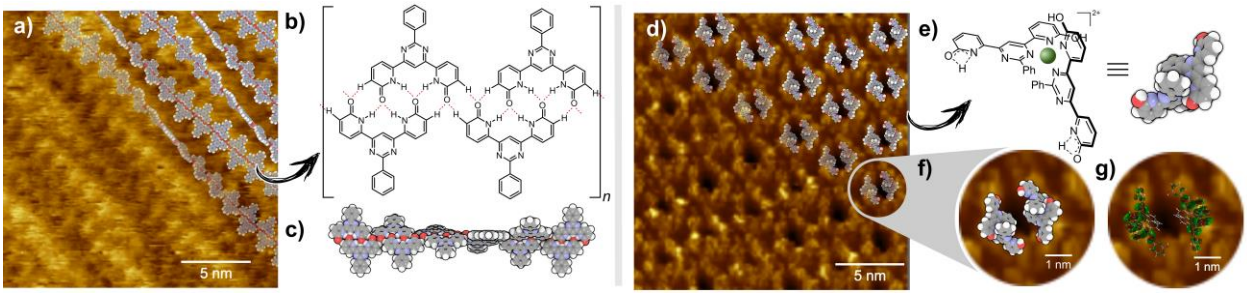

Figure 10 (a) STM image of a helical dynamer with model arranged on top of it. Image size: 20×20 nm²; V_{sample}=+0.6V; I_T = 0.1 nA; (b) chemical structure of **22** with presented H-bond motif; (c) model of helical dynamer **22**; (d) STM image of 2D an array formed by complex $[Zn(\mathbf{22'})_2](BF_4)_2$ with a model arranged on top of it. Image size: 20×20 nm²; V_{sample} = +0.6 V; I_T = 0.1 nA; (e) chemical structure of the cation $[Zn(\mathbf{22'})_2]^{2+}$ and its model; (f) zoomed area of STM image shown in (g). Image size: 5×5 nm² V_{sample} = +0.6 V; I_T = 0.1 nA; (i) zoomed area of STM image with model of LUMO orbitals on top of it. Image size: 5×5 nm²; V_{sample} = +0.6 V; I_T = 0.1 nA.

This part of the presented dissertation thesis provides a novel example of a dynamic ligand able to form both organic polymer and Zn^{2+} complex, that further assemble into hydrogen-bonded dimers. This multi-functionality of the same molecule allows reversible access to both organic dynamer and metallosupramolecular toroidal species by simple chemical stimuli such as metal ions, bases, and acid additions. We also demonstrated that simple 2-pyridone derivatives can be used as simple fluorescence sensors for Zn^{2+} ions and are well suited for the further generation of fluorescent adaptive materials.

A full description of the above project is presented in paper A1 (page 61) and in Supplementary Information A1 (page 67) which are part of this dissertation.

Miroslava Čonková, Wojciech Drożdż, Zygmunt Miłosz, Piotr Cecot, Jack Harrowfield, Mikołaj Lewandowski, Artur R. Stefankiewicz* *Influencing prototropy by metal ion coordination: supramolecular transformation of a dynamer into a Zn-based toroidal species,* Journal of Materials Chemistry C, **2021**, *9*, 3065-3069.

The project was carried out in cooperation with prof. Jack Harrowfield from the Institut de Science et d'Ingénieerie Supramoléculaires, Université de Strasbourg (France).

Chapter 3: 27@AuNPs for metal cation sensing

Sensors are systems or devices that can produce signals upon stimulation. Chemical sensors are basically measurement devices that convert the chemical or physical characteristics of an analyte into a signal. This dissertation includes a study that utilises the potential of metal ions to form complexes with *N*-acyl hydrazones to determine the trace metal content of the analyte of choice. Our goal was to produce a sensor that would be very versatile and highly sensitive. GNPs have been employed as colorimetric sensors of various compounds, from metal ions to antibodies, because of their characteristic surface plasmon resonance (SPR). When the shape, size, or surface properties of the GNP change, SPR changes can be easily quantified by Raman or UV-Vis spectroscopy. There are „on" and „off" states of gold nanoparticles: one when the particles are well dispersed, and the second, aggregated state. Aggregation alters the surface characteristics of the GNPs and shifts the SPR, which can also be visually observed as a colour change. In the literature, there are several examples of GNP-based sensors identifying various substances in aqueous samples; however, we choose to take a different approach. While trace metal content determination in water is highly practical, for example, for water quality control, sensing metal ions in organic media is an opportunity to develop a device that can be useful in the pharmaceutical and fine chemical industries. In both, catalytic processes are employed, and metal can be introduced into the final products of fine chemicals, active pharmaceutical ingredients (APIs), or an excipient used in a drug.[74] There are legal limits concerning transition metal contamination in APIs, regulated by European[40], British[75], Japanese[76], and United States[77] pharmacopoeias, which state that for orally administered drugs, metal content cannot be more than 10–20 ppm for most transition metals.[41] Producing organic waste with metal ions is another problem that results from metal catalysis. After a catalytic reaction, the work-up process might result in the loss of the catalyst and metal contamination of both organic and aqueous waste. To implement safe and environmentally friendly waste disposal, it is crucial to understand the composition of chemical waste. Environmental issues have concerned industry in general for some time. The importance of better environmental management is well illustrated by BASF, which has

prepared a tool for eco-efficiency analysis that includes environmental factors.[78] The goal was to develop a tool for decision-making processes that is applicable for many chemistry applications and will address issues like energy, toxicity, and material utilisation.

For both issues, quick and easy determination of transition metal content could be beneficial. Therefore, we decided to develop colorimetric sensors that could be easily used, directly in organic solvents during the production of different chemicals.

3.1 Synthesis of ligand 27

Ligand **27** was designed to combine both: a high affinity towards the gold surface and a versatile coordination pocket. To meet these requirements, **27** was derived from α-lipoic acid, often described as a capping agent for a gold surface.[79-82] *N*-acylhydrazone pocket[56,83-85] on the other hand, can efficiently bind metal cations. **27** was synthesised from α-lipoic acid (**23**) via a three-step protocol with a high 75% overall yield without column chromatography. In the first step, α-lipoic acid was converted to active ester **24** using *N*-hydroxysuccinimide (NHS) and *N*,*N*′-dicyclohexylcarbodiimide (DCC) in dichloromethane with an 82% yield. Next, the ester was converted acylhydrazone **25** in excellent 99% yield with hydrazine monohydrate in dichloromethane. Finally, the imine formation with salicylaldehyde (**26**) yielded **27** (93%, Scheme 14) as a mixture of two *cis*-*trans* isomers. The 2:1 ratio was calculated as the mean of the integrals of H-9$_{cis}$, H-9$_{trans}$, and H-11$_{cis}$, H-11$_{trans}$. The mixture of regioisomers was used as prepared. It was reported that α-lipoic acid and its derivatives forms complexes with metal ions via disulfide-metal interaction[86-87]; moreover several derivatives were even proved to act successfully in the treatment of heavy metal poisoning[88-90]. For testing the

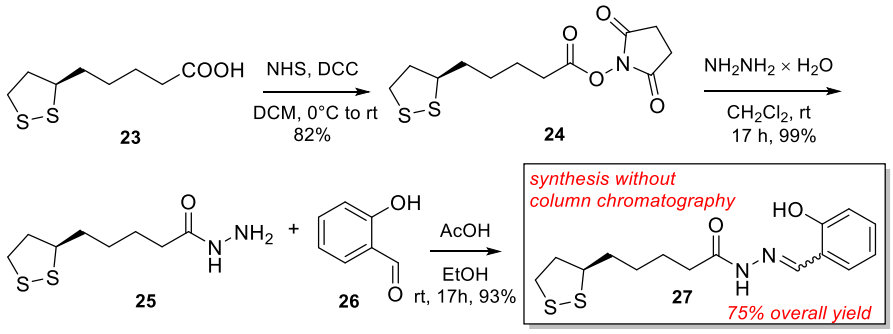

Scheme 14 Syntheis of **27**.

effectiveness of the prepared *N*-acylhydrazone chelating system, a simpler, literature known ligand **28** (structure in Figure 11) was synthesised to prevent these potential conflicting interactions between metal ions and the unbound disulphide.

On the assumption that the ligand will react as a tridentate chelate, **28** was first reacted with a number of metal ions (Ag^{+}, Al^{3+}, Cd^{2+}, Ce^{3+}, Co^{2+}, Cu^{2+}, Fe^{3+}, and Ni^{2+}), all as nitrate salts in a M:L molar ratio of 1:2. Reactions were conducted in acetonitrile, and the products were isolated as powders by recrystallization from diethyl ether. The coordination reaction yielded in complexes only in three cases (Cu^{2+}, Ni^{2+}, and Fe^{3+}) with 71-85% yield/efficiency. The structure of these complexes was then determined by individual ESI-MS mass spectra, where signals assigned to [M(**28**)$_2$] (M = Cu, Ni) and [M(**28**)$_2$]$^{+}$ (M = Fe) were identified showing octahedral geometry of formed complexes. With metal coordination efficiency and selectivity experiments of *N*-acylhydrazone moiety in hand, synthesis of metal nanoparticles and determination of capability of α-lipoic acid moiety to form Au-S linkage on the gold surface were conducted.

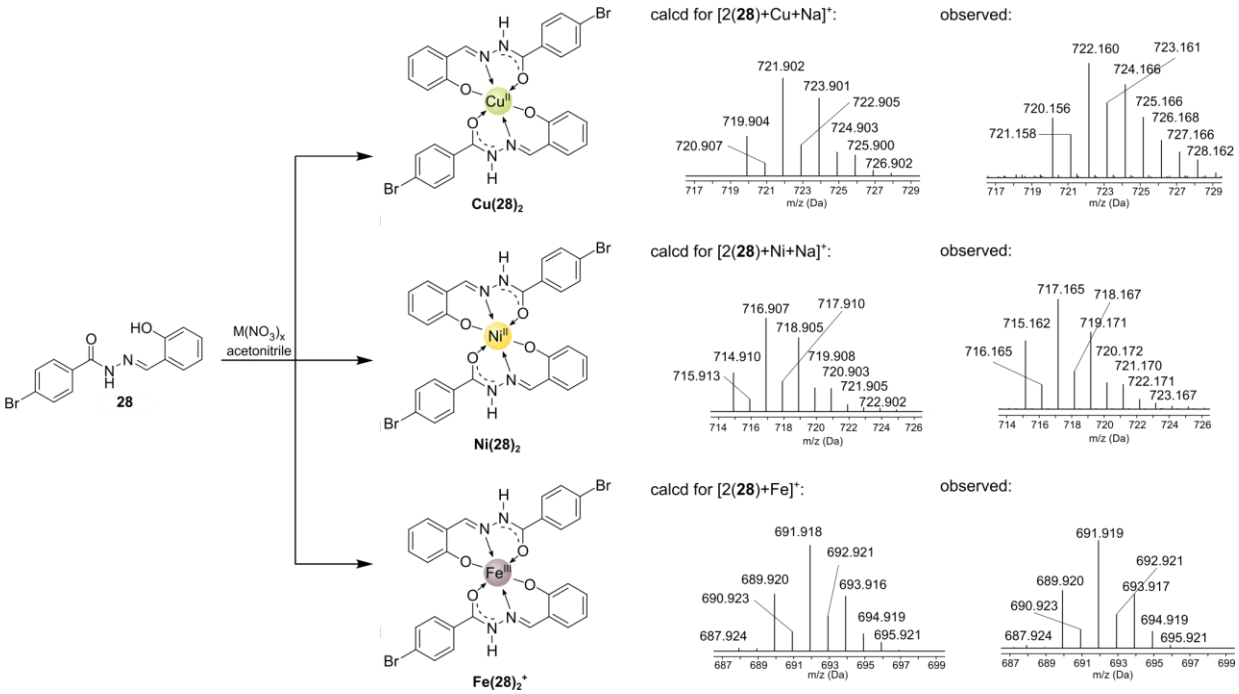

Figure 11 Synthesis of M(**28**)$_2$ complexes (M = Cu^{2+}, Ni^{2+}, Fe^{3+}) and mass spectra confirming their structure.

3.2 Gold nanoparticle synthesis and ligand exchange reaction

For application in metal sensing in post-catalytic reaction mixtures, gold nanoparticle synthesis was directed toward compatibility with organic solvents. Li et all[91] reported the synthesis of monodispersed gold nanoparticles stable in toluene for up to several weeks that utilise oleylamine as a surfactant, solvent, and reducing agent. With the mentioned stability and simple experimental set-up, we prepared oleylamine-capped gold nanoparticles (**OL**@AuNPs) according to the described protocol.[91] At first glance, the specific red colour of the obtained solution indicated the generation of gold nanoparticles, and UV-Vis spectra displayed a characteristic band at 526 nm, ascribed to the dipole resonance of individual AuNPs. The amine group interacts with the gold surface in a generally weaker way than the dative Au-S bond[92], which is expected to promote exchange between the two molecules. During the project, this step was found to be the most challenging. After numerous disappointing attempts, leading to quick aggregation of AuNPs, we learned that a specific concentration window of **27** is essential for a successful ligand exchange reaction. To overcome this problem, we chose the concentration of **27** according to the roughly calculated number of binding sites on the surface of GNPs. The number of binding sites was estimated to be 4.5 binding sites per nm^2, which is the maximum molecular density of the alkanethiol self-assembled monolayer (SAM), based on the tight-packed spherical model proposed by Murray and coworkers,[93] according to which gold nanoparticles have a densely packed core with a density of 59 atoms/nm^3,[93-94]. Each nanoparticle has a core of around 31 d^3 Au atoms, and the theoretical number of binding sites per nanoparticle was determined to be about 14.7 d^2 under the assumption that the capping agent is distributed uniformly across the nanoparticle surface. These calculations suggest that 890 molecules of the **27** molecules per nanoparticle need be added in order to carry out the ligand exchange reaction.

The concentration of **27** was then set up to 7.5 μM, 15 μM, 30 μM, and 60 μM, and the stock **OL**@AuNPs solution concentration was set to 1 mM (in toluene, in terms of metal). UV-Vis spectroscopy was used to observe the exchange reaction over a certain amount of time ranging from 1 hour to 96 hours.

At concentration [**27**] = 7.5 μM, a 3–4 nm shift in the localised surface plasmon resonance (LSPR) band was observed after one hour. Although the LSPR band was stable for 96 hours, there was a small band widening after 24 hours. Similar behaviour could be observed in the UV-Vis spectra at a concentration of [**27**] = 15 μM. A 4-5 nm LSPR band shift occurred after three hours, and no aggregation was identified during the whole of the observation period (96 hours). The ligand concentration was increased to 30 μM and 60 μM in the exchange process to enhance the number of receptors on the gold surface. Unfortunately, the LSPR band shift was rapidly shifting in both instances, leading to rapid aggregation that was evident to the naked eye as a colour change from red to violet-blue and an LSPR band shift up to 106 nm. These tests shown that reactions using **27** at a concentration of 15 μM produced stable gold nanoparticles with the greatest possible number of receptors.

3.3 Morphology study

Transmission electron microscopy (TEM) and dynamic light scattering measurements (DLS) were used to study the size and shape of both **OL**@AuNPs and **27**@AuNPs (Figure 12). TEM

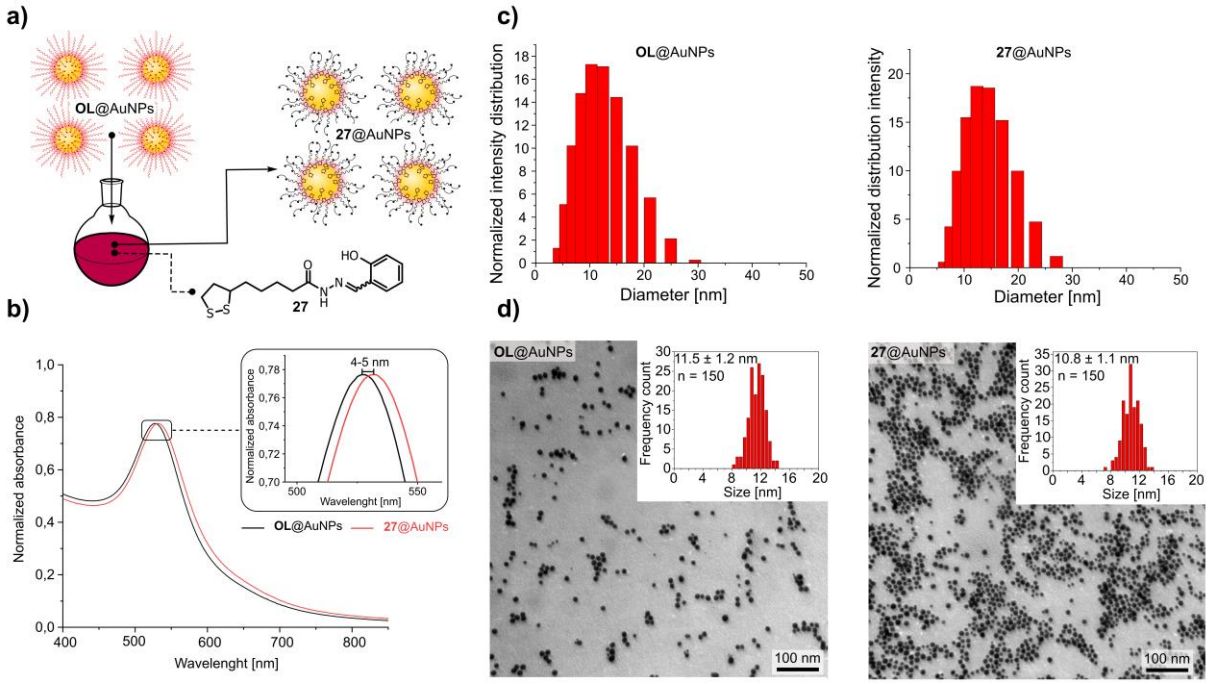

Figure 12 a) representation of ligand exchange reaction; b) UV-Vis comparison of **OL**@AuNPs and **27**@AuNPs; c) DLS comparison of **OL**@AuNPs and **27**@AuNPs d) TEM comparison of **OL**@AuNPs and **27**@AuNPs.

pictures of monodispersed gold nanoparticles with a uniform shape and a core size of 11.5±1.2 nm were obtained by drop casting a diluted solution of **OL**@AuNPs onto a copper grid. In DLS measurements, slightly bigger solvodynamic diameter was observed: 14.3±4.38 nm (PdI: 0.186; calculated for n = 5 measurements), which is consistent with the presence of oleylamine on the surface of gold nanoparticles and molecules of solvent surrounding the GNPs.

As seen in TEM images of **27**@AuNPs, which showed firmly packed gold nanoparticles with an unchanged size of metal core 10.8±1.1 nm, Ligand **27** is not likely to change the NP size. DLS observations of **27**@AuNPs reveal an average solvodynamic diameter of 15.45±4.26 nm (PdI: 0.243; estimated for n = 5 measurements). It is also important to note that none of the samples developed aggregates in any of the DLS experiments at the concentration of 0.25 mM.

3.4 Metal sensing properties of GNPs

The next crucial step was to evaluate the sensitivity of the newly prepared sensor for selected transition metal ions in a toluene-acetonitrile solution. First, it was important to set up the experiment correctly; therefore, non-specific aggregation caused by acetonitrile had to be ruled out first. Upon incremental addition of acetonitrile, UV-Vis spectra revealed that the **27**@AuNPs solution is stable up to 23% v/v of acetonitrile. On the same note, to be sure that metals react to receptors on the surface and not with the gold surface itself, it was necessary to test how selected metal ions interact with gold nanoparticles without these receptors (**OL**@AuNPs). The solution of **OL**@AuNPs remained stable in all tested conditions, up to metal ion concentration c = 10 μM (no change in LSPR was detected).

Activity of **27**@AuNPs toluene solution was determined via titration with an acetonitrile solution of selected metal ions in the form of nitrate salts (Cu^{2+}, Ni^{2+}, and Fe^{3+}), and LSPR band change was measured by UV-Vis spectroscopy.

To create 1-10 M solutions of metal salts, aliquots of a 0.1 mM acetonitrile solution of metal salt were added to 0.25 mM gold colloidal dispersions. As apparent from Figure 13, the addition of Cu^{2+}, Ni^{2+}, and Fe^{3+} ions caused the LSPR band of the sensor (**27**@AuNPs) to shift to the higher wavelengths. In detail: when Cu^{2+} ion concentrations range from 1 μM to 5 μM, the LSPR band was changing slowly (0.5–1 nm between each concentration) until c (Cu^{2+}) = 7.5 μM and 10 μM, where the shift of LSPR was approximately 12 nm (Figure 13a).

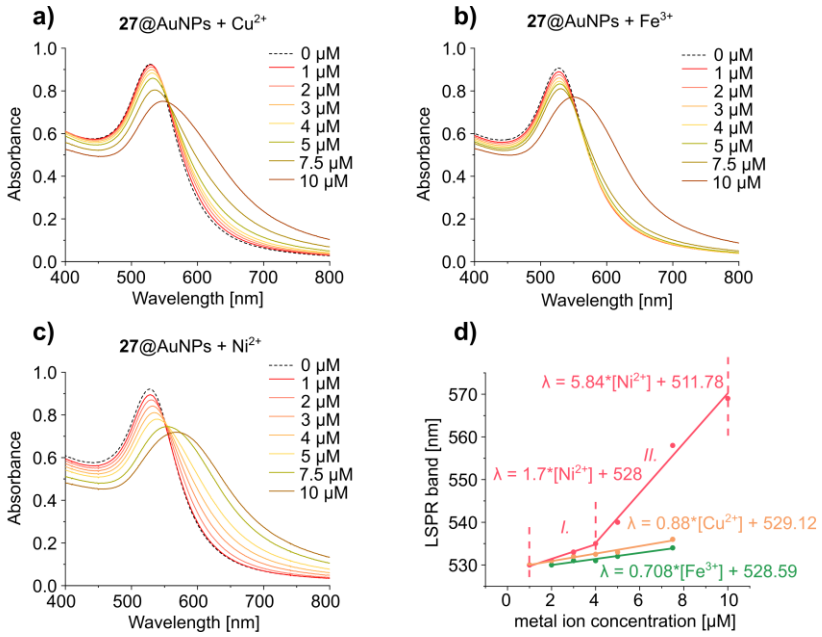

Figure 13 a) UV-Vis spectrum showing LSPR band shift upon addition of Cu^{2+}; b) Fe^{3+}; c) Ni^{2+}; d) linear change of LSPR maximum plotted as a function of metal ion concentration.

Similar behaviour was observed upon the addition of Fe^{3+} ions (see Figure 13b). The maximum sensing capability of **27**@AuNPs was demonstrated for the Ni^{2+} ion detection. Compared to the other metals more notable LSPR shift was seen at a concentration of 4 μM of Ni^{2+}. The LSPR band shift changed more quickly in the 4–10 μM range as seen in Figure 13d. Additionally, for all of the measured metal ions, the colour of the sensor changed from red to violet upon the addition of a transition metal ion in the concentration range of 5-7.5 μM. Visible colour change is result of aggregation of the nanoparticles, that comes from the formation of the octahedral complex of metal ions and *N*-acylhydrazone moieties present at the particle surface (Scheme 15).

The result demonstrates, that the as-prepared sensor could be simply observed by the naked eye and would be a feasible colorimetric method for the determination of Cu^{2+}, Ni^{2+}, and Fe^{3+} ions in organic solvents. The limit of detection for all tested metal ions was determined by plotting known concentrations of Cu^{2+}, Ni^{2+}, or Fe^{3+} ions (1–10 μM) against the LSPR maximum (Figure 13d). The linear response was fitted to the formula: $LSPR_{max}$ = a*[metal ion + b], and the limit of detection (LoD) of each metal ion was calculated using the $3SB/m^{95}$ equation, (SB = standard deviation of a blank sample, m = slope of each calibration curve).

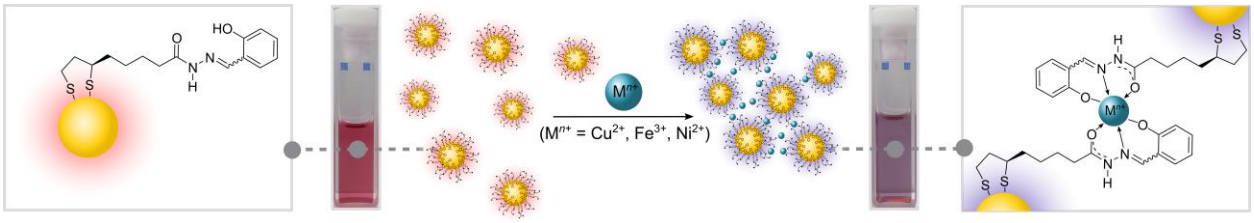

Scheme 15 Coordination triggered aggregation of **27** capped gold nanoparticles.

The **27**@AuNPs sensor showed very low LoDs that ranging from 1.4 to 11.2 nM for the investigated metal ions. Sensitivities (S) in the case of Cu^{2+} and Fe^{3+} cations are very similar: S = 0.88 and 0.71 μM^{-1}, respectively. In the case of the most catalytically valuable of all studied cations – Ni^{2+} sensitivity is much higher. In the first region (c = 1-4 μM), S = 1.7 μM^{-1}, and in the second region (c = 4-10 μM), S was determined as 5.84 μM^{-1} (Figure 13d).

3.5 Real sample analysis

Nickel catalysis is both environmentally and economically advantageous, which leads to a higher demand for the utilisation of nickel catalysts in the pharmaceutical industry.[96] Comparing to the most commonly used palladium and nickel, it has been estimated that the global warming potential (GWP) for the production of 1 kg of palladium is 3880 kg equivalents of CO_2 (e-CO_2), while for the production of 1 kg of nickel, the GWP is 6.5 kg e-CO_2.[97] Ni-catalysed reactions are used in the synthesis of several valuable molecules, including pictilisib44[98] (PI3K inhibitor developed by Genentech) or PDE47245[99] (an inhibitor of phosphodiesterase type 4D developed by Novartis Pharma AG). It was important to demonstrate that our sensor can be used for the determination of metal waste content in post-catalytic reactions such as C-C coupling used for the synthesis of mentioned PDE47245. We decided to reproduce the synthetic protocol for nickel-catalysed Kumada coupling that was used in synthesis of PDE472, reported by Novartis Pharma AG. After the reaction, purification of the product as described by Novartis Pharma AG was performed, and organic waste that included traces of nickel in toluene was analysed by UV-Vis spectroscopy. To compare the reliability of the data, metal content was also determined by inductively coupled plasma mass spectrometry (ICP-MS).

10 minutes after the toluene waste (50 μL) was added to the **27**@AuNPs dispersion, the UV-vis spectrum was recorded and showed a 4 nm red shift of the LSPR band. From the

calibration curve obtained from the metal sensing experiments (*vide supra)*, the concentration of nickel ions was evaluated at 3.5 μM (the evaluation is approximation since a 1 nm difference equals concentration difference of 0.5 μM). The nickel content was determined from the same organic waste by ICP-MS, and the metal content was determined at 3.49 μM. It is good to highlight that for ICP-MS measurements, the organic waste had to be evaporated, dried, and mineralized prior to measurement. This procedure took several hours in total, while UV-Vis measurement have been done right after purification, directly from the solution, and the total analysis time was reduced to approximately 15 minutes.

Chemical change upon metal ion addition was observed after around 10 minutes, which makes it suitable for on-the-spot qualitative sensing. The sensitivity of **27**@AuNPs was excellent for all studied ions, especially the catalytically most valuable Ni^{2+} ions, and the colorimetric response visible by the naked eye was 204 ppb, which is two orders of magnitude lower than the EU recommended limits (366 ppb for Cu^{2+} colorimetric sensing and 458 ppb for Fe^{3+} colorimetric sensing). Furthermore, LoDs for all studied ions were determined and are in the nanomolar range. In general, we showed how the coordination ability of Schiff bases can be translated into a highly efficient, versatile, and applicable sensing device.

A full description of the above project is presented in paper A2 (page 92) and in Supplementary Information A2 (page 97) which are part of this dissertation.

Miroslava Čonková#, Verónica Montez-Garcia#, Marcin Konopka, Artur Cieselski*, Paolo Samori*, Artur R. Stefankiewicz* *Schiff base caped gold nanoparticles for transition metal cations sensing in organic media*, Chemical Communications, **2022**, *58 (38)*, 5773-5776.

The project was carried out in cooperation with prof. Paolo Samori and visiting prof. Artur Ciesielski from the Institut de Science et d'Ingénieerie Supramoléculaires, Université de Strasbourg (France).

Conclusion

In the presented thesis, systems based on hydrogen and coordination bonds were discussed. A brief introduction offered a simple explanation of the responsiveness of non-covalent architectures and a summary of their utilisation and application. The intention was to draw attention to gaps in the literature and show opportunities for our research.

The main part of the thesis are two reports in international scientific journals (Chemical Communications, and Journal of Materials Chemistry C), discussing the potential of non-covalent interactions for building functional assemblies. We designed, synthesised, and characterised molecules that form intermolecular hydrogen bonds (A1) and coordination bonds (A1 and A2). These molecules were tailor-made to deliver specific responses that were: a) unique and new to the literature; b) easily measurable by benchtop spectroscopic methods and/or the naked eye; c) suitable to produce stimuli-responsive assemblies for either the development of smart materials or sensors. The characterization of these novel molecules was focused on describing both the „off" and „on" states of the system in solution and on the surface using a wide set of spectroscopic and microscopic techniques. The applicability of the described molecules was explored in the area of optical detection for metal ion.

References

1. Staudinger, H., *Arbeitserinnerungen*. Alfred Hüthig: Heidelberg, 1961.
2. Mülhaupt, R., Hermann Staudinger and the Origin of Macromolecular Chemistry. *Angewandte Chemie International Edition* **2004,** *43* (9), 1054-1063.
3. Carothers, W. H. Linear Condenzation Polymers. US2071250A, 1937.
4. Carothers, W. H. Linear polyamides and their production. US2130523A, 1938.
5. Zhang, M.; Biesold, G. M.; Choi, W.; Yu, J.; Deng, Y.; Silvestre, C.; Lin, Z., Recent advances in polymers and polymer composites for food packaging. *Materials Today* **2022,** *53*, 134-161.
6. Liechty, W. B.; Kryscio, D. R.; Slaughter, B. V.; Peppas, N. A., Polymers for drug delivery systems. *Annu Rev Chem Biomol Eng* **2010,** *1*, 149-73.
7. Lehn, J.-M., *Supramolecular Chemistry: Concepts and Perspectives*. Wiley: Weinheim, 1995.
8. Kumar, A. M.; Sivakova, S.; Fox, J. D.; Green, J. E.; Marchant, R. E.; Rowan, S. J., Molecular engineering of supramolecular scaffold coatings that can reduce static platelet adhesion. *J Am Chem Soc* **2008,** *130* (4), 1466-76.
9. Besenius, P.; Portale, G.; Bomans, P. H.; Janssen, H. M.; Palmans, A. R.; Meijer, E. W., Controlling the growth and shape of chiral supramolecular polymers in water. *Proc Natl Acad Sci U S A* **2010,** *107* (42), 17888-93.
10. Park, T.; Zimmerman, S. C., A supramolecular multi-block copolymer with a high propensity for alternation. *J Am Chem Soc* **2006,** *128* (43), 13986-7.
11. Yang, S. K.; Zimmerman, S. C., Hydrogen Bonding Modules for Use in Supramolecular Polymers. *Israel Journal of Chemistry* **2013,** *53* (8), 511-520.
12. Djurdjevic, S.; Leigh, D. A.; McNab, H.; Parsons, S.; Teobaldi, G.; Zerbetto, F., Extremely strong and readily accessible AAA-DDD triple hydrogen bond complexes. *J Am Chem Soc* **2007,** *129* (3), 476-7.
13. Prabhakaran, P.; Puranik, V. G.; Sanjayan, G. J., Preorganizing linear (self-complementary) quadruple hydrogen-bonding arrays using intramolecular hydrogen bonding as the sole force. *J Org Chem* **2005,** *70* (24), 10067-72.
14. Yang, Y.; Yang, Z. Y.; Yi, Y. P.; Xiang, J. F.; Chen, C. F.; Wan, L. J.; Shuai, Z. G., Helical molecular duplex strands: multiple hydrogen-bond-mediated assembly of self-complementary oligomeric hydrazide derivatives. *J Org Chem* **2007,** *72* (13), 4936-46.
15. Mayer, M. F.; Nakashima, S.; Zimmerman, S. C., Synthesis of a soluble ureido-naphthyridine oligomer that self-associates via eight contiguous hydrogen bonds. *Org Lett* **2005,** *7* (14), 3005-8.
16. Archer, E. A.; Sochia, A. E.; Krische, M. J., The Covalent Casting of One-Dimensional Hydrogen Bonding Motifs: Toward Oligomers and Polymers of Predefined Topography. *Chemistry* **2001,** *7* (10), 2059-2066.
17. Pantoş, G. D.; Pengo, P.; Sanders, J. K. M., Hydrogen-Bonded Helical Organic Nanotubes. *Angewandte Chemie* **2007,** *119* (1-2), 198-201.
18. Pantos, G. D.; Wietor, J. L.; Sanders, J. K., Filling helical nanotubes with C60. *Angew Chem Int Ed Engl* **2007,** *46* (13), 2238-40.

19. Kulkarni, C.; Meijer, E. W.; Palmans, A. R. A., Cooperativity Scale: A Structure-Mechanism Correlation in the Self-Assembly of Benzene-1,3,5-tricarboxamides. *Acc Chem Res* **2017,** *50* (8), 1928-1936.
20. Perlitius, F.; Walczak, A.; Čonková, M.; Markiewicz, G.; Harrowfield, J.; Stefankiewicz, A. R., Dimeric capsule vs columnar polymer: Structural factors determining the aggregation behavior of amino acid functionalized benzene-1,3,5-tricarboxamides in solution and in the solid-state. *Journal of Molecular Liquids* **2022,** *367*, 120511.
21. Desmarchelier, A.; Alvarenga, B. G.; Caumes, X.; Dubreucq, L.; Troufflard, C.; Tessier, M.; Vanthuyne, N.; Ide, J.; Maistriaux, T.; Beljonne, D.; Brocorens, P.; Lazzaroni, R.; Raynal, M.; Bouteiller, L., Tuning the nature and stability of self-assemblies formed by ester benzene 1,3,5-tricarboxamides: the crucial role played by the substituents. *Soft Matter* **2016,** *12* (37), 7824-7838.
22. Markiewicz, G.; Jenczak, A.; Kolodziejski, M.; Holstein, J. J.; Sanders, J. K. M.; Stefankiewicz, A. R., Selective C70 encapsulation by a robust octameric nanospheroid held together by 48 cooperative hydrogen bonds. *Nat Commun* **2017,** *8*, 15109.
23. Leenders, C. M.; Baker, M. B.; Pijpers, I. A.; Lafleur, R. P.; Albertazzi, L.; Palmans, A. R.; Meijer, E. W., Supramolecular polymerisation in water; elucidating the role of hydrophobic and hydrogen-bond interactions. *Soft Matter* **2016,** *12* (11), 2887-93.
24. Leenders, C. M.; Albertazzi, L.; Mes, T.; Koenigs, M. M.; Palmans, A. R.; Meijer, E. W., Supramolecular polymerization in water harnessing both hydrophobic effects and hydrogen bond formation. *Chem Commun (Camb)* **2013,** *49* (19), 1963-5.
25. Albertazzi, L.; van der Zwaag, D.; Leenders, C. M.; Fitzner, R.; van der Hofstad, R. W.; Meijer, E. W., Probing exchange pathways in one-dimensional aggregates with super-resolution microscopy. *Science* **2014,** *344* (6183), 491-5.
26. Bochicchio, D.; Pavan, G. M., Effect of Concentration on the Supramolecular Polymerization Mechanism via Implicit-Solvent Coarse-Grained Simulations of Water-Soluble 1,3,5-Benzenetricarboxamide. *J Phys Chem Lett* **2017,** *8* (16), 3813-3819.
27. Fuentes, E.; Gerth, M.; Berrocal, J. A.; Matera, C.; Gorostiza, P.; Voets, I. K.; Pujals, S.; Albertazzi, L., An Azobenzene-Based Single-Component Supramolecular Polymer Responsive to Multiple Stimuli in Water. *J Am Chem Soc* **2020,** *142* (22), 10069-10078.
28. Yano, K.; Itoh, Y.; Araoka, F.; Watanabe, G.; Hikima, T.; Aida, T., Nematic-to-columnar mesophase transition by in situ supramolecular polymerization. *Science* **2019,** *363* (6423), 161-165.
29. Stoncius, S.; Orentas, E.; Butkus, E.; Ohrstrom, L.; Wendt, O. F.; Warnmark, K., An approach to helical tubular self-aggregation using C2-symmetric self-complementary hydrogen-bonding cavity molecules. *J Am Chem Soc* **2006,** *128* (25), 8272-85.
30. Saied, O.; Maris, T.; Wuest, J. D., Deformation of porous molecular networks induced by the exchange of guests in single crystals. *J Am Chem Soc* **2003,** *125* (49), 14956-7.
31. Wang, X.; Simard, M.; Wuest, J. D., Molecular Tectonics. Three-Dimensional Organic Networks with Zeolitic Properties. *Journal of the American Chemical Society* **1994,** *116* (26), 12119-12120.
32. Kumpfer, J. R.; Jin, J.; Rowan, S. J., Stimuli-responsive europium-containing metallo-supramolecular polymers. *J. Mater. Chem.* **2010,** *20* (1), 145-151.

33. Adarsh, N. N.; Dastidar, P., Coordination polymers: what has been achieved in going from innocent 4,4'-bipyridine to bis-pyridyl ligands having a non-innocent backbone? *Chem Soc Rev* **2012,** *41* (8), 3039-60.
34. Leong, W. L.; Vittal, J. J., One-dimensional coordination polymers: complexity and diversity in structures, properties, and applications. *Chem Rev* **2011,** *111* (2), 688-764.
35. Lu, Z. Z.; Zhang, R.; Li, Y. Z.; Guo, Z. J.; Zheng, H. G., Solvatochromic behavior of a nanotubular metal-organic framework for sensing small molecules. *J Am Chem Soc* **2011,** *133* (12), 4172-4.
36. Warad, I., Hemilabile trans/cis-isomerism in [(P∩OO)2RuCl2(N∩N)], XRD/HSA-interactions, C–H···Cl-Ru(II) supramolecular synthon, solvatochromism, thermal and A DFT/TD-DFT computation. *Journal of Molecular Liquids* **2021,** *328*, 115482.
37. McKenzie, B. M.; Wojtecki, R. J.; Burke, K. A.; Zhang, C.; Jákli, A.; Mather, P. T.; Rowan, S. J., Metallo-Responsive Liquid Crystalline Monomers and Polymers. *Chemistry of Materials* **2011,** *23* (15), 3525-3533.
38. Oehme, I.; Wolfbeis, O. S., Optical sensors for determination of heavy metal ions. *Mikrochimica Acta* **1997,** *126* (3-4), 177-192.
39. Kaur, B.; Kaur, N.; Kumar, S., Colorimetric metal ion sensors – A comprehensive review of the years 2011–2016. *Coordination Chemistry Reviews* **2018,** *358*, 13-69.
40. E.D.f.t.Q.o.M., C. o. E. *European Pharmacopoeia*; Strasbourg, 2006.
41. European Medicine Agency, C. f. H. M. P. *ICH guideline Q3D (R1) on elemental impurities*; 2019.
42. Priyadarshini, E.; Pradhan, N., Gold nanoparticles as efficient sensors in colorimetric detection of toxic metal ions: A review. *Sensors and Actuators B: Chemical* **2017,** *238*, 888-902.
43. Winkler, J. D.; Bowen, C. M.; Michelet, V., Photodynamic Fluorescent Metal Ion Sensors with Parts per Billion Sensitivity. *Journal of the American Chemical Society* **1998,** *120* (13), 3237-3242.
44. Wang, L.; Wang, Y.; Li, W.; Zhi, W.; Liu, Y.; Ni, L.; Wang, Y., Recyclable DNA-Derived Polymeric Sensor: Ultrasensitive Detection of Hg(II) Ions Modulated by Morphological Changes. *ACS Appl Mater Interfaces* **2019,** *11* (43), 40575-40584.
45. Jia, H.; Li, Z.; Wang, X.; Zheng, Z., Facile functionalization of a tetrahedron-like PEG macromonomer-based fluorescent hydrogel with high strength and its heavy metal ion detection. *Journal of Materials Chemistry A* **2015,** *3* (3), 1158-1163.
46. Koenigs, W.; Koerner, G., Ueber Oxycinchoninsäure und Oxychinolinsäure. *Berichte der deutschen chemischen Gesellschaft* **1883,** *16* (2), 2152-2160.
47. Aue, D. H.; Betowski, L. D.; Davidson, W. R.; Bowers, M. T.; Beak, P.; Lee, J., Gas-phase basicities of amides and imidates. Estimation of protomeric equilibrium constants by the basicity method in the gas phase. *Journal of the American Chemical Society* **1979,** *101* (6), 1361-1368.
48. Albert, A.; Phillips, J. N., 264. Ionization constants of heterocyclic substances. Part II. Hydroxy-derivatives of nitrogenous six-membered ring-compounds. *Journal of the Chemical Society (Resumed)* **1956**, 1294.
49. Waring, A.; Forlani, L.; Cristoni, G.; Boga, C.; Todesco, P. E.; Vecchio, E. D.; Selva, S.; Monari, M., Reinvestigation of the tautomerism of some substituted 2-hydroxypyridines. *Arkivoc* **2002,** *2002* (11), 198-215.

50. Hagimori, M.; Mizuyama, N.; Yamaguchi, Y.; Saji, H.; Tominaga, Y., A novel small molecule fluorescent sensor for Zn2+ based on pyridine-pyridone scaffold. *Talanta* **2011,** *83* (5), 1730-5.
51. Hagimori, M.; Uto, T.; Mizuyama, N.; Temma, T.; Yamaguchi, Y.; Tominaga, Y.; Saji, H., Fluorescence ON/OFF switching Zn2+ sensor based on pyridine–pyridone scaffold. *Sensors and Actuators B: Chemical* **2013,** *181*, 823-828.
52. Hagimori, M.; Mizuyama, N.; Tominaga, Y.; Mukai, T.; Saji, H., A low-molecular-weight fluorescent sensor with Zn2+ dependent bathochromic shift of emission wavelength and its imaging in living cells. *Dyes and Pigments* **2015,** *113*, 205-209.
53. Hagimori, M.; Temma, T.; Mizuyama, N.; Uto, T.; Yamaguchi, Y.; Tominaga, Y.; Mukai, T.; Saji, H., A high-affinity fluorescent Zn2+ sensor improved by the suppression of pyridine-pyridone tautomerism and its application in living cells. *Sensors and Actuators B: Chemical* **2015,** *213*, 45-52.
54. Wu, D. L.; Liu, L.; Liu, G. F.; Jia, D. Z., Ab initio/DFT and AIM studies on dual hydrogen-bonded complexes of 2-hydroxypyridine/2-pyridone tautomerism. *J Phys Chem A* **2007,** *111* (24), 5244-52.
55. Ciesielski, A.; Stefankiewicz, A. R.; Hanke, F.; Persson, M.; Lehn, J.-M.; Samorì, P., Rigid Dimers Formed through Strong Interdigitated H-Bonds Yield Compact 1D Supramolecular Helical Polymers. *Small* **2011,** *7* (3), 342-350.
56. Stadler, A.-M.; Harrowfield, J., Bis-acyl-/aroyl-hydrazones as multidentate ligands. *Inorganica Chimica Acta* **2009,** *362* (12), 4298-4314.
57. Han, A.; Su, H.; Xu, G.; Khan, M. A.; Li, H., Synthesis, crystal structures, and luminescent properties of Zn(ii), Cd(ii), Eu(iii) complexes and detection of Fe(iii) ions based on a diacylhydrazone Schiff base. *RSC Advances* **2020,** *10* (39), 23372-23378.
58. Gupta, V. K.; Singh, A. K.; Ganjali, M. R.; Norouzi, P.; Faridbod, F.; Mergu, N., Comparative study of colorimetric sensors based on newly synthesized Schiff bases. *Sensors and Actuators B: Chemical* **2013,** *182*, 642-651.
59. Sun, H.; Jiang, Y.; Nie, J.; Wei, J.-H.; Miao, B. X.; Zhao, Y.; Zhang, L.-F.; Ni, Z.-H., Multifunctional AIE-ESIPT dual mechanism tetraphenylethene-based Schiff base for inkless rewritable paper and colorimetric/fluorescent dual-channel Zn2+ sensor. *Materials Chemistry Frontiers* **2020**.
60. Liao, Z.; Liu, Y.; Han, S.-F.; Wang, D.; Zheng, J.-Q.; Zheng, X.-J.; Jin, L.-P., A novel acylhydrazone-based derivative as dual-mode chemosensor for Al3+, Zn2+ and Fe3+ and its applications in cell imaging. *Sensors and Actuators B: Chemical* **2017,** *244*, 914-921.
61. Wei, T.-B.; Zhang, P.; Shi, B.-B.; Chen, P.; Lin, Q.; Liu, J.; Zhang, Y.-M., A highly selective chemosensor for colorimetric detection of Fe3+ and fluorescence turn-on response of Zn2+. *Dyes and Pigments* **2013,** *97* (2), 297-302.
62. Papavassiliou, G. C., Optical properties of small inorganic and organic metal particles. *Progress in Solid State Chemistry* **1979,** *12* (3-4), 185-271.
63. Lu, F.; Yang, H.; Tang, Y.; Yu, C. J.; Wang, G.; Yuan, Z.; Quan, H., 11-Mercaptoundecanoic acid capped gold nanoclusters with unusual aggregation-enhanced emission for selective fluorometric hydrogen sulfide determination. *Mikrochim Acta* **2020,** *187* (4), 200.

64. Meng, L.; Yin, J. H.; Yuan, Y.; Xu, N., 11-Mercaptoundecanoic acid capped gold nanoclusters as a fluorescent probe for specific detection of folic acid via a ratiometric fluorescence strategy. *RSC Adv* **2018,** *8* (17), 9327-9333.
65. Dzwonek, M.; Zalubiniak, D.; Piatek, P.; Cichowicz, G.; Meczynska-Wielgosz, S.; Stepkowski, T.; Kruszewski, M.; Wieckowska, A.; Bilewicz, R., Towards potent but less toxic nanopharmaceuticals - lipoic acid bioconjugates of ultrasmall gold nanoparticles with an anticancer drug and addressing unit. *RSC Adv* **2018,** *8* (27), 14947-14957.
66. Turcu, I.; Zarafu, I.; Popa, M.; Chifiriuc, M. C.; Bleotu, C.; Culita, D.; Ghica, C.; Ionita, P., Lipoic Acid Gold Nanoparticles Functionalized with Organic Compounds as Bioactive Materials. *Nanomaterials (Basel)* **2017,** *7* (2).
67. Jimoh, A. A.; Helal, A.; Shaikh, M. N.; Aziz, M. A.; Yamani, Z. H.; Al-Ahmed, A.; Kim, J. P., Schiff Base Ligand Coated Gold Nanoparticles for the Chemical Sensing of Fe(III) Ions. *Journal of Nanomaterials* **2015,** *2015*, 1-7.
68. Amourizi, F.; Dashtian, K.; Ghaedi, M.; Hosseinzadeh, B., An asymmetric Schiff base-functionalized gold nanoparticle-based colorimetric sensor for Hg(2+) ion determination: experimental and DFT studies. *Anal Methods* **2021,** *13* (23), 2603-2611.
69. Peponi, L.; Arrieta, M. P.; Mujica-Garcia, A.; López, D., Smart Polymers. In *Modification of Polymer Properties*, Jasso-Gastinel, C. F., Kenny J. M., Ed. Elsevier Inc: Oxford, United Kingdom, 2017; pp 131-154.
70. Wong, M. W.; Wiberg, K. B.; Frisch, M. J., Solvent effects. 3. Tautomeric equilibria of formamide and 2-pyridone in the gas phase and solution: an ab initio SCRF study. *Journal of the American Chemical Society* **1992,** *114* (5), 1645-1652.
71. Seliger, J.; Zagar, V., Tautomerism and possible polymorphism in solid hydroxypyridines and pyridones studied by 14N NQR. *J Phys Chem A* **2013,** *117* (7), 1651-8.
72. Swain, C. G.; Brown, J. F., Concerted Displacement Reactions. VIII. Polyfunctional Catalysis1. *Journal of the American Chemical Society* **1952,** *74* (10), 2538-2543.
73. Stang, P. J.; Olenyuk, B., Self-Assembly, Symmetry, and Molecular Architecture: Coordination as the Motif in the Rational Design of Supramolecular Metallacyclic Polygons and Polyhedra. *Accounts of Chemical Research* **1997,** *30* (12), 502-518.
74. European Medicine Agency, C. f. H. M. P. *Guideline on the Specification Limits for Residues of Metal Catalysts*; London, 2007.
75. Commission, B. P. *British Pharmacopoeia*; The Stationery Office: Norwich, 2009.
76. Pharmacopoeia, T. S. o. J. *The Japanese Pharmacopoeia*; Tokyo, 2001.
77. United States Pharmacopeial Convention, I. *The United States Pharmacopeia. The National Formulary.*; Rockville, 1979.
78. Saling, P.; Kicherer, A.; Dittrich-Krämer, B.; Wittlinger, R.; Zombik, W.; Schmidt, I.; Schrott, W.; Schmidt, S., Eco-efficiency analysis by basf: the method. *The International Journal of Life Cycle Assessment* **2002,** *7* (4), 203-218.
79. Savage, A. C.; Pikramenou, Z., Peptide coated gold nanoparticles that bind lanthanide ions. *Chem Commun (Camb)* **2011,** *47* (22), 6431-3.
80. Beer, P. D.; Cormode, D. P.; Davis, J. J., Zinc metalloporphyrin-functionalised nanoparticle anion sensors. *Chem Commun (Camb)* **2004,** (4), 414-5.

81. Krpetic, Z.; Guerrini, L.; Larmour, I. A.; Reglinski, J.; Faulds, K.; Graham, D., Importance of nanoparticle size in colorimetric and SERS-based multimodal trace detection of Ni(II) ions with functional gold nanoparticles. *Small* **2012,** *8* (5), 707-14.
82. Abad, J. M.; Mertens, S. F.; Pita, M.; Fernandez, V. M.; Schiffrin, D. J., Functionalization of thioctic acid-capped gold nanoparticles for specific immobilization of histidine-tagged proteins. *J Am Chem Soc* **2005,** *127* (15), 5689-94.
83. Wang, D.-H.; Zhang, Y.; Sun, R.; Zhao, D.-Z., Dimethyl yellow-based colorimetric chemosensors for "naked eye" detection of Cr3+ in aqueous media via test papers. *RSC Advances* **2016,** *6* (6), 4640-4646.
84. Gou, Y.; Zhang, Y.; Qi, J.; Zhou, Z.; Yang, F.; Liang, H., Enhancing the copper(II) complexes cytotoxicity to cancer cells through bound to human serum albumin. *J Inorg Biochem* **2015,** *144*, 47-55.
85. Yu, J.-X.; Kodibagkar, V. D.; Liu, L.; Zhang, Z.; Liu, L.; Magnusson, J.; Liu, Y., 19F-MRS/1H-MRI dual-function probe for detection of β-galactosidase activity. *Chemical Science* **2013,** *4* (5), 2132.
86. Baumgartner, M. R.; Schmalle, H.; Dubler, E., The interaction of transition metals with the coenzyme α-lipoic acid: synthesis, structure and characterization of copper and zinc complexes. *Inorganica Chimica Acta* **1996,** *252* (1-2), 319-331.
87. Sigel, H.; Prijs, B.; McCormick, D. B., Stability and structure of Cd2+ and Pb2+ complexes with biotin, lipoic acid and some of their derivatives in solution. *Journal of Inorganic and Nuclear Chemistry* **1978,** *40* (9), 1678-1680.
88. Brown, P. R.; Edwards, J. O., The reactions of 1, 3-dimercaptopropane, lipoic acid, and dihydrolipoic acid with metal ions. *Journal of Inorganic and Nuclear Chemistry* **1970,** *32* (8), 2671-2675.
89. Flora, S. J. S., Metal Poisoning: Threat and Management. *Al Ameen Journal of Medical Sciences* **2009,** *2*, 4-26.
90. Sears, M. E., Chelation: harnessing and enhancing heavy metal detoxification--a review. *ScientificWorldJournal* **2013,** *2013*, 219840.
91. Huang, X.; Shumski, A. J.; Zhang, X.; Li, C. W., Systematic Control of Redox Properties and Oxygen Reduction Reactivity through Colloidal Ligand-Exchange Deposition of Pd on Au. *J Am Chem Soc* **2018,** *140* (28), 8918-8923.
92. Hakkinen, H., The gold-sulfur interface at the nanoscale. *Nat Chem* **2012,** *4* (6), 443-55.
93. Hostetler, M. J.; Wingate, J. E.; Zhong, C.-J.; Harris, J. E.; Vachet, R. W.; Clark, M. R.; Londono, J. D.; Green, S. J.; Stokes, J. J.; Wignall, G. D.; Glish, G. L.; Porter, M. D.; Evans, N. D.; Murray, R. W., Alkanethiolate Gold Cluster Molecules with Core Diameters from 1.5 to 5.2 nm: Core and Monolayer Properties as a Function of Core Size. *Langmuir* **1998,** *14* (1), 17-30.
94. Sorensen, C. M., Particles as Molecules. **2009**, 37-69.
95. European Medicine Agency, C. f. H. M. P. *ICH Topic Q 2 (R1) Validation of Analytical Procedures: Text and Methodology*; 1995.
96. Hayler, J. D.; Leahy, D. K.; Simmons, E. M., A Pharmaceutical Industry Perspective on Sustainable Metal Catalysis. *Organometallics* **2018,** *38* (1), 36-46.
97. Nuss, P.; Eckelman, M. J., Life cycle assessment of metals: a scientific synthesis. *PLoS One* **2014,** *9* (7), e101298.

98. Tian, Q.; Cheng, Z.; Yajima, H. M.; Savage, S. J.; Green, K. L.; Humphries, T.; Reynolds, M. E.; Babu, S.; Gosselin, F.; Askin, D.; Kurimoto, I.; Hirata, N.; Iwasaki, M.; Shimasaki, Y.; Miki, T., A Practical Synthesis of a PI3K Inhibitor under Noncryogenic Conditions via Functionalization of a Lithium Triarylmagnesiate Intermediate. *Organic Process Research & Development* **2013,** *17* (1), 97-107.
99. Manley, P. W.; Acemoglu, M.; Marterer, W.; Pachinger, W., Large-Scale Negishi Coupling as Applied to the Synthesis of PDE472, an Inhibitor of Phosphodiesterase Type 4D. *Organic Process Research & Development* **2003,** *7* (3), 436-445.

Reprints of publications

A1: Influencing prototropy by metal ion coordination: supramolecular transformation of a dynamer into a Zn-based toroidal species

Journal of
Materials Chemistry C

ROYAL SOCIETY OF CHEMISTRY

COMMUNICATION

Cite this: DOI: 10.1039/d0tc05598k

Received 27th November 2020,
Accepted 13th January 2021

DOI: 10.1039/d0tc05598k

rsc.li/materials-c

Influencing prototropy by metal ion coordination: supramolecular transformation of a dynamer into a Zn-based toroidal species†‡

Miroslava Čonková, [ab] Wojciech Drozdz, [ab] Zygmunt Miłosz, [c] Piotr Cecot, [ab] Jack Harrowfield, [d] Mikołaj Lewandowski [c] and Artur R. Stefankiewicz *[ab]

Disruption of a tautomeric equilibrium by coordination self-assembly depends upon a delicate interplay between supramolecular interactions but has not been studied for supramolecular polymers in two dimensions at the solid–liquid interface. Presented herein is the description of a functionalized molecular module which in DMSO solution generates a highly compact dynamic aggregate in its lactam (amide) form that undergoes reaction with Zn(II) ion to give a ML_2-type complex in which one lactam unit on each ligand has been converted to its iminol form, enabling bidentate binding also involving pyrimidine-N. These solution measurements, as well as a study by scanning tunneling microscopy at the liquid/graphite interface, corroborated by density functional studies, have revealed how the tautomeric equilibrium can be modulated by the addition of a metal salt.

Supramolecular assemblies based on noncovalent bonds are reversible and sensitive to environment, entailing adaptivity and stimuli-responsiveness that can be employed to achieve desired topology and/or functionality.[1–7] Of the numerous stimuli which have been used to displace dynamic equilibria,[8,9] metal ions are amongst the most versatile, since their actual influence can vary greatly, depending upon the particular choice.[10] Very simple, long-known examples of their varying preferences for interaction sites are provided by the complexes of transition metals with ambidentate ligands[11–13] such as thiocyanate and nitrite ions, although more interesting cases arise with the coordination of primary amides, RCONHR′.[14–17] In their neutral form, such amides behave as O-donor species but the enhancement of acidity due to their coordination results in their ready deprotonation followed by rearrangement to the N-bound anion, subsequent reacidification leading, at least in the case of kinetically inert Co(III),[18] to a complex of the tautomeric iminol form of the neutral ligand.

Similar cases of metal ion binding leading to displacement of a tautomeric equilibrium have been seen in uranyl ion complexes of amidoximes, where the ligand is bound in its neutral but zwitterionic form obtained by proton transfer from O to oxime-N.[19,20] Somewhat surprisingly therefore, these principles have not been explored for more complex dynamic aggregates in solution and in two dimensions on a flat surface, even though structurally distinct supramolecular assemblies can be efficiently studied in submolecular detail with scanning probe techniques.[21,22]

In seeking to explore enhancement of metal ion effects on a tautomeric equilibrium, we have examined the coordination behavior of the 2-pyridone-derived ligand H_2L (Fig. 1), where the additional pyrimidine-N coordination sites adjacent to the amide unit were expected to favor action as a bis(bidentate) species with the amide units converted to their iminol form, thus making the bidentate unit a 2,2′-bipyridine derivative. Both theoretical and experimental studies of 2-pyridone itself have shown that its lactam and iminol forms do not differ greatly in energy, so that the position of the equilibrium between them is readily displaced.[23,24] The ligand (H_2L) was prepared in three steps, following a previously reported procedure.[25] The molecule is insoluble in the most commonly used solvents except for dimethyl sulfoxide (DMSO). While it would appear possible that H_2L could adopt a multitude of different forms (for other possible tautomeric forms for ligand H_2L and coordination modes see Fig. S1 and S2 in the ESI†), previous study[25] by ^{1}H NMR spectroscopy of the molecule in DMSO solution and by STM when adsorbed (from 1,2,4-trichlorobenzene) on graphite, has shown only the form presented in Fig. 1 to be involved. Features of the ambient-temperature

[a] Faculty of Chemistry, Adam Mickiewicz University, Uniwersytetu Poznańskiego 8, Poznań 61-614, Poland. E-mail: ars@amu.edu.pl
[b] Center for Advanced Technologies, Adam Mickiewicz University, Uniwersytetu Poznańskiego 10, Poznań 61-614, Poland
[c] NanoBioMedical Centre, Adam Mickiewicz University, Wszechnicy Piastowskiej 3, Poznań 61-614, Poland
[d] Institut de Science et d'Ingénierie Supramoléculaires (ISIS), Université de Strasbourg, 8 allée Gaspard Monge, Strasbourg 67083, France
† Electronic supplementary information (ESI) available. See DOI: 10.1039/d0tc05598k
‡ Dedicated to Prof. Bogdan Marciniec on the occasion of his 80th birthday.

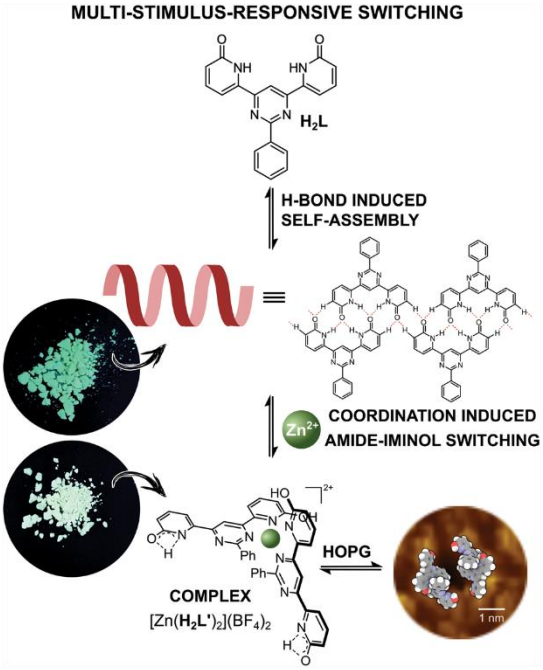

Fig. 1 Schematic representation of the metal-ion coordination induced supramolecular transformation between organic dynamer and Zn-based ML_2 type complex.

^{1}H NMR spectroscopy in DMSO (Fig. 2a), not previously commented on, are that the peaks are all rather broad and that the NH resonance appears at a rather low field (11.5 ppm) indicating its involvement in H-bonding interactions.

Since intramolecular H-bonding is not possible for the conformer shown in Fig. 1, this is taken as evidence that supramolecular aggregation due primarily to N–H O type hydrogen bonding, to some extent analogous to that seen on graphite, must also occur in solution.

In contrast, the ^{1}H NMR spectrum in DMSO-d_6, of the O-methylated analogue of H_2L, which cannot form hydrogen-bonded structures and can exists only in pseudo-iminol form, is markedly different and appears as sharp, well-resolved proton signals expected for the monomeric structures containing two methoxypyridine units (see Fig. S3 in the ESI†). Moreover, MALDI mass spectrometry provided further evidence for the presence of H_2L-based supramolecular H-bonded aggregates (Fig. 3a), while only the monomer signal was observed for the reference O-methylated component (see Fig. S4 in the ESI†).

Interestingly, when, as part of the present work, the DMSO solution was titrated with aqueous HCl to see if protonation might disrupt this aggregation, the spectrum remained essentially unchanged except for the disappearance of the NH signal (Fig. S5, in the ESI†). The lack of evidence of protonation is unsurprising given the weak basicity of both pyrimidine and amide units but the loss of the NH peak could be explained as a result of an acid-catalyzed exchange process passing through the iminol (hydroxypyridine) tautomer of H_2L as an intermediate (Fig. S6 in the ESI†), thus being evidence that this form should be attainable and justifying efforts to explore the effects of metal ion coordination.

While it is known that different metal ions can favour binding of either tautomer of an amide ligand,[17,26] Zn(II), in particular has been shown to favour the iminol form.

The diamagnetic nature of Zn(II) renders ^{1}H NMR spectroscopy a particularly convenient way of following its complex formation. Addition of $Zn(BF_4)_2$ to a solution of H_2L in DMSO-d_6 produced no immediate change in the ^{1}H NMR spectrum but on prolonged reaction (48 hours) at a high temperature, peaks, in particular two broad resonances at d 11.3 and 11.8, attributable to a new species became evident (Fig. S7 in the ESI†). Assuming that the slowness of the reaction was due to the limited ability of the neutral, amide-form ligand to compete with DMSO for coordination to Zn(II), an alternative means of bringing the two species into contact was sought.

The NH acidity of primary amides is well-known, the pK_a of 2-pyridone itself in DMSO being 17,[27] and an anionic ligand should of course interact more strongly with a cation than it would with its neutral parent. Even more significantly, there is an extensive known coordination chemistry of amide-derived anions which shows that the form of their complexes is usually closer to what would be expected for an iminolate than an amidate.[27,28] Reaction of H_2L with 2 molar equivalents of NaOH in DMSO-d_6 provided a deep yellow solution giving a

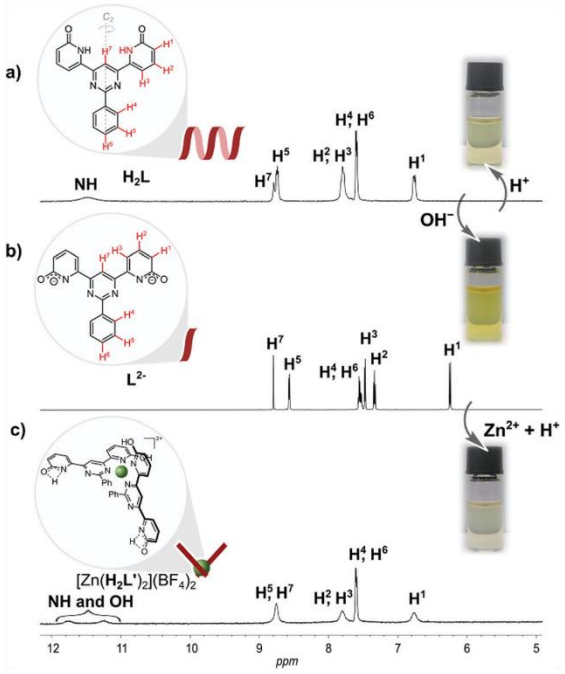

Fig. 2 ^{1}H NMR (600 MHz) spectra at ambient temperature of: (a) fully organic dynamer H_2L; (b) L^{2-} in form of disodium salt; (c) $[Zn(H_2L^0)_2](BF_4)_2$ in DMSO-d_6.

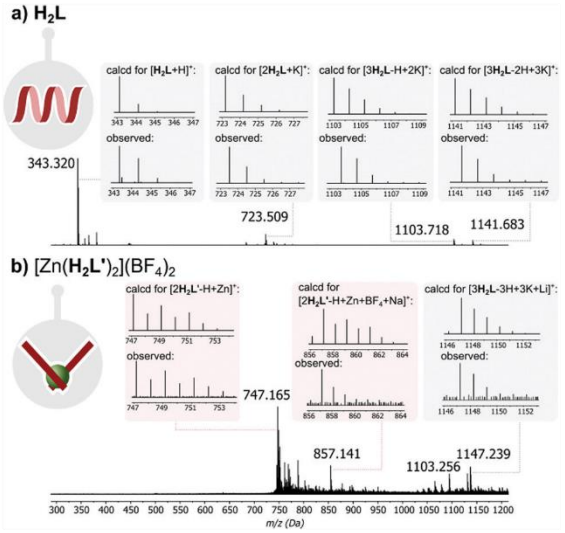

Fig. 3 Simulated and experimental MALDI-MS signals of: (a) H_2L and (b) complex $[Zn(H_2L^0)_2](BF_4)_2$.

^{1}H NMR spectrum with very well resolved peaks consistent with the formation of the presumably largely dissociated disodium complex (Fig. 2b). Addition of 0.5 molar equivalent of $Zn(BF_4)_2$ to this solution resulted in drastic broadening of all peaks, indicating rather strong interaction, and careful addition of 2 molar equivalents of HCl then led to the emergence of two broad resonances as seen in the first experiment (Fig. 2c). Assignment of one of these resonances as due to the NH of the uncoordinated amide unit and the other as OH of the bound iminol unit is completely consistent with the structure shown in Fig. 2, although we have not been able to establish which is which.

Repetition of the second experiment on a preparative scale and addition of methanol and diethyl ether to the final solution led to the isolation of $[Zn(H_2L^0)_2](BF_4)_2$ in the form of yellow powder.

Since a 2,2^0-bipyridine-like ligand should be weakly basic and Zn(II) complexes are generally labile, we reasoned that release of the ligand from $[Zn(H_2L^0)_2](BF_4)_2$ should occur on further addition of acid. Consistent with this expectation, an ^{1}H NMR titration of $[Zn(H_2L^0)_2](BF_4)_2$ with acid (0.06 M HCl, in H_2O/DMSO-d_6) revealed, after addition of 1 equivalent, that the spectrum of dynamer H_2L was regenerated (see ESI,† Fig. S13). Since chloride ion is poorly solvated in DMSO, formation of chloro complexes may have assisted this reaction also.

Since in DMSO solution, $[Zn(H_2L^0)_2](BF_4)_2$ has a rather dynamic nature, we decided to examine fluorescence of both H_2L and $[Zn(H_2L^0)_2](BF_4)_2$ in solid state. These measurements show that described system is photo-responsive, which opens several avenues towards their application in various technological fields. As shown in Fig. 4, after excitation at 468 nm, the emission spectrum of H_2L shows a broad band with its maximum at 555 nm, while in the emission spectrum of $[Zn(H_2L^0)_2](BF_4)_2$ there

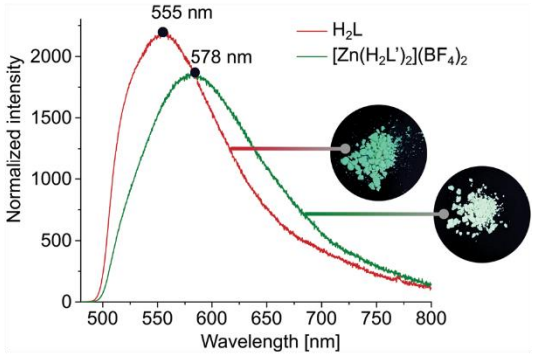

Fig. 4 Emission spectra of H_2L and $[Zn(H_2L^0)_2](BF_4)_2$ in the solid state, together with photographs made under UV light (254 nm).

is a notable shift in the band maximum =578 nm (for absorbance spectra see ESI,† Fig. S12).

The difference in fluorescence under excitation at 254 nm is also visible to the naked eye as a slight difference in colour (Fig. 4). The observed significant Stokes shifts of 87 nm (H_2L) and 110 nm ($[Zn(H_2L^0)_2](BF_4)_2$) predispose both materials to application as dynamic fluorescence dyes.

Due to the limited solubility of both H_2L and $[Zn(H_2L^0)_2](BF_4)_2$, we were not able to obtain a crystal suitable for an X-ray diffraction measurement, even after multiple trials. However, computational methods are a powerful tool for compound characterization. Therefore the B3LYP/6-31+G(d,p) molecular geometry optimization of H_2L together with H_2L^0 and $[Zn(H_2L^0)_2](BF_4)_2$ was performed. Additionally, in order to capture the effects of dispersion interactions, the empirical Grimme GD3 dispersion parameters were used, supplemented by Becke–Johnson (BJ) damping. The accuracy of the method was tested by first optimizing H_2L, until results from the literature[25] were reproduced (Table S3 in the ESI†). $Zn(H_2L^0)_2^{2+}$ was optimized stepwise using the same method. First H_2L^0 was optimized and based on these results, the structure of the cation $Zn(H_2L^0)_2^{2+}$ was obtained. Ligand molecules coordinate the Zn^{2+} cation in their pyrimidine–pyridine pocket, the Zn center having the symmetry of a distorted tetrahedron with angles N(pyr)–Zn–N(pyr) 1531, N(py)–Zn–N(py) 1051 and N(pyr)–Zn–N(py) 81.51 and Zn–N(py) and Zn–N(pyr) bond lengths of 2.08 Å and 2.01 Å, respectively (see ESI,† Section II for details).

Intrinsic properties of a molecule can be predicted from the energy levels of the HOMO and LUMO orbitals. The calculations showed a symmetrical pattern for the H_2L MO, while the introduction of a metal ion caused a shift of the electron density in the HOMO towards the metal centre and a displacement of the LUMO to the outer region of the ligand (Table S2 in the ESI†). It has been previously shown, that H_2L forms both 2D arrays and helical polymer chains at a solid–liquid interface.[25] Fig. 5a presents the STM image of a helical dynamer H_2L drop-casted onto HOPG, heated up and imaged at room temperature. The measured period of the model structure is B 25 nm – in agreement with the experimental value. In addition to helical structures, we also observed 2D molecular arrays shown in Fig. 5d,

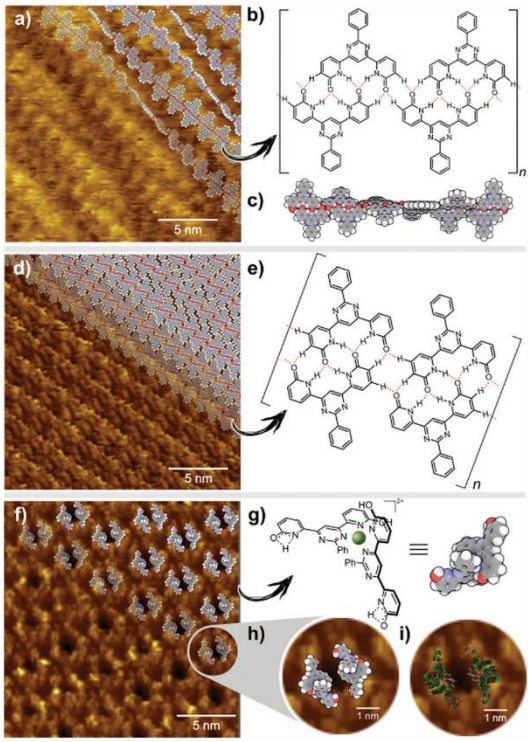

Fig. 5 (a) STM image of a helical dynamer with model arranged on top of it. Image size: 20 20 nm^2; V_{sample} = +0.6 V; I_T = 0.1 nA; (b) chemical structure of H_2L with presented H-bond motif; (c) model of helical dynamer H_2L; (d) STM image of a 2D array of dynamer with model an arranged on top of it. Image size: 20 20 nm^2; V_{sample} = +0.6 V; I_T = 0.1 nA; (e) chemical structure of H_2L with presented H-bond motif; (f) STM image of 2D an array formed by complex $[Zn(H_2L^0)_2](BF_4)_2$ with a model arranged on top of it. Image size: 20 20 nm^2; V_{sample} = +0.6 V; I_T = 0.1 nA; (g) chemical structure of the cation $Zn(H_2L^0)_2^{2+}$ and its model; (h) zoomed area of STM image shown in (f). Image size: 5 5 nm^2; V_{sample} = +0.6 V; I_T = 0.1 nA; (i) zoomed area of STM image with model of LUMO orbitals on top of it. Image size: 5 5 nm^2; V_{sample} = +0.6 V; I_T = 0.1 nA.

which are built from the same molecule H_2L but with a different H-bonding motif (Fig. 5e). Following similar drop-casting of a solution of complex $[Zn(H_2L^0)_2](BF_4)_2$, the STM image revealed a well-ordered molecular array, visible as a 2D array of dark spots surrounded by bright rings (Fig. 5f). The measured in-plane lattice parameters of this structure are B 3.6 nm. STM topography fits very well with the calculated LUMO orbitals of $Zn(H_2L^0)_2^{2+}$ (Fig. 5i). The two pyridone moieties not involved in coordination should still be able to form H-bonds, regardless of their tautomeric form. This we consider to be the reason why two molecules of the complex assemble into toroidal dimer units (Fig. 5), which then form more extended arrays.

The present work provides a previously unknown example of the desymmetrisation of a ligand resulting from the metal-ion-induced tautomerisation of one binding site within an initially symmetrical organic species. This mode of coordination produces two different H-bonding sites within the metallosupramolecular species, which are both used to provide different forms of association in the solid state and in solution. Retention of the amide form of the unbound coordination site is significant factor in leading to the H-bonding which appears to control the adsorbed form of the complex on the surface and which reveals its multifunctionality. Reversible interconversion between organic dynamer and metallosupramolecular toroidal species is readily achieved by simple control of metal ion concentration, base and acid additions and results in the generation of dynamic materials of distinct fluorescent properties. Thus, we have demonstrated that simple 2-pyridone derivatives are well suited for the generation of distinct forms of fluorescent adaptive materials.

Conflicts of interest

There are no conflicts to declare.

Acknowledgements

This work was funded by the National Science Centre of Poland grants: SONATA BIS 2018/30/E/ST5/00032 (A.R.S.), PRELUDIUM UMO-2016/21/N/ST5/00849 (W. D.) and OPUS 2014/15/B/ST3/02927 (Z. M. and M. L.). The work of P. C. was also co-financed by European Social Fund under the Operational Program Knowledge Education Development and Poznan Supercomputing and Networking Centre computing grant no. 401. The work of M. C. was co-financed by the National Centre for Research and Development grant POWR.03.02.00-00-I032/16. We thank Prof. Jean-Marie Lehn, Dr Monika Wałęsa-Chorab and Jakub Lewandowski for their contribution at the initial stage of this project.

Notes and references

1 J.-F. Lutz, J.-M. Lehn, E. W. Meijer and K. Matyjaszewski, Nat. Rev. Mater., 2016, 16024.
2 S. Chen, R. Costil, F. K. Leung and B. L. Feringa, Angew. Chem., Int. Ed., 2021, DOI: 10.1002/anie.202007693.
3 A. Goulet-Hanssens, F. Eisenreich and S. Hecht, Adv. Mater., 2020, 32, e1905966.
4 A. Brzechwa-Chodzyńska, M. Zieliński, M. Gilski, J. M. Harrowfield and A. R. Stefankiewicz, Inorg. Chem., 2020, 59, 8552–8561.
5 A. Bocian, W. Drożdż, M. Szymańska, J. Lewandowski, M. Fik-Jaskółka, A. Gorczyński, V. Patroniak and A. R. Stefankiewicz, Nanoscale, 2020, 12, 4743–4750.
6 G. Markiewicz, M. M. J. Smulders and A. R. Stefankiewicz, Adv. Sci., 2019, 6, 1900577.
7 W. Drożdż, A. Walczak, Y. Bessin, V. Gervais, X.-Y. Cao, J.-M. Lehn, S. Ulrich and A. R. Stefankiewicz, Chem. – Eur. J., 2018, 24, 10802–10811.
8 J. M. Lehn, Chem. Soc. Rev., 2007, 36, 151–160.
9 S. Sobczak, W. Drożdż, G. I. Lampronti, A. M. Belenguer, A. Katrusiak and A. R. Stefankiewicz, Chem. – Eur. J., 2018, 24, 8769–8773.
10 A. J. McConnell, C. S. Wood, P. P. Neelakandan and J. R. Nitschke, Chem. Rev., 2015, 115, 7729–7793.

11 R. A. A. Abdine, G. Kurpik, A. Walczak, S. A. A. Aeash, A. R. Stefankiewicz, F. Monnier and M. Taillefer, J. Catal., 2019, 376, 119–122.
12 A. Walczak and A. R. Stefankiewicz, Inorg. Chem., 2018, 57, 471–477.
13 A. Walczak, H. Stachowiak, G. Kurpik, J. Kaźmierczak, G. Hreczycho and A. R. Stefankiewicz, J. Catal., 2019, 373, 139–146.
14 R. C. R. H. E. Toma, Croat. Chem. Acta, 2001, 499–528.
15 W. G. Jackson and A. M. Sargeson, Essay 11 in Rearrangements in Ground and Excited States, in Organic Chemistry: A Series of Monographs, ed. P. de Mayo, Academic Press, New York, 1980, vol. 42-3, pp. 273–378.
16 D. B. Brown, M. B. Robin and R. D. Burbank, J. Am. Chem. Soc., 1968, 90, 5621–5622.
17 D. P. Fairlie, T. C. Woon, W. A. Wickramasinghe and A. C. Willis, Inorg. Chem., 1994, 33, 6425–6428.
18 D. P. Fairlie, P. M. Angus, M. D. Fenn and W. G. Jackson, Inorg. Chem., 1991, 30, 1564–1569.
19 D. A. Decato and O. B. Berryman, Org. Chem. Front., 2019, 6, 1038–1043.
20 E. G. Witte, K. S. Schwochau, G. Henkel and B. Krebs, Inorg. Chim. Acta, 1984, 94, 323–331.
21 D. B. Amabilino and P. A. Gale, Chem. Soc. Rev., 2017, 46, 2376–2377.
22 T. Kudernac, S. Lei, J. A. Elemans and S. De Feyter, Chem. Soc. Rev., 2009, 38, 402–421.
23 M. W. Wong, K. B. Wiberg and M. J. Frisch, J. Am. Chem. Soc., 1992, 114, 1645–1652.
24 J. Seliger and V. Zagar, J. Phys. Chem. A, 2013, 117, 1651–1658.
25 A. Ciesielski, A. R. Stefankiewicz, F. Hanke, M. Persson, J.-M. Lehn and P. Samorì, Small, 2011, 7, 342–350.
26 Z. Xu, K. H. Baek, H. N. Kim, J. Cui, X. Qian, D. R. Spring, I. Shin and J. Yoon, J. Am. Chem. Soc., 2010, 132, 601–610.
27 C. G. Swain and J. F. Brown, J. Am. Chem. Soc., 1952, 74, 2538–2543.
28 P. J. Stang and B. Olenyuk, Acc. Chem. Res., 1997, 30, 502–518.

Supplementary information to A1

Electronic Supplementary Material (ESI) for Journal of Materials Chemistry C.

Electronic Supplementary Information

Influencing Prototropy by Metal Ion Coordination: Supramolecular Transformation of a Dynamer into a Zn-based Toroidal Species

Miroslava Čonková[a,b], Wojciech Drożdż[a,b], Zygmunt Miłosz[c], Piotr Cecot[a,b], Jack Harrowfield[d], Mikołaj Lewandowski[c], Artur R. Stefankiewcz[a,b]*

[a]Faculty of Chemistry
Adam Mickiewicz University
Uniwersytetu Poznańskiego 8, 61-614 Poznań, Poland

[b]Center for Advanced Technologies
Adam Mickiewicz University
Uniwersytetu Poznańskiego 10, 61-614 Poznań

[c]NanoBioMedical Centre
Adam Mickiewicz University
Wszechnicy Piastowskiej 3, 61-614 Poznań, Poland

[d]Institut de Science et d'Ingénierie Supramoléculaires (ISIS)
Université de Strasbourg
8 allée Gaspard Monge, 67083 Strasbourg, France

*Corresponding author. E-mail: ars@amu.edu.pl (Artur R. Stefankiewcz)

Table of contents

I. EXPERIMENTAL SECTION

General methods

Chemicals were purchased from commercial suppliers (Sigma-Aldrich and TriMen Chemicals) and used as received. NMR spectroscopic data were performed on a Bruker UltraShield 300 MHz and 600 MHz spectrometers, calibrated against the residual protonated solvent signal (for ^{1}H NMR DMSO-d_6: δ = 2.50, for ^{13}C NMR DMSO-d_6: δ = 39.52) and are given in ppm. Mass spectra were determined using MALDI-TOF/TOF (Ultrafle extreme, Bruker) spectrometer in DMSO/MeOH mixture. Experiments were performed on DHB (**H_2L**, **Me_2L**) and THAP [Zn(**H_2L'**)$_2$]$(BF_4)_2$ matrix. DSC, TGA and DTG experiments were performed on Simultaneous Thermal Analyzer (STA) 6000, Perkin Elmer. UV/Vis measurements were conducted in solid state on Jasco V-770 spectrophotometer. Fluorescence spectra were made in solid state on Fluorescence Spectrophotometer Hitachi F-7000; light source – 150 W xenon lamp; wavelenght speed 240 nm/min. Photographs were made under UV lamp at 254 nm wavelenght on digital camera in Samsung S10. Infrared spectra were measured in ATR mode on FT-IR (Nicoletis 50). Both, ligand in amido (**H_2L**) and iminol (**H_2L'**) form were optimized using DFT b3lyp functional and 6-31+G(d,p) basis set. All calculations were carried out using Gaussian 16 rev C.01 software. Steric hindrance of complex [Zn(**H_2L'**)$_2$]$(BF_4)_2$ was calculated via SambVca 2.1 A web application (https://www.molnac.unisa.it/OMtools/sambvca2.1/index.html). The STM measurements were performed using a Bruker Innova Atomic Force Microscope operating in a constant-current STM mode. All the images were recorded using mechanically-cut PtIr tips. Highly-oriented pyrolytic graphite (HOPG) substrate was cleaned using a "Scotch tape" method before each experiment. The use of HOPG was justified by its weak interaction with any adsorbed species which was favouring the formation of molecule-molecule bonds rather than molecule-substrate. The acquired STM images were processed using Gwyddion (gwyddion.net) computer software.

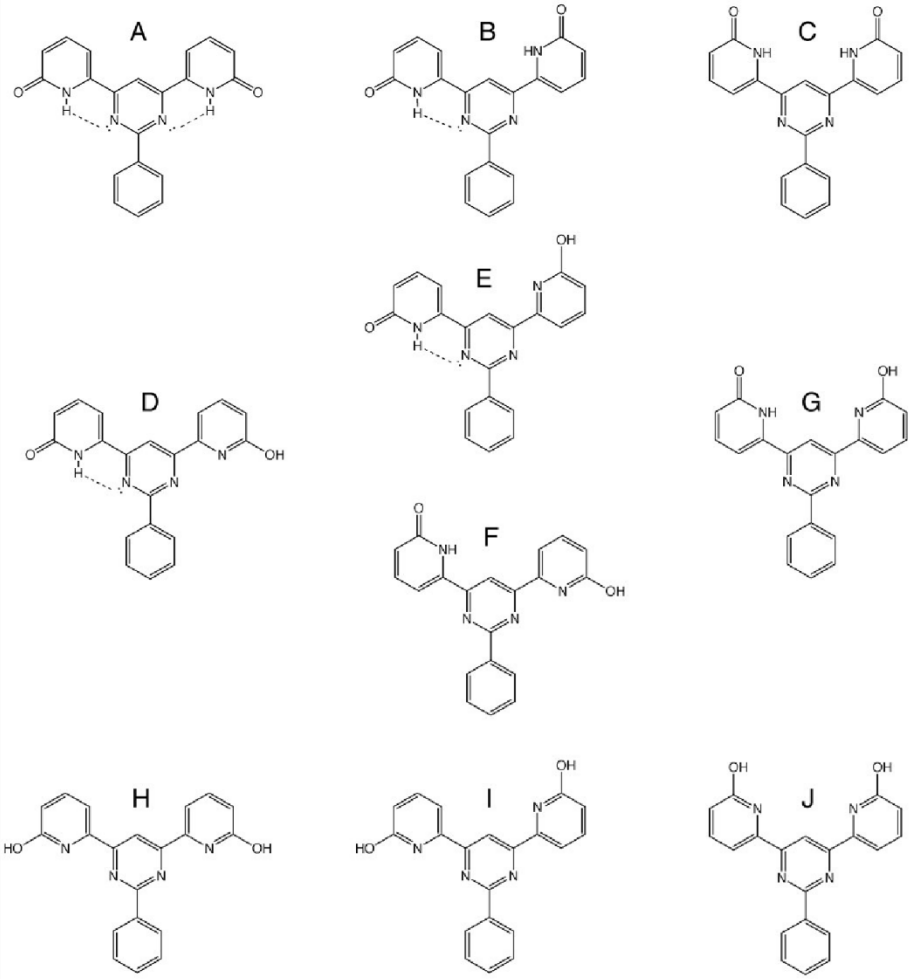

Figure S1. Representations of planar conformations and their tautomeric forms for ligand **H_2L**. Possible intramolecular H-bonds in certain species are shown as dashed lines. (Nonplanar conformations are also not to be excluded.)

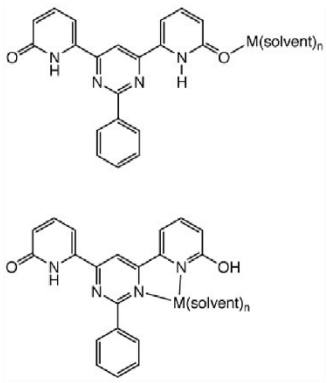

Figure S2. Different possible coordination modes for tautomeric units of ligand **H_2L**.

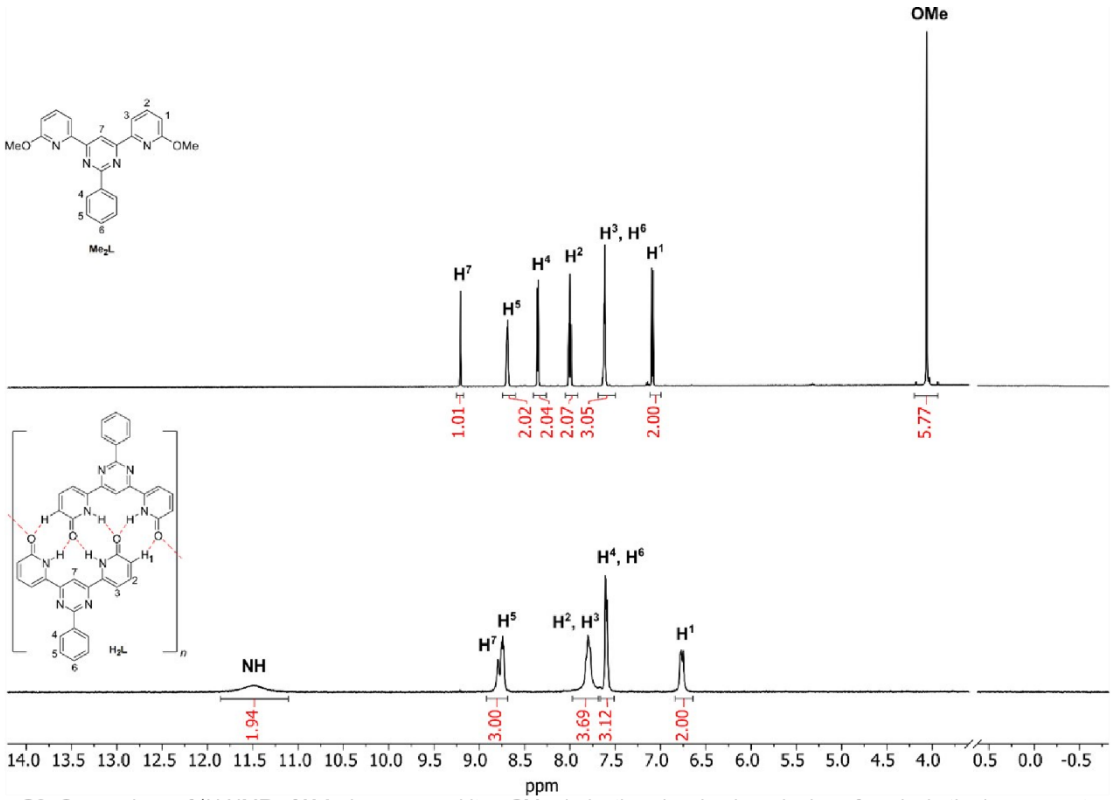

Figure S3. Comparison of ^{1}H NMR of **H_2L** dynamer and its –OMe derivative showing broadening of peaks in the lower spectrum, that suggests H-bonds.

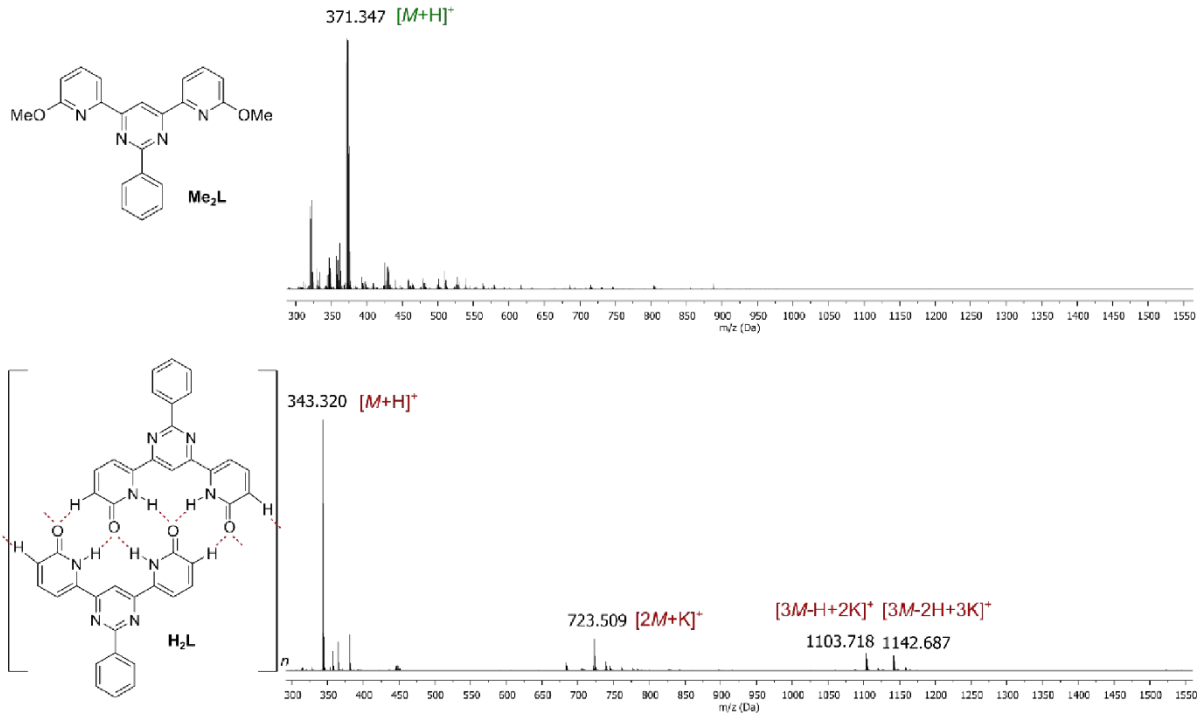

Figure S4. Comparison of MALDI spectra of **H_2L** and its –OMe derivative.

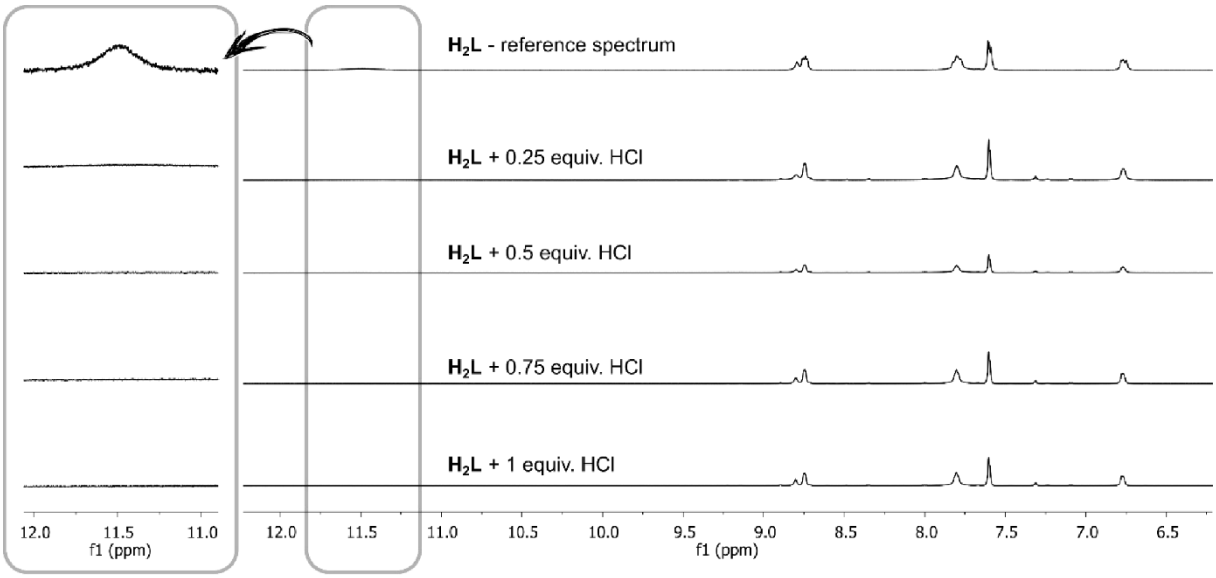

Figure S5. Titration of **H_2L** with HCl (0.06 M, in DMSO-d_6).

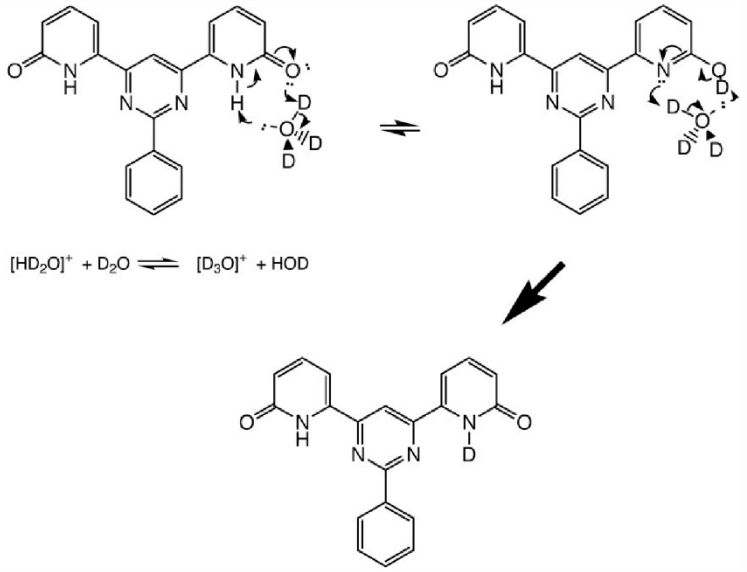

Figure S6. A possible mechanism for acid-catalysed NH exchange in form C of **H_2L**.

Synthesis of complex $[Zn(\mathbf{H_2L'})_2](BF_4)_2$:

Method A: To the suspension of ligand **H_2L** (50 mg, 0.15 mmol) in DMSO (10 mL) $Zn(BF_4)_2$ (39 mg, 0.15 mmol) was added and the suspension was stirred at 130 °C for 48 h. After the clear solution was cooled to room temperature, methanol and then big portion of diethyl ether was added to precipitate the product. Yellow solid was centrifuged, washed several times with diethyl ether and dried under vacuum.

Method B: To the suspension of ligand **H_2L** (50 mg, 0.15 mmol) in DMSO (10 mL) NaOH (12 mg, 0.3 mmol) solution in water (1 mL) was added. After stirring at ambient temperature for 0.5 hour $Zn(BF_4)_2$ (39 mg, 0.15 mmol) was added and the mixture was stirred at ambient temperature for 24 h. After methanol and big portion of diethyl ether was added to precipitate the product. Yellow solid was centrifuged, washed several times with diethyl ether and dried under vacuum.

^{1}H NMR (600 MHz, DMSO-d_6) δ 11.76 (bs, 1H), 11.25 (bs, 1H), 8.91–8.60 (m, 3H), 7.91–7.71 (m, 4H), 7.64–7.57 (m, 3H), 6.88–6.63 (m, 2H). ESI-TOF-MS: for $[C_{40}H_{27}N_8O_4Zn]^+$ calc. m/z = 747.1441, found 747.1419.

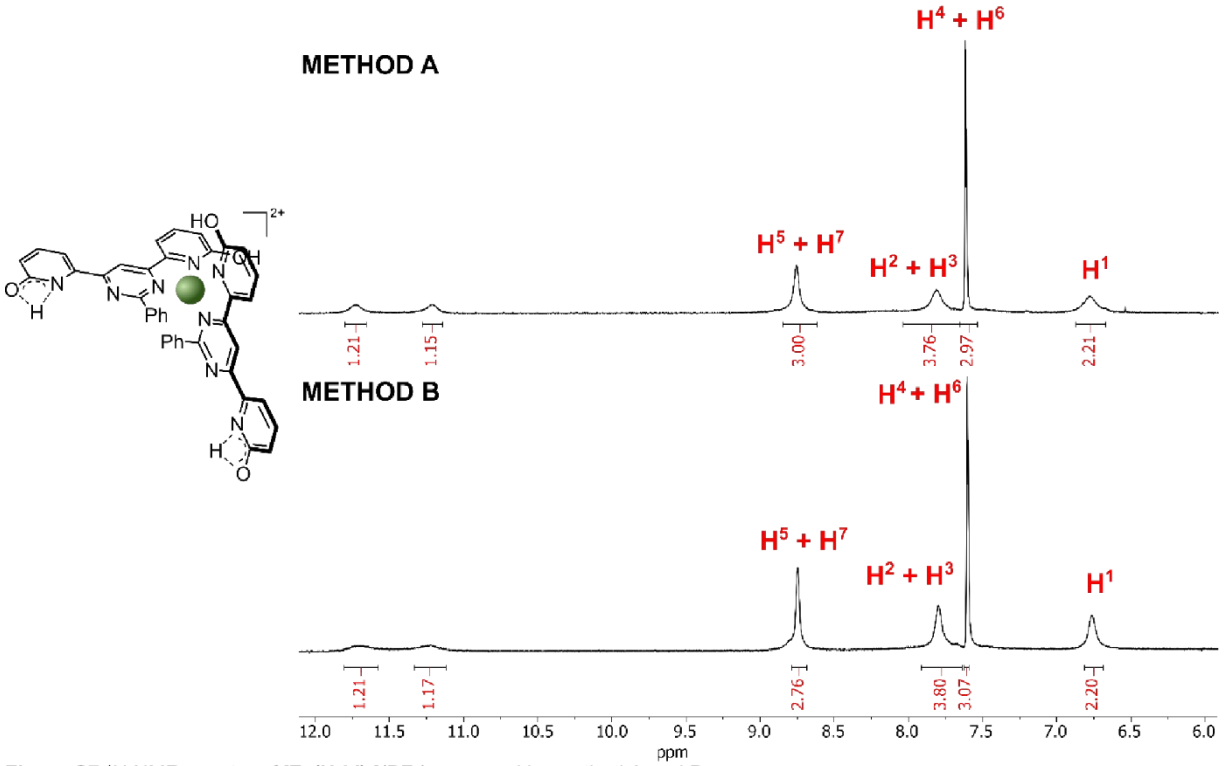

Figure S7 ^{1}H NMR spectra of $[Zn(\mathbf{H_2L'})_2](BF_4)_2$ prepared by method A and B.

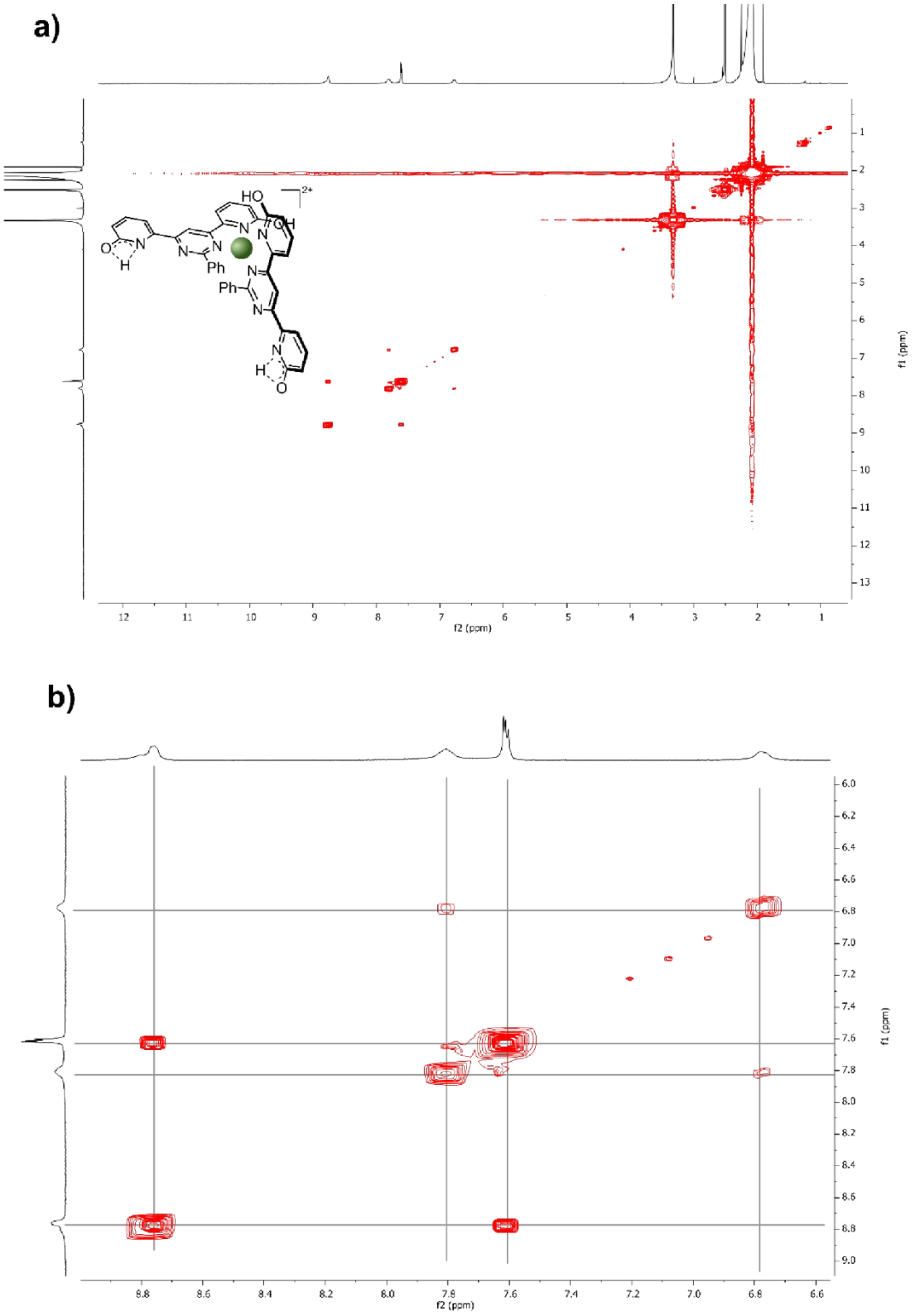

Figure S8. ^{1}H-^{1}H COSY NMR spectrum of $[Zn(\mathbf{H_2L'})_2](BF_4)_2$ (a – whole spectrum, b – part of the spectrum)

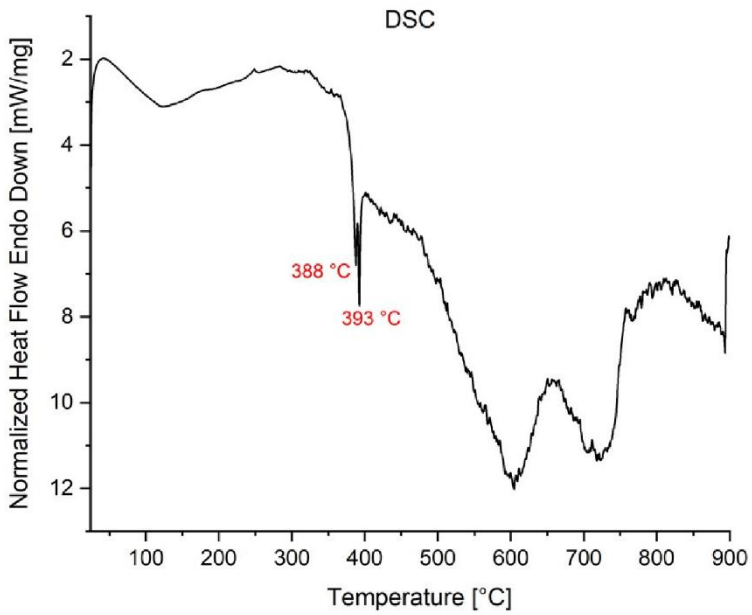

Figure S9. Differential scanning calorimetry analysis of complex $[Zn(\mathbf{H_2L'})_2](BF_4)_2$

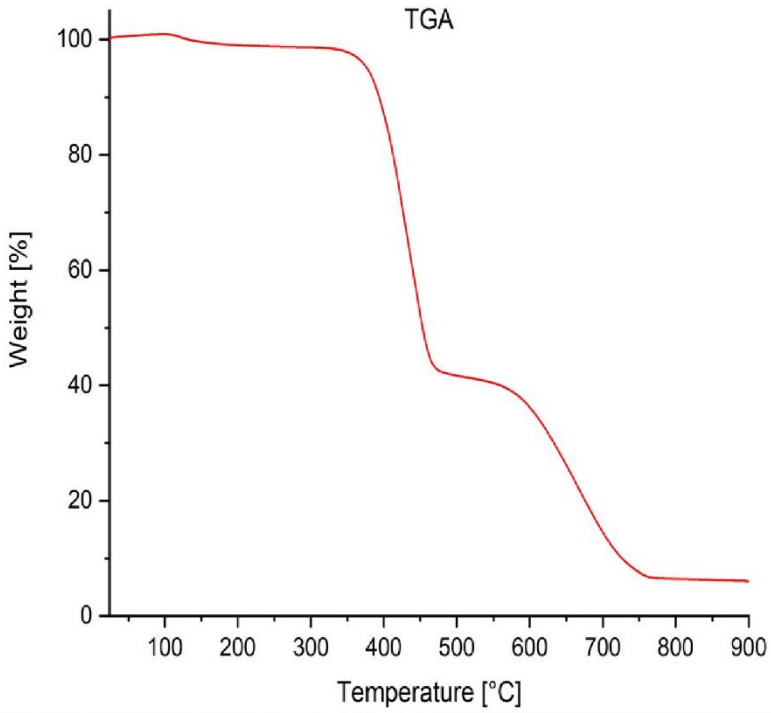

Figure S10. Thermogravimetric analysis of complex $[Zn(\mathbf{H_2L'})_2](BF_4)_2$

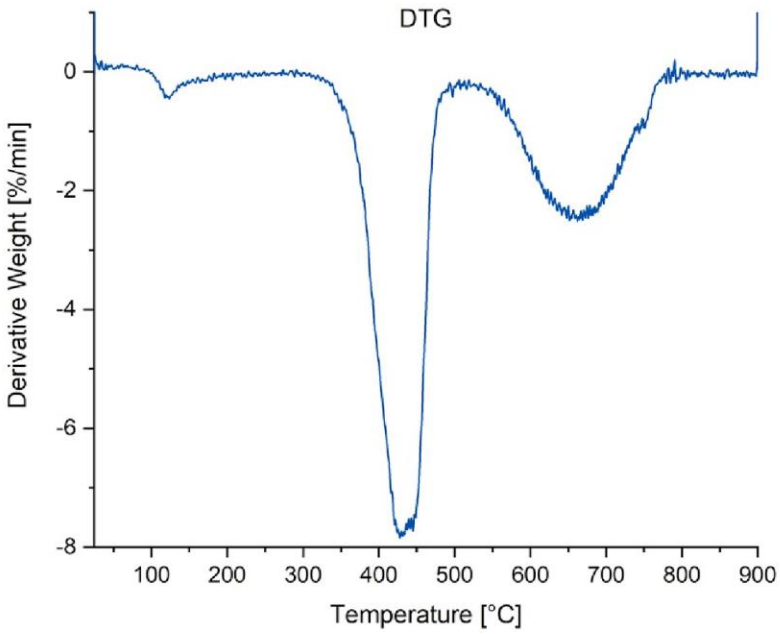

Figure S11. Difference thermogravimetric analysis of complex $[Zn(\mathbf{H_2L'})_2](BF_4)_2$

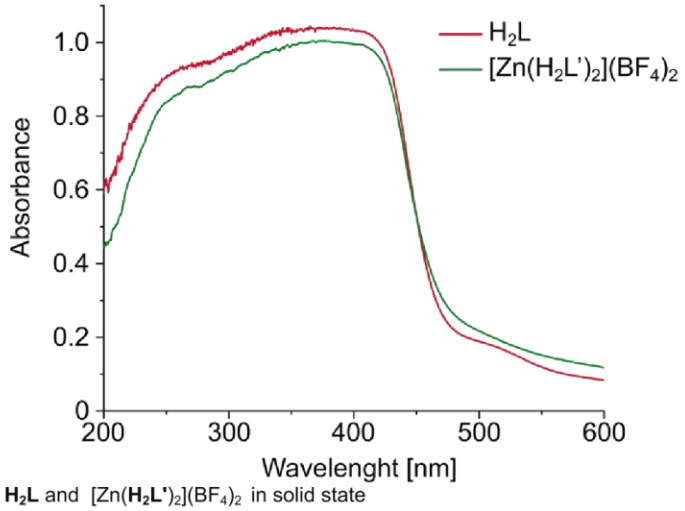

Figure S12. UV-Vis spectra of $\mathbf{H_2L}$ and $[Zn(\mathbf{H_2L'})_2](BF_4)_2$ in solid state

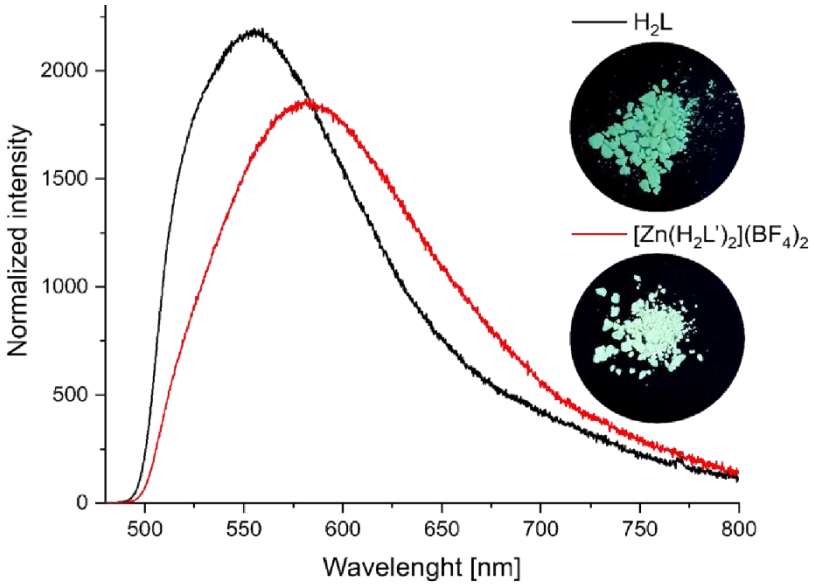

Figure S13. Fluorescence spectra of **H_2L** and $[Zn(\mathbf{H_2L'})_2](BF_4)_2$ in solid state and photographs under UV lamp (254 nm)

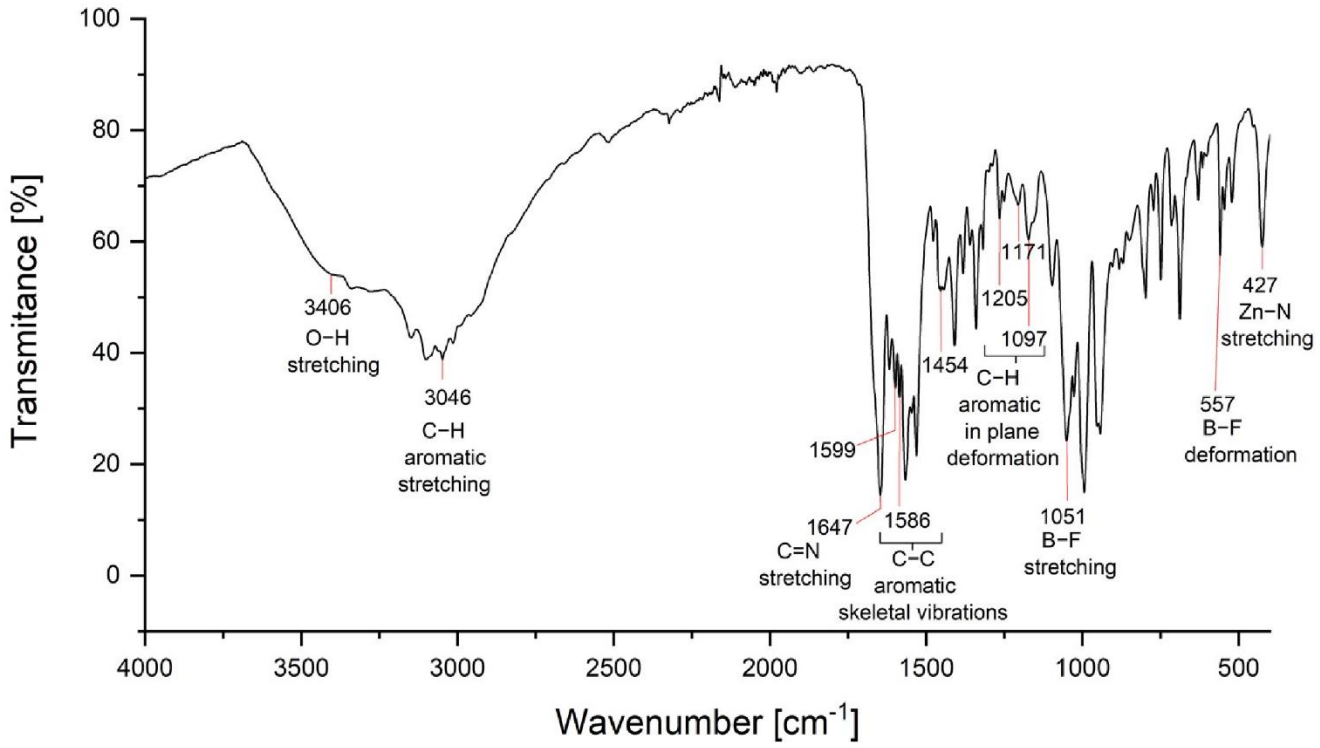

Figure S14. ATR-IR spectrum of complex $[Zn(\mathbf{H_2L'})_2](BF_4)_2$

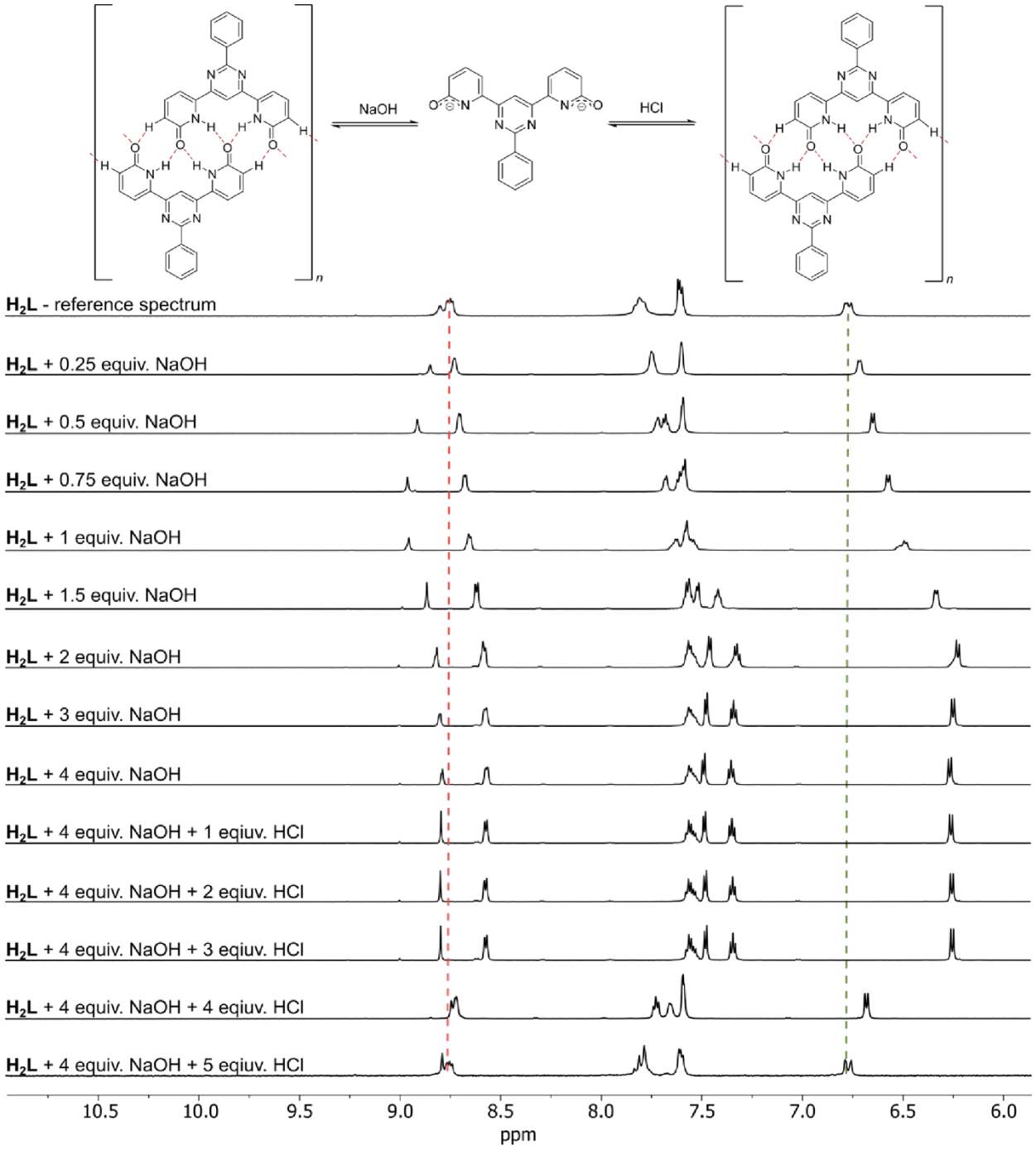

Figure S15. Titration of **H_2L** with NaOH (0.12 M in DMSO-d_6/D_2O = 1:1) causing **L^{2-}** formation, followed by incremental addition of HCl 0.06 M, in DMSO-d_6. NMR spectra were measured right after the addition. Excess of both NaOH and HCl were used to speed up the transformations.

.

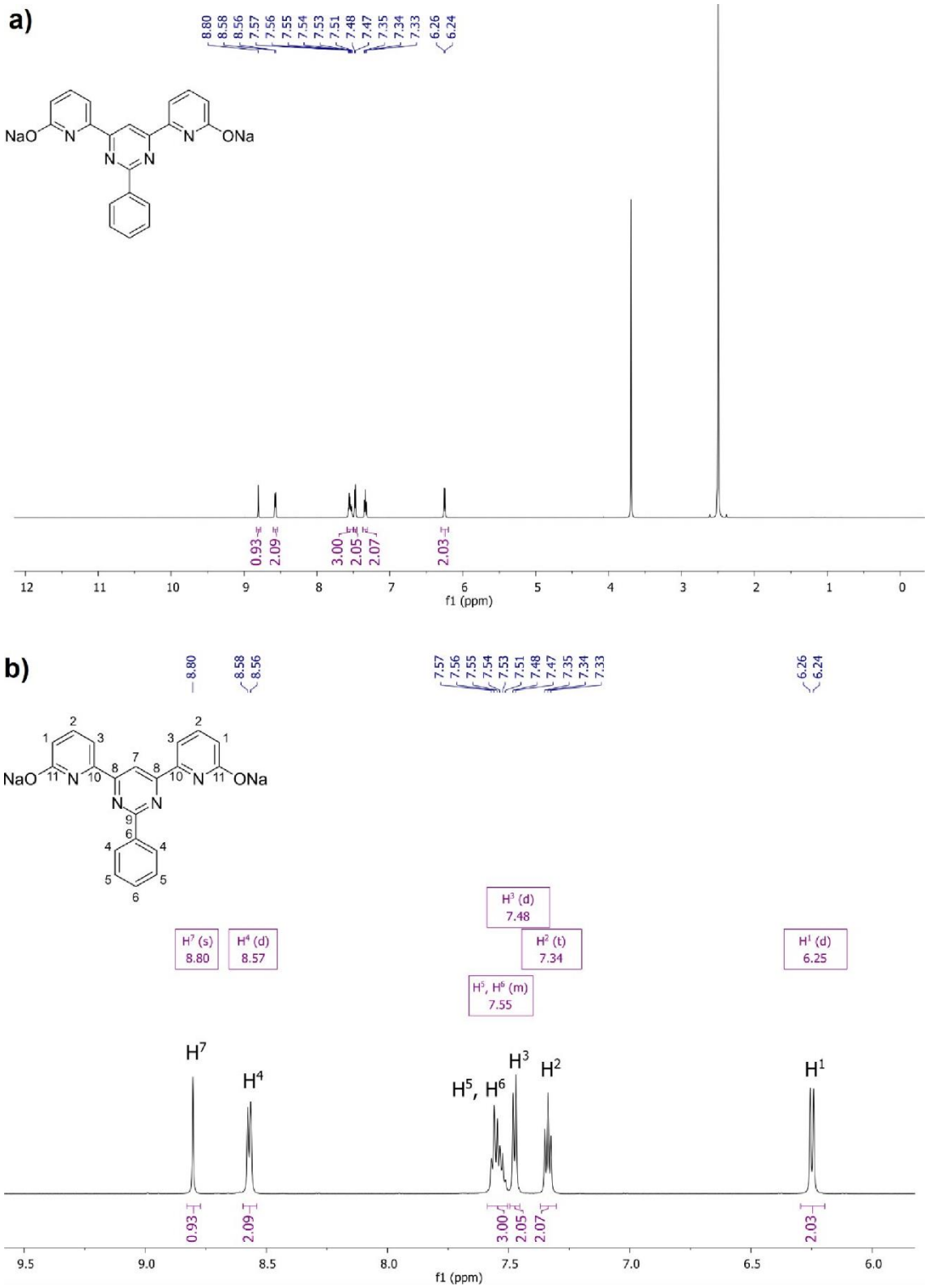

Figure S16. ^{1}H NMR spectrum of $\mathbf{L^{2-}}$ monomer (a – whole spectrum, b – part of the spectrum)

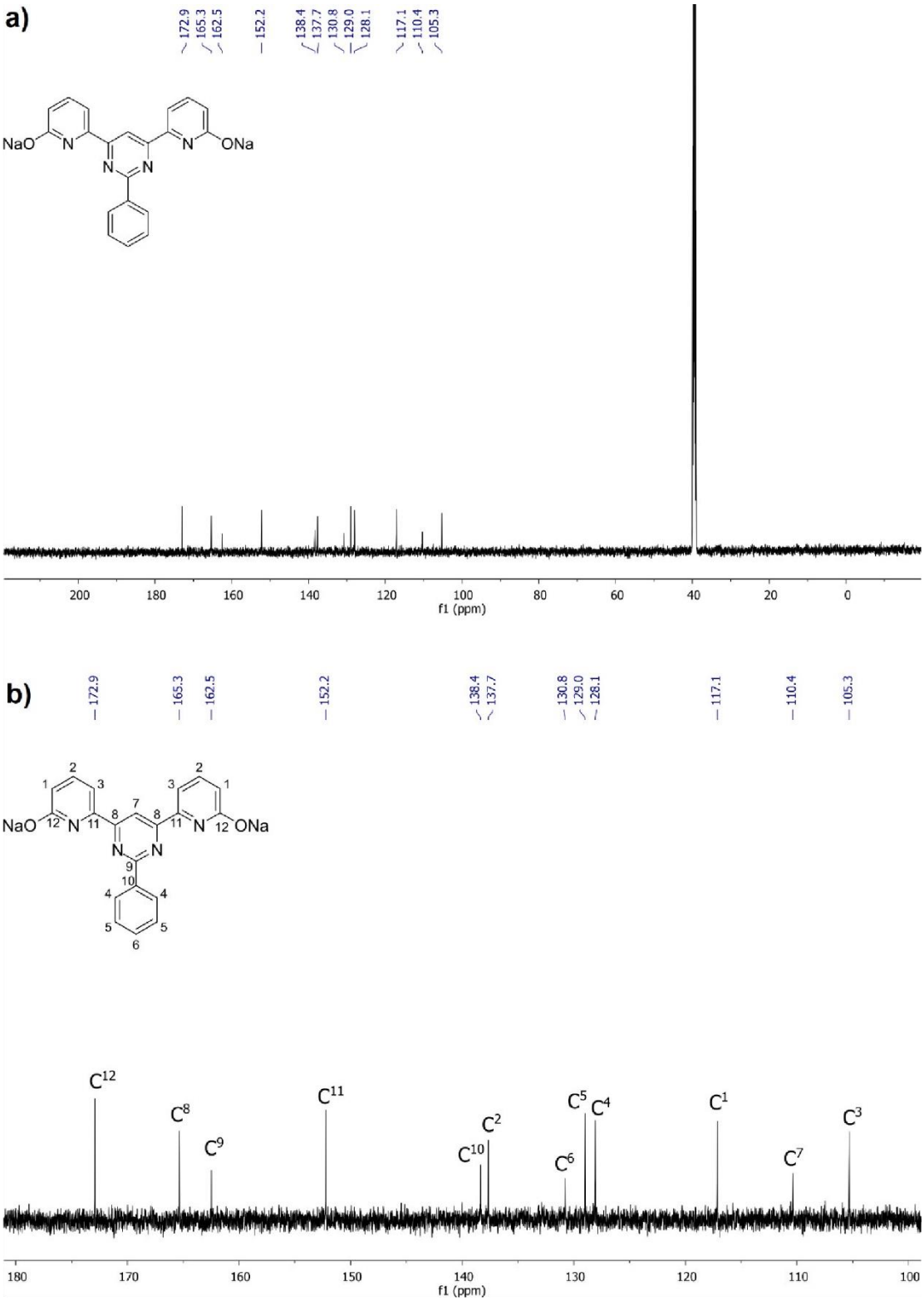

Figure S17. ^{13}C NMR spectrum of L^{2-} monomer (a – whole spectrum, b – part of the spectrum)

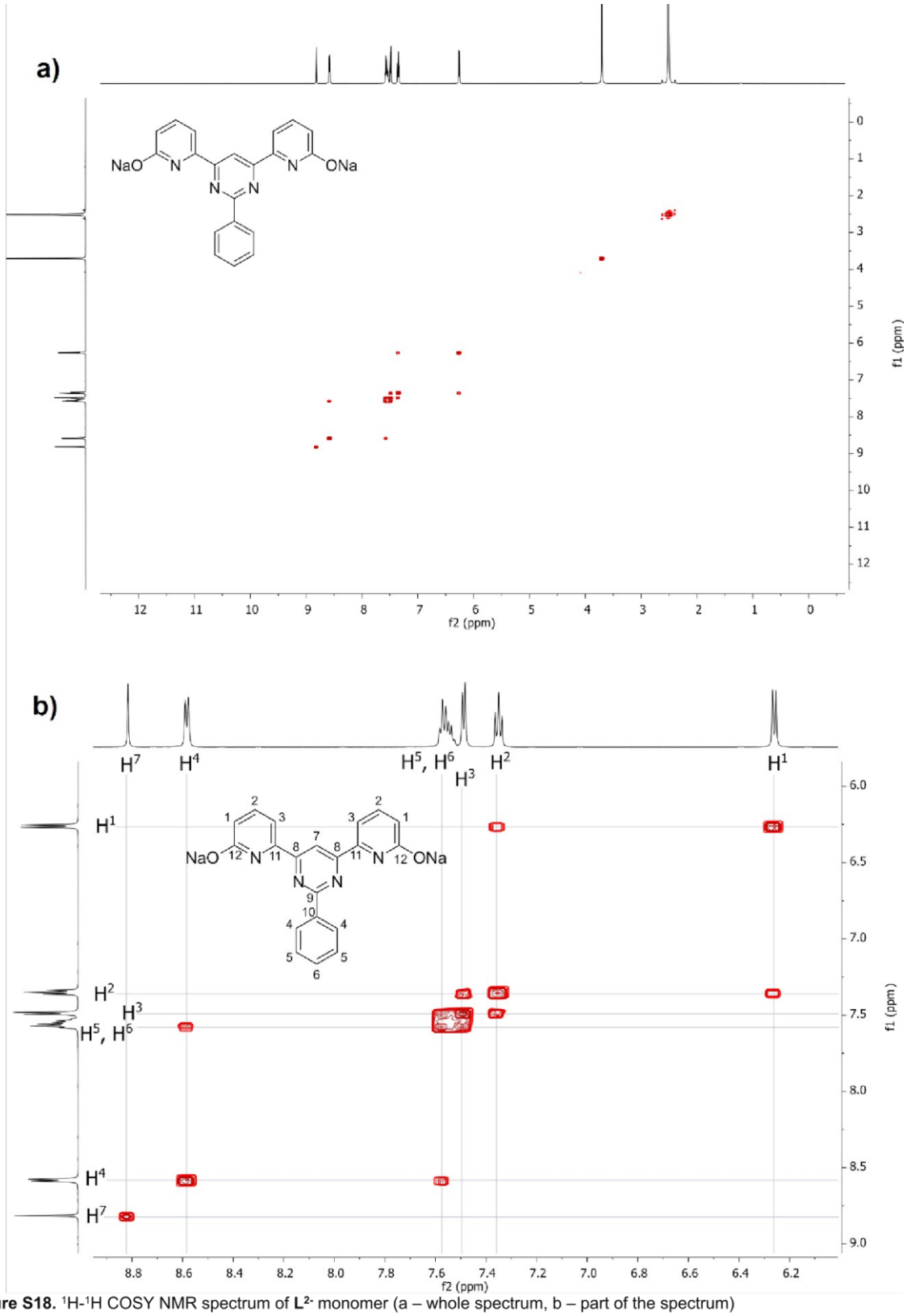

Figure S18. ^{1}H-^{1}H COSY NMR spectrum of $\mathbf{L}^{2-}$ monomer (a – whole spectrum, b – part of the spectrum)

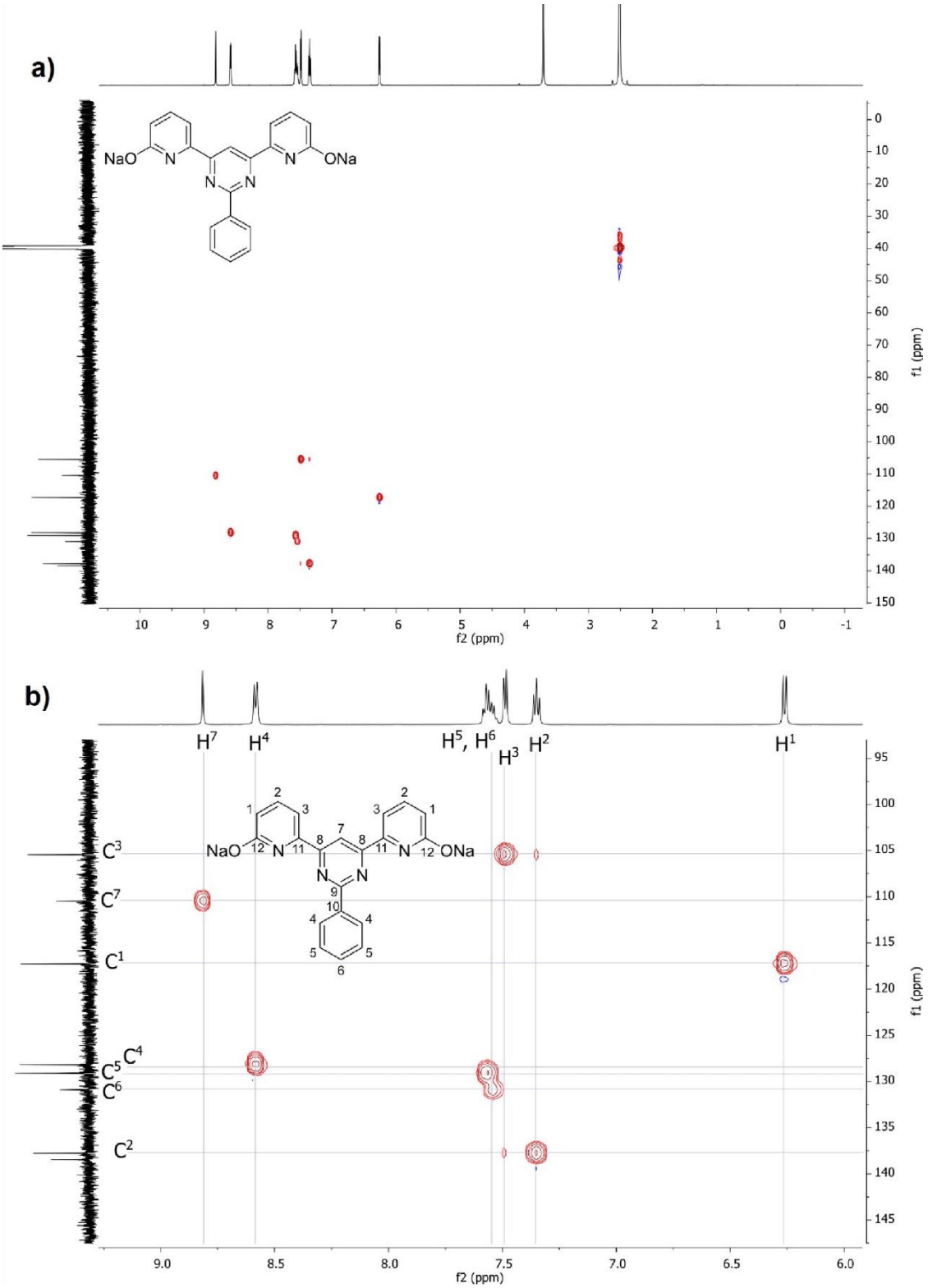

Figure S19. ^{1}H-^{13}C HSQC NMR spectrum of $\mathbf{L^{2-}}$ monomer (a – whole spectrum, b – part of the spectrum)

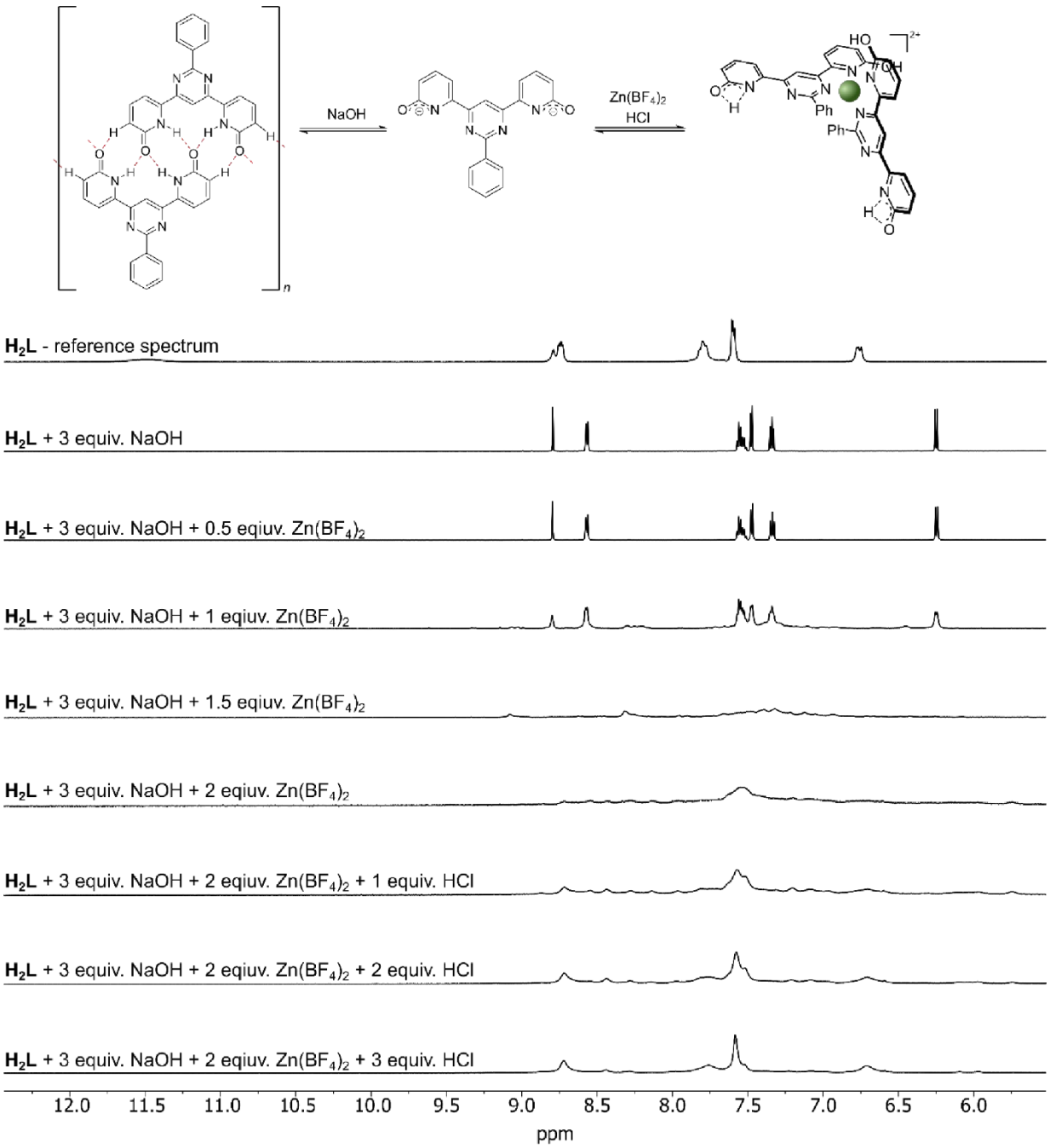

Figure S20. Titration of **H_2L** with NaOH (0.12 M in DMSO-d_6/D_2O = 1:1) causing **L^{2-}** formation, following by incremental addition of $Zn(BF_4)_2$ (0.12 M in DMSO-d_6) and neutralization by HCl (0.06 M, in DMSO-d_6) forming $[Zn(\mathbf{H_2L'})_2](BF_4)_2$.

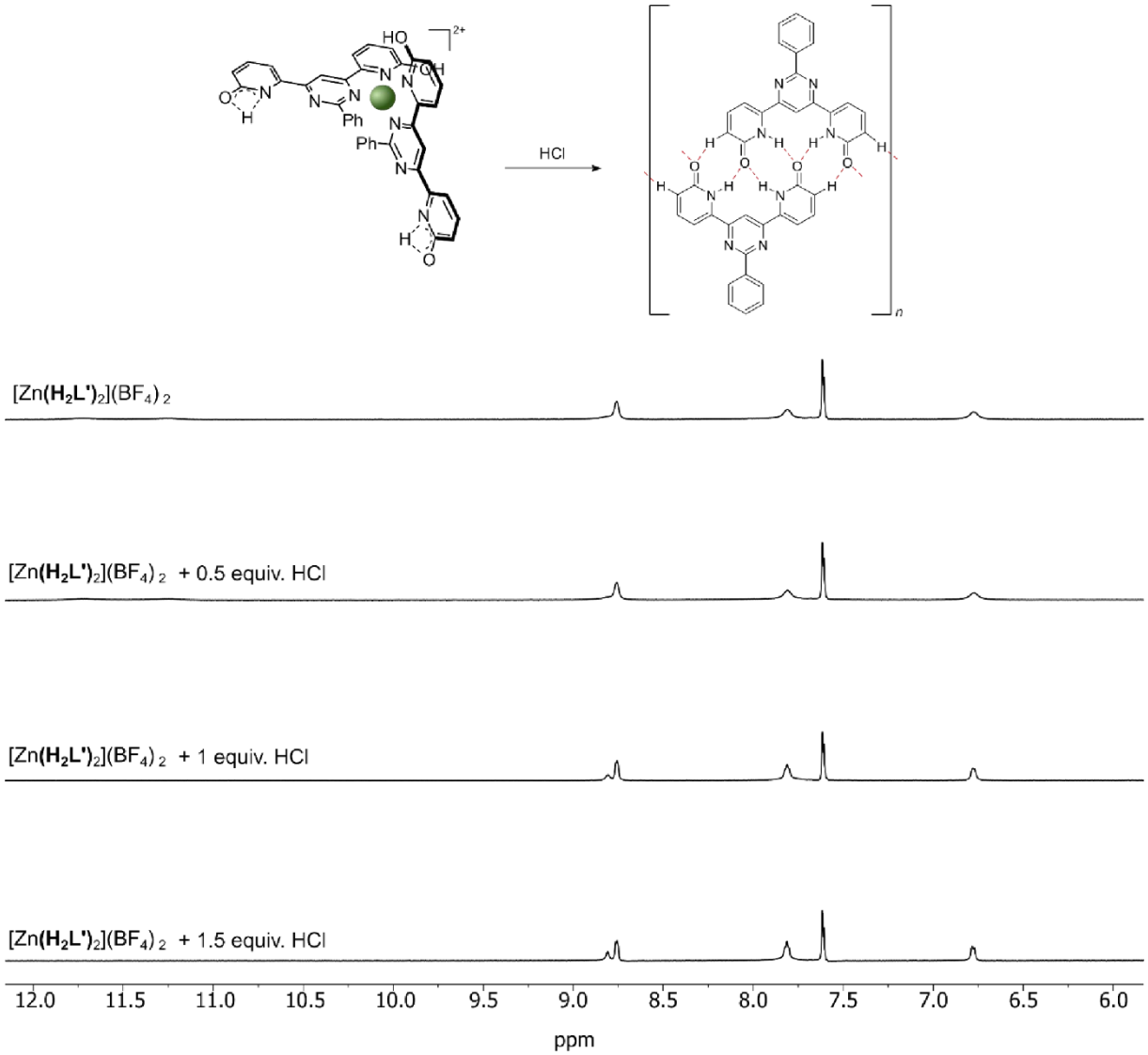

Figure S21. Titration of $[Zn(\mathbf{H_2L'})_2](BF_4)_2$ with HCl (0.06 M, in DMSO-d_6) causing $\mathbf{H_2L}$ formation.

II. MOLECULAR MODELLING

The main goal of this ab-initio studies was to predict and depict the structures formed by ligand **H_2L** and its' iminol form **H_2L'**, including hydrogen-bonded aggregates and complex $[Zn(\mathbf{H_2L'})_2](BF_4)_2$. A multi-step procedure was used to optimize the studied structures. The obtained structures were used as a blueprint for visualisation of polymeric species. All structures were pre-optimised with the semi-empirical RM1 method. The parameters for zinc atom were taken from the AM1 method. For **H_2L**, **L^{2-}** and **H_2L'**, the lowest-energy conformations were found using Gaussian's gmmx module. The input structures were then optimised with the DFT b3lyp/6-31+(g,d) method, which is a fair compromise between differing natures of the studied species and computational expenses, and ensures comparability of the results. To include dispersion effects, Grimme's D3 dispersion was added and complemented by Becke-Johnson (BJ) damping parameters for close-ranged interactions. Additional diffusion functions were included to correctly reproduce behaviour of anionic species. Polarization functions were added on hydrogen and the heavy atoms to reproduce correctly hydrogen. First, 2-pyridone and 2-pyridone dimer were optimized. The DFT functional PBE with base 6-31++G(d,p) was used and the calculation results obtained did reflect values reported in literature[1].

Table S1. The results of energy calculations of 2-pirydone molecule for monomeric and dimeric species. The H-Bond energy calculations were used for comparison to earlier reported values.

	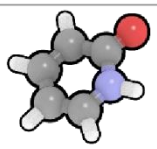	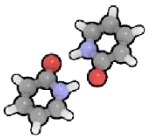	
Base	2-pirydone [10^5 kcal mol^{-1}]	2-pirydone dimer [10^5 kcal mol^{-1}]	H-Bond [kcal mol^{-1}]
pbepbe/6-311++g(d)	-2.0282	-4.0567	-20.55
ED3 correction	-	-4.0567	-6.78

Next was the optimisation of the **H_2L** structure itself. The **H_2L** molecule exists in amido-iminol tautomeric forms. The amido-form was found to be more stable (form C, Figure S1). Calculated single point energies for tautomers **H_2L** and **H_2L'** show that **H_2L** has total energy lower by about 24.3 kJ/mol than **H_2L'**.

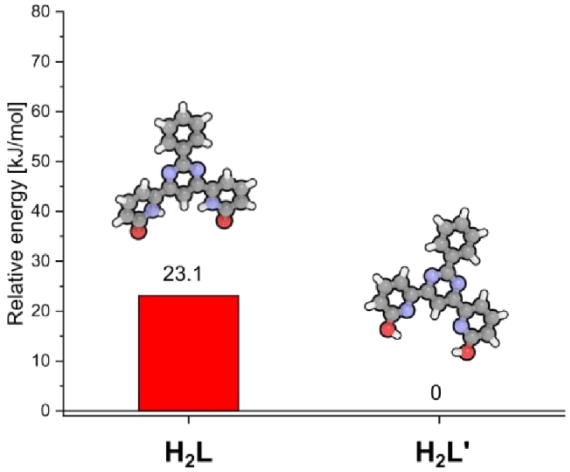

Figure S22. Relative energy of **H_2L** and **H_2L'** The total energy of molecules was obtained using b3lyl/6-31+g(d,p) methodology and gd3bj dispersion and damping.

Intrinsic properties of a molecule can be predicted based on the distribution of energy levels of highest occupied molecular orbital (HOMO) and lowest unoccupied molecular orbital (LUMO). While the MO structure for both **H_2L** and **H_2L'** shows symmetrical pattern, the introduction of metal cation shows the shift of electronic cloud of bonding HOMO level towards the metal centre and shift of LUMO levels to the opposite side of molecule. For analysis 6-31g++(d,p) calculations for optimised structures of molecules were used.

Table S2. Frontier orbilals analysis.

MO	H_2L	H_2L'	$[Zn(H_2L')_2](BF_4)_2$
LUMO +4	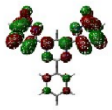	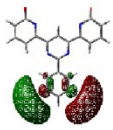	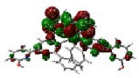
LUMO +3			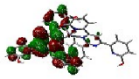
LUMO +2			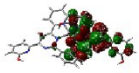
LUMO +1		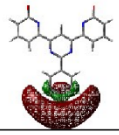	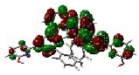
LUMO	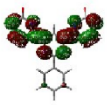	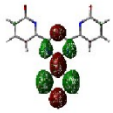	
HOMO	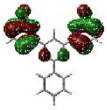	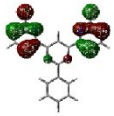	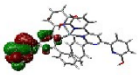
HOMO −1	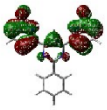	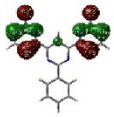	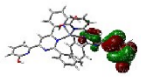
HOMO −2	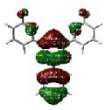	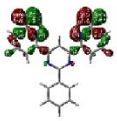	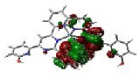

HOMO −3	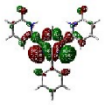	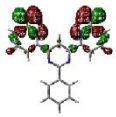	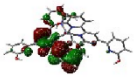
HOMO −4	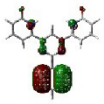	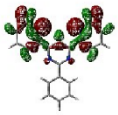	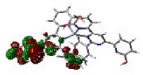

H_2L, L^{2-} anion and $[Zn(H_2L')_2](BF_4)_2$ structure description

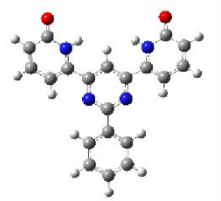

H_2L: This structure can occur in several conformations, from of which the one shown, has the lowest energy. The pyridone rings are set relative to each other in a trans configuration, deflected relative to the plane of the central pyrimidine ring by about 21° in opposite directions. The phenyl ring is slightly displaced from the plane of the pyrimidine ring by a dihedral angle of 5.7 Å. The length of the C=O bonds in this molecule is 1.23 Å, while the N-C bonds of the amide group are 1.41 Å.

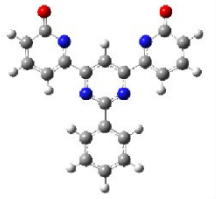

L^{2-} anion: The anionic form of iminol form of the structure was found to be flat. The length of the C-O bonds in this molecule is 1.26 Å, while the N-C bonds of the amide group are 1.39 Å.

$[Zn(H_2L')_2](BF_4)_2$: The structure of the complex consists of two ligand molecules in the iminol form, coordinated to the Zn^{2+} cation by the nitrogen atoms of the pyrimidine-pyridine pocket. The Zn-N bond lengths for pyridine nitrogen atoms are slightly longer than for pyrimidine nitrogen atoms, the average lengths of these bonds are 2.08 Å and 2.01 Å, respectively. The zinc cation is coordinated with the symmetry of a distorted tetrahedron. The dihedral angles between the pyridine and central ring are small for the coordinating unit, i.e. about 1-13°, while for phenyl rings, angles are on average 20.7°, which is similar to the free form **H_2L**. The dihedral angles between the phenyl ring and the pyrimidine ring have an average value of 36°. The bond lengths are as follows: C-O 1.34 Å, C-N 1.34 Å.

SambVca 2.1 steric hindrance results

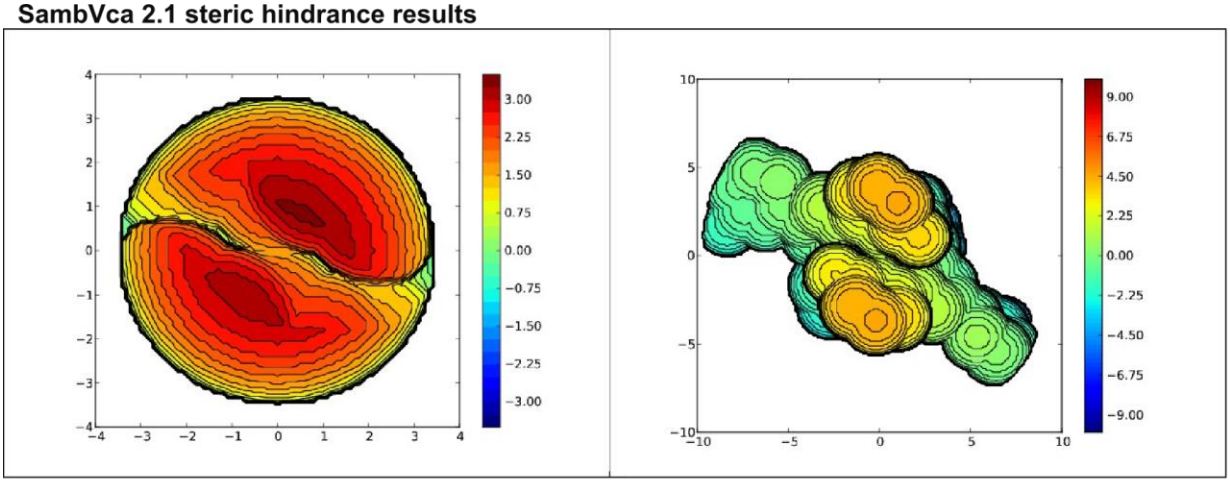

Figure S23. Steric maps calculated in SambVca software[2] for complex $[Zn(\mathbf{H_2L'})_2](BF_4)_2$. Standard (3.5 Å) and enlarged (10 Å) radii were used.

Table S4. SambVca 2.1 steric hindrance results.

%V Free	**%V Buried**			
10.8	**89.2**			
Quadrant	**V_{free}**	**V_{bur}**	**$\%V_{free}$**	**$\%V_{bur}$**
SW	6	38.9	**13.4**	86.6
NW	5.8	39	**13**	87
NE	2.7	42.2	**6**	94
SE	4.8	40	**10.8**	89.2

III. SCANNING TUNNELING MICROSCOPY

General methods for STM experiments:

The solution was prepared by dissolving dynamer $\mathbf{H_2L}$ or complex $[Zn(\mathbf{H_2L'})_2](BF_4)_2$ in DMSO at slightly elevated temperatures (heat gun) and, additionally, in tricholorobenzene (TCB). For the measurements, a 20 µL drop of 5 µM of solution was casted onto the surface and heated up (using heating plate) to a temperature of 50-65 °C (determined empirically). The temperature was measured using a type K thermocouple spot-welded to the edge of the sample holder. The scanning was performed inside the solution drop, i.e. at the solid-liquid interface. The bias voltage was applied to the sample.

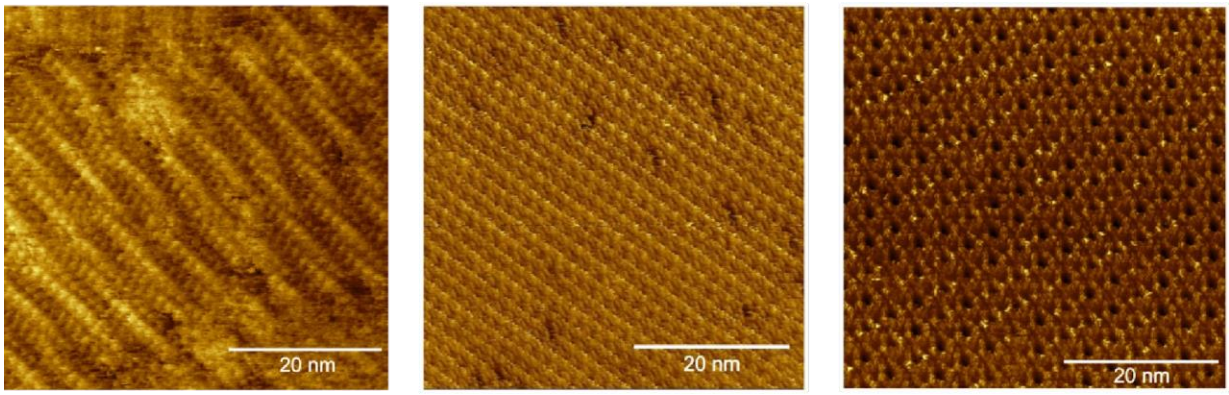

Figure S24. STM images of helical $\mathbf{H_2L}$ (left) $\mathbf{H_2L}$ 2D arrays (middle) and $[Zn(\mathbf{H_2L'})_2](BF_4)_2$ (right). Images size: 50 × 50 nm^2; V_{sample} = +0.6 V; I_T = 0.1 nA.

Both STM images of helical polymer $\mathbf{H_2L}$ (Fig. S24 left) and of 2D array of complex $[Zn(\mathbf{H_2L'})_2](BF_4)_2$ (Fig S24 right) were obtained from same sample by drop-casting 20 µL of 5 µM solution of $[Zn(\mathbf{H_2L'})_2](BF_4)_2$ onto HOPG and heating to 50-65 °C. This coexistence of both helical dynamers and 2D arrays made by complex $[Zn(\mathbf{H_2L'})_2](BF_4)_2$ can be interpreted as confirmation of dynamic equilibrium between $\mathbf{H_2L}$ and $[Zn(\mathbf{H_2L'})_2](BF_4)_2$. STM image of 2D array of $\mathbf{H_2L}$ (Fig. S24 middle) was obtained by drop-casting 20 µL of 5 µM of $\mathbf{H_2L}$ solution onto HOPG and heating to 50-65 °C.

Using the methodology proposed by Gao et al[3], for the given experimental conditions of the STM experiment, we compared the shape and the contours of the LUMO orbitals with the recorded STM images. The obtained structure match very well to the toroidal shapes in the STM image.

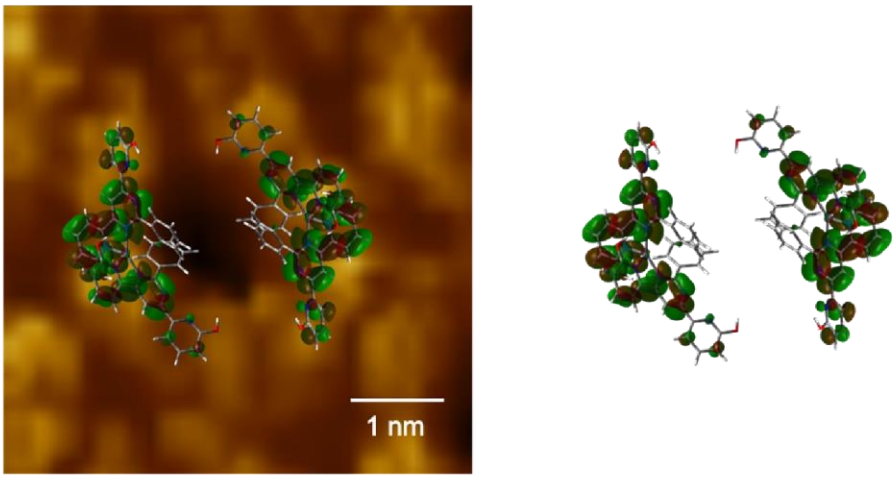

Figure S25. Zoomed area of STM image of $[Zn(\mathbf{H_2L'})_2](BF_4)_2$ 2D arrays with model of LUMO orbitals of 2 molecules of $[Zn(\mathbf{H_2L'})_2](BF_4)_2$ on top of it (left). Image size: 5 × 5 nm^2; V_{sample} = +0.6 V; I_T = 0.1 nA. LUMO orbitals of 2 molecules of $[Zn(\mathbf{H_2L'})_2](BF_4)_2$ (right).

References

[1] Ciesielski, A., Stefankiewicz, A. R., Hanke, F., Persson, M., Lehn, J. M., & Samorì, P. *Small* **2011**, *7*, 342–350.
[2] Falivene, L. et al. *Nat. Chem.* **2019**, *11*, 872.
[3] H. T. Zhou, J. H. Mao, G. Li, Y. L. Wang, X. L. Feng, S. X. Du, K. Müllen, H. J. Gao, *Applied Physics Letters* **2011**, *99*, 153101.

A2: Schiff base caped gold nanoparticles for transition metal cations sensing in organic media

ChemComm

ROYAL SOCIETY OF CHEMISTRY

COMMUNICATION

View Article Online
View Journal | View Issue

Cite this: *Chem. Commun.*, 2022, 58, 5773

Received 25th January 2022,
Accepted 10th April 2022

DOI: 10.1039/d2cc00497f

rsc.li/chemcomm

Schiff base capped gold nanoparticles for transition metal cation sensing in organic media†

Miroslava Čonková,‡[ab] Verónica Montes-García,‡[c] Marcin Konopka,[ab] Artur Ciesielski,*[bc] Paolo Samorì*[c] and Artur R. Stefankiewicz*[ab]

We report a fast and ultrasensitive colorimetric method for the detection of transition metal ions (Fe^{3+}, Cu^{2+}, Ni^{2+}) in a mixture of toluene–acetonitrile using Schiff base functionalized gold nanoparticles. We achieved limits of detection for the three metal ions at least two orders of magnitude lower than the EU recommended limits. Finally, our methodology was assessed for the determination of nickel in the organic waste of a relevant industrial reaction.

The fine chemical, petroleum, and pharmaceutical industries have been identified as major producers of chemical waste because the vast majority of technological processes are still carried out in organic solvents with the use of metal-based catalysts.[1] Organic medium hitherto remains essential not only for chemical reactions to proceed but also for the extraction and purification steps, necessary to achieve sufficient product purity. Despite the continuous development and improvement of synthetic methodologies, waste including that containing transition metal ions derived from decomposed catalysts is also often a source of contamination of the final product, including in active pharmaceutical ingredients (APIs).[2] Although some of the transition metal ions employed in catalytically relevant processes (e.g., Cu^{2+}, Ni^{2+}, and Fe^{3+}) bear several important biological roles,[3–5] their excessive content in the human body can lead to serious health problems.[6] EU recommended limits in APIs are 20 ppm[7] and 300 ppm[7] for Ni^{2+} and Cu^{2+}, respectively. No specific limit has yet been established so far for Fe^{3+}, although overexposure to this metal can lead to iron poisoning,[8] including heart diseases[9] and cancer.[10] Analytical methods commonly exploited for trace metal ion determination, despite the high capital cost, are ion-coupled-plasma spectroscopy (ICP-MS)[11,12] and atomic absorption spectrometry (AAS).[12] However, the direct determination of trace elements in non-aqueous mixtures by these techniques remains problematic due to time-consuming and highly invasive sample pre-treatment (e.g., mineralization, high temperature/pressure) often leading to variation in metal content.[12] Within this context, the development of simple and effective methods to detect transition metal ions in organic media is highly sought after.

Low-dimensional nanostructures possess the highest surface-to-volume ratios and unique optoelectronic properties, which are highly susceptible to their interaction with the environment. The latter can be tuned via the chemical functionalization of their surface with receptors of the analyte of choice, enabling the development of chemical sensors with electrical or optical readouts featuring key performance indicators beyond the state-of-the-art.[13] Among low-dimensional nanostructures, noble metal nanoparticles (NPs) represent versatile platforms for the fabrication of (bio)-chemical sensors due to their high chemical stability, surface-to-volume ratio, and distinctive optoelectronic properties. The extraordinary plasmonic phenomenon has given rise to a rapidly developing field of optical nanosensors,[14] where the exposure to target analytes can induce a localized surface plasmon resonance (LSPR) shift of the metallic NPs (in solution or deposited into a solid platform) and may be accompanied by a visual colour change. In particular, colorimetric sensing, where a specific analyte can trigger a significant visual colour change, is very attractive due to its simplicity, cost-effectiveness, and unprecedented selectivity among the traditional detection methodologies.[15]

On the other hand, Schiff bases derived from 2-hydroxybenzaldehydes and appropriate amine or hydrazide create a very effective chelating system for binding to metal cations.[16,17] They have also been employed for colorimetric ion sensing, reaching in some cases limits of detection in the micromolar range.[18–21] However, their synergetic combination with metal NPs for colorimetric cation sensing has been barely exploited. For instance, gold nanoparticles (AuNPs) functionalized with

[a] Faculty of Chemistry, Adam Mickiewicz University, Uniwersytetu Poznańskiego 8, 61-614 Poznań, Poland. E-mail: ars@amu.edu.pl
[b] Center for Advanced Technology, Adam Mickiewicz University, Uniwersytetu Poznańskiego 10, 61-614 Poznań, Poland
[c] Université de Strasbourg, CNRS, ISIS, 8 allée Gaspard Monge, 67000 Strasbourg, France
† Electronic supplementary information (ESI) available. See DOI: https://doi.org/10.1039/d2cc00497f
‡ These authors contributed equally to this work.

View Article Online

Schiff bases can effectively detect Cu^{2+}, Al^{3+}, or Fe^{3+}, exhibiting sensitivities in the micromolar range.[22–24] Yet most examples combining AuNPs and Schiff bases were investigated in aqueous solutions, despite the high stability of AuNPs capped by Schiff base ligands in organic media.[25,26] Examples of sensors combining AuNPs with Schiff base ligands capable of efficiently sensing selected metal ions in organic solvents remain very few.[24,27]

To fill this gap, we report here a new type of colorimetric sensor based on Schiff-base decorated AuNPs for the detection of industrially relevant transition metal cations (Cu^{2+}, Ni^{2+}, and Fe^{3+}) in organic solvents. The employed chelating system (L1) was designed to act both as a stabilizing agent of AuNPs and as a supramolecular receptor for the analyte of interest.

Ligand L1 was designed to combine a moiety that is capable of chemisorbing on gold surfaces and a versatile coordination pocket that can efficiently bind metal cations. Thus, an a-lipoic acid moiety was chosen as the anchoring site, through the formation of an Au–S linkage,[28–31] while the mono(salicylaldehyde)-iminoacetyl-hydrazone ligand providing the N,O,O binding pocket[16,32–34] was employed for coordinating metal cations, as confirmed in the control experiment with ligand L2 (see ESI†). Ligand L1 was synthesized from a-lipoic acid via a three-step protocol in a high 75% overall yield without column chromatography (see Scheme S1, ESI†). The final ligand L1 was obtained as a mixture of two geometrical isomers (in Z:E = 2:1 ratio calculated from integrals of H-9_{cis}, H-9_{trans} and H-11_{cis}, H-11_{trans}). Detailed synthetic procedures and characterization can be found in the ESI,† Fig. S1–S8.

The synthesis of monodispersed AuNPs in toluene was performed by following a previously reported protocol, where oleylamine was used as a surfactant.[35] The resulting oleylamine capped gold nanoparticles (OL@AuNPs) featured a plasmon band at 526 nm, ascribed to the dipole resonance of individual AuNPs (Fig. 1b). The interactions between the gold nanoparticle surface and the amine group of oleylamine are weaker than dative Au–S bonds, and hence this favours the ligand exchange reaction between oleylamine and ligand L1. The ligand exchange reaction should be achieved by adding approximately 890 L1 molecules per nanoparticle (calculated from the size of the metal core, for details see ESI†). To maximize the number of L1 molecules on the AuNPs surface, and hence have the maximum number of receptors, we performed the ligand exchange reaction with different concentrations of ligand L1 (i.e., from 7.5 to 60 mM) and we studied the stability of the AuNPs in time (see ESI,† Fig. S12). The highest concentration of ligand L1 that lead to a stable system during at least 96 hours was 15 mM; higher concentrations lead to a fast and irreversible aggregation of the system (see ESI,† Fig. S12C and D).

The size and the morphology studies of both OL@AuNPs and L1@AuNPs were performed by transmission electron microscopy (TEM) and dynamic light scattering measurements (DLS). TEM images of OL@AuNPs revealed monodispersed spherical nanoparticles with uniform shape and core size 11.5 1.2 nm (Fig. 1c), which is in good agreement with DLS measurements, revealing an average hydrodynamic diameter of 14.3 4.4 nm (for details see ESI,† Fig. S13 and S14). In the

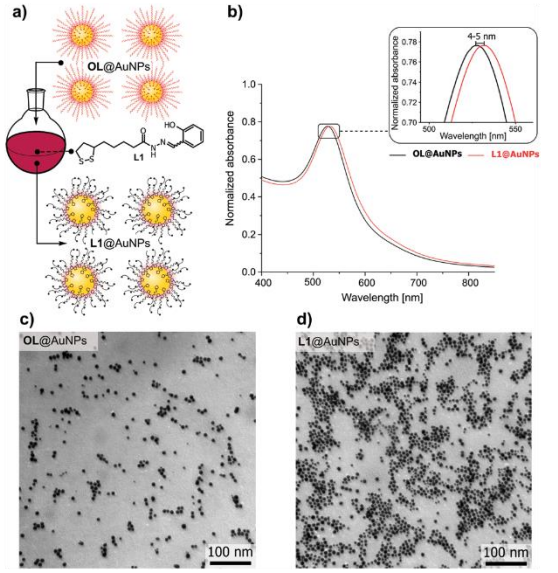

Fig. 1 (a) Schematic representation of the ligand exchange reaction; (b) UV-Vis comparison of OL@AuNPs and L1@AuNPs; (c) TEM image of OL@AuNPs (d) TEM image of L1@AuNPs.

case of L1@AuNPs, TEM images revealed that the AuNP size remains constant (core size: 10.8 1.1 nm, Fig. 1d) as ligand L1 is not expected to modify the NP size. This is in good agreement with DLS measurements, which showed an average hydrodynamic diameter of L1@AuNPs of 15.45 4.26 nm (see ESI,† Fig. S13).

To evaluate the sensing performance, our system was tested for the selected transition metal ions (Cu^{2+}, Ni^{2+}, and Fe^{3+}). To rule out nonspecific acetonitrile-induced aggregation we have verified the stability of L1@AuNPs in the presence of acetonitrile up to 23% (see ESI,† Fig. S15). To demonstrate the selective interactions between ligand L1 and metal cations, colloidal dispersions of OL@AuNPs were exposed to selected metal cations and no aggregation was observed (see Fig. S16a, S17a, and S18a in ESI†). These experiments also exclude any non-specific interaction with AuNPs. To eliminate the counter ion influence, all experiments were performed by using NO_3^- salts. After 10 minutes of analyte addition (for a detailed description see ESI†), a visible colour change from red to purple was observed indicating the aggregation of L1@AuNPs (See Fig. 2). The response time observed for our system is better or comparable with other known colorimetric sensors (see ESI,† Table S4).[36–40] The aggregation of L1@AuNPs is triggered by the coordination reaction between the N-acylhydrazone moiety and the metal cation, giving rise to octahedral complexes (Fig. 2). Solely based on naked-eye observation, the colour change from red to purple can be observed in the 5–7.5 mM concentration range (Fig. S19 in ESI†). To be easily comparable to the EU recommended limits, we converted the concentration in which colour change was noted into ppb. More specifically, for Cu^{2+}

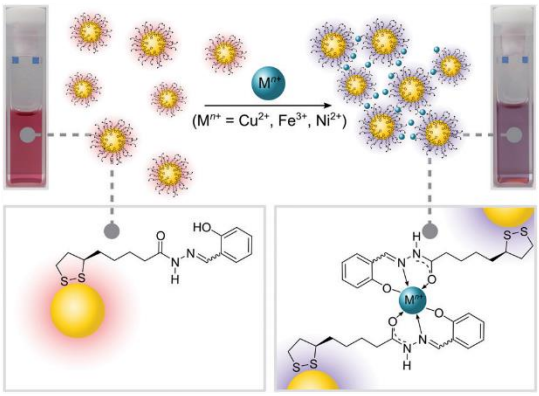

Fig. 2 Schematic representation of coordination triggered aggregation.

cations, the visible colour change took place after the addition of 5 mM, which corresponds to 366 ppb. For Fe^{3+} cations it was 7.5 mM (458 ppb) and 5 mM of Ni^{2+} cations, which corresponds to 204 ppb (see ESI,† Fig. S19). As compared to the allowed limits of transition metal ions in APIs and an excipient,[7] our sensor exhibited a sensitivity 2 and 3 orders higher.

The sensing performance of the L1@AuNPs was quantitatively assessed via UV-Vis spectroscopy. The UV-vis absorbance spectrum of L1@AuNPs upon each metal ion addition at different concentrations showed a red shift of the LSPR band (Fig. 3a, b, and c, for Cu^{2+}, Fe^{3+}, and Ni^{2+} ions, respectively). The calibration curves were obtained by plotting known concentrations of Cu^{2+}, Ni^{2+} or Fe^{3} ions (1–10 mM) against the LSPR maximum (Fig. 3d and Table S1 in ESI†) and the linear response can be fitted to the formula: $LSPR_{max} = a$ [metal ion] + b. For calculating the limit of detection (LoD) of each metal ion, the $3S_B/m$[41] equation was used, where S_B is the standard deviation of a blank sample and m is the slope of each calibration curve, also known as sensitivity (S). The colorimetric

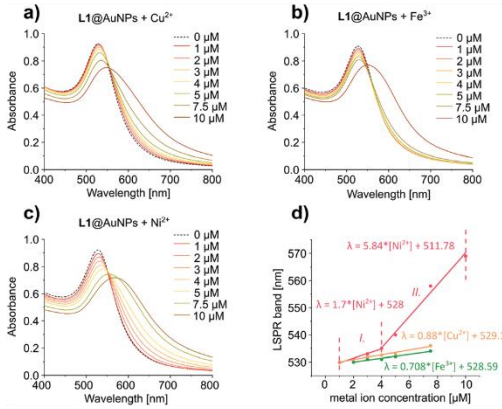

Fig. 3 (a) UV-Vis spectrum showing the LSPR band shift upon addition of Cu^{2+}, (b) Fe^{3+} and (c) Ni^{2+}; (d) linear change of LSPR maximum plotted as a function of metal ion concentration.

sensor in toluene–acetonitrile solutions showed extremely low LoDs, in the range 1.4–11.2 nM (see ESI,† Table S1) for the assessed metal ions.

As can be seen in Fig. 3d, the sensor showed a similar sensitivity in the case of Cu^{2+} and Fe^{3+} cations (S = 0.88 and 0.71 nM ^{1}, respectively). However, the sensitivity towards the most catalytically valuable and the most toxic of all studied cations, i.e. Ni^{2+}, was much higher in both linear regions (S = 1.7 and 5.84 nM ^{1}). This high sensitivity towards Ni^{2+} can be further utilized in industrially valuable Ni-catalyzed reactions, such as the synthesis of Pictilisib[42] or PDE472.[43] Usually, Ni^{2+}, Cu^{2+} and Fe^{3+} cations are not found as a mixture in industrial processes and hence we highlight that our colorimetric sensor can be used to detect all of them individually. When compared to other known colorimetric sensors based on Schiff bases, L1@AuNPs displayed 2–6 orders of magnitude lower LoD than structurally similar Schiff base capped AuNP sensors, which were described for Cu^{2+}[22,27] and Al^{3+}[23] detection.

To demonstrate that our sensor can be used for the quantitative evaluation of metal content in organic waste produced during catalytic processes used in the pharmaceutical industry, we decided to reproduce the synthetic protocol reported by Novartis Pharma AG, that utilizes nickel catalyzed Kumada coupling for the synthesis of PDE472, an inhibitor of phosphodiesterase type 4D and a recognized drug target for the treatment of asthma.[43] The reaction was performed at a laboratory scale and the organic waste was analyzed by UV-vis spectroscopy with our sensor and by inductively coupled plasma mass spectrometry (ICP-MS). Right after the purification procedure, the toluene waste (50 mL) was added to the L1@AuNP dispersion (for more details see ESI†). The UV-vis spectrum was recorded after 10 minutes and showed a red shift of the LSPR band (4 nm, see ESI,† Fig. S22), similar to the red shift observed for low concentrations of Ni^{2+} ions (r 4 mM, see ESI,† Fig. S17d). On the basis of this UV-Vis experiment and the calibration curve obtained upon the addition of a known concentration of Ni^{2+} ions (Fig. S17d, ESI†), the Ni^{2+} content in the real sample was evaluated as 3.5 mM. The exact nickel content was determined by ICP-MS. The obtained value of 3.49 mM is in full agreement with our UV-vis results. It is worth highlighting that for ICP-MS measurements the organic waste had to be evaporated, dried and mineralized prior to measurement, which in total took several hours. On the other hand, for our sensing experiment, the organic waste was directly examined by UV-vis spectroscopy without any pre-treatment, which reduced the total analysis time to a few minutes.

We have devised a highly sensitive chemical sensor of divalent and trivalent metal ions based on Schiff base capped AuNPs via colorimetric detection. These low-dimensional sensitive elements were characterized by UV-vis spectroscopy, DLS, and TEM. The colorimetric response relies on the complexation of the metal ions with the Schiff base ligand, forming ML_2-type complexes with first-row transition metal ions (Ni^{2+}, Cu^{2+}, Fe^{3+}) in toluene–acetonitrile solution, which triggers the AuNP aggregation process. The metal coordination occurred in less than 10 minutes, which makes this sensor suitable for on-the-spot

qualitative sensing. The sensitivity performance was excellent for all studied ions, and the colorimetric response visible solely by the naked eye (no instrumentation necessary) was as low as 204 ppb for Ni^{2+} ions, which is two orders of magnitude lower than the EU recommended limits. The estimated LoD for all studied metal ions was in the nanomolar range and the highest sensitivity was observed for the toxic and catalytically valuable Ni^{2+} cations.

Significantly, our chemical sensor outperforms other known Schiff base capped AuNP colorimetric sensors, with a 3–6 orders of magnitude lower LoD. Moreover, we demonstrated the applicability of our sensor for the evaluation of the Ni^{2+} content in organic waste generated during the synthesis of PDE472, a recognized drug target for the treatment of asthma. The modular strategy applied can tune the sensor on-demand and it can be refined to become suitable for the selective detection of transition metal ions for pharmaceutical and technological applications in organic solvents.

The activity in Poznań was funded by the National Science Centre of Poland grant: SONATA BIS 2018/30/E/ST5/00032 (A.R.S.) and co-funded by The National Centre for Research and Development grant: POWR.03.02.00-00-I032/16 (M.C.). The activity in Strasbourg was financially supported by European Commission through the ERC project SUPRA2DMAT (GA-833707), the AMI project funded by the ERA-NET EuroNanoMed III program, the European Union and the Agence Nationale de la Recherche (ANR) GA-ANR-17-ENM3-0001-01, the Labex project CSC (ANR-10LABX-0026 CSC) within the Investissement d'Avenir program ANR-10-IDEX-0002-02, the International Center for Frontier Research in Chemistry (icFRC) and the Institut Universitaire de France (IUF). We thank Prof. Danuta Barałkiewicz and Dr Adam Sajnóg for ICP-MS measurements.

Conflicts of interest

There are no conflicts to declare.

Notes and references

1 S. Abou-Shehada, J. H. Clark, G. Paggiola and J. Sherwood, Chem. Eng. Process., 2016, 99, 88–96.
2 European Medicine Agency, Guideline on the Specification Limits for Residues of Metal Catalysts, London, 2007.
3 R. Crichton, Inorganic Biochemistry of Iron Metabolism: From Molecular Mechanisms to Clinical Consequences, John Wiley & Sons, Ltd, 2001.
4 A. Sass-Kortsak, Adv. Clin. Chem., 1966, 8, 1–67.
5 F. Sunderman, Ann. Clin. Lab. Sci., 1977, 7, 377–398.
6 R. R. Crichton, in Metal Chelation in Medicine, ed. R. J. W. Robert R Crichton, Robert C Hider, 2016, ch. 1, pp. 1–23.
7 European Medicine Agency, ICH guideline Q3D (R1) on elemental impurities, 2019.
8 C. G. Fraga, Mol. Aspects Med., 2005, 26, 235–244.
9 M. L. Rasmussen, A. R. Folsom, D. J. Catellier, M. Y. Tsai, U. Garg and J. H. Eckfeldt, Atherosclerosis, 2001, 154, 739–746.
10 L. E. Beckman, G. F. Van Landeghem, C. Sikstrom, A. Wahlin, B. Markevarn, G. Hallmans, P. Lenner, L. Athlin, R. Stenling and L. Beckman, Carcinogenesis, 1999, 20, 1231–1233.
11 N. Lewen, S. Mathew, M. Schenkenberger and T. Raglione, J. Pharm. Biomed. Anal., 2004, 35, 739–752.
12 E. Bulska and A. Ruszczynska, Phys. Sci. Rev., 2017, 2, 1–14.
13 R. Furlan de Oliveira, V. Montes-Garcia, A. Ciesielski and P. Samori, Mater. Horiz., 2021, 8, 2685–2708.
14 C. Pezzato, S. Maiti, J. L. Chen, A. Cazzolaro, C. Gobbo and L. J. Prins, Chem. Commun., 2015, 51, 9922–9931.
15 V. Montes-Garcia, M. A. Squillaci, M. Diez-Castellnou, Q. K. Ong, F. Stellacci and P. Samori, Chem. Soc. Rev., 2021, 50, 1269–1304.
16 G. Markiewicz, A. Walczak, F. Perlitius, M. Piasecka, J. Harrowfield and A. R. Stefankiewicz, Dalton Trans., 2018, 47, 14254–14262.
17 A. R. Stefankiewicz, J. Harrowfield, A. M. Madalan and J. M. Lehn, CrystEngComm, 2013, 15, 9128–9134.
18 B. Kaur, N. Kaur and S. Kumar, Coord. Chem. Rev., 2018, 358, 13–69.
19 V. K. Gupta, A. K. Singh, M. R. Ganjali, P. Norouzi, F. Faridbod and N. Mergu, Sens. Actuators, B, 2013, 182, 642–651.
20 H. Sun, Y. Jiang, J. Nie, J.-H. Wei, B. X. Miao, Y. Zhao, L.-F. Zhang and Z.-H. Ni, Mater. Chem. Front., 2021, 5, 347–354.
21 Z. Liao, Y. Liu, S.-F. Han, D. Wang, J.-Q. Zheng, X.-J. Zheng and L.-P. Jin, Sens. Actuators, B, 2017, 244, 914–921.
22 Y. Wang, X. Li, Y. Zhou and C. Liu, Int. J. Chem., 2012, 4, 90–95.
23 P. Huang, J. Li, X. Liu and F. Wu, Microchim. Acta, 2015, 183, 863–869.
24 A. A. Jimoh, A. Helal, M. N. Shaikh, M. A. Aziz, Z. H. Yamani, A. Al-Ahmed and J. P. Kim, J. Nanomater., 2015, 2015, 1–7.
25 W. Edwards, N. Marro, G. Turner and E. R. Kay, Chem. Sci., 2018, 9, 125–133.
26 J. M. McMahon and S. R. Emory, Langmuir, 2007, 23, 1414–1418.
27 E. Oliveira, J. D. Nunes-Miranda and H. M. Santos, Inorg. Chim. Acta, 2012, 380, 22–30.
28 A. C. Savage and Z. Pikramenou, Chem. Commun., 2011, 47, 6431–6433.
29 P. D. Beer, D. P. Cormode and J. J. Davis, Chem. Commun., 2004, 414–415, DOI: 10.1039/b313658b.
30 Z. Krpetic, L. Guerrini, I. A. Larmour, J. Reglinski, K. Faulds and D. Graham, Small, 2012, 8, 707–714.
31 J. M. Abad, S. F. Mertens, M. Pita, V. M. Fernandez and D. J. Schiffrin, J. Am. Chem. Soc., 2005, 127, 5689–5694.
32 D.-H. Wang, Y. Zhang, R. Sun and D.-Z. Zhao, RSC Adv., 2016, 6, 4640–4646.
33 Y. Gou, Y. Zhang, J. Qi, Z. Zhou, F. Yang and H. Liang, J. Inorg. Biochem., 2015, 144, 47–55.
34 J.-X. Yu, V. D. Kodibagkar, L. Liu, Z. Zhang, L. Liu, J. Magnusson and Y. Liu, Chem. Sci., 2013, 4, 2132.
35 X. Huang, A. J. Shumski, X. Zhang and C. W. Li, J. Am. Chem. Soc., 2018, 140, 8918–8923.
36 K. Singh, V. Kumar, B. Kukkar, K. H. Kim and T. R. Sharma, Int. J. Environ. Sci. Technol., 2021, DOI: 10.1007/s13762-021-03331-0.
37 J. Das and P. Sarkar, Environ. Sci.: Water Res. Technol., 2016, 2, 693–704.
38 T. Kiatkumjorn, P. Rattanarat, W. Siangproh, O. Chailapakul and N. Praphairaksit, Talanta, 2014, 128, 215–220.
39 T.-B. Wei, P. Zhang, B.-B. Shi, P. Chen, Q. Lin, J. Liu and Y.-M. Zhang, Dyes Pigm., 2013, 97, 297–302.
40 A. K. Yetisen, Y. Montelongo, M. M. Qasim, H. Butt, T. D. Wilkinson, M. J. Monteiro and S. H. Yun, Anal. Chem., 2015, 87, 5101–5108.
41 European Medicine Agency, ICH Topic Q 2 (R1) Validation of Analytical Procedures: Text and Methodology, 1995.
42 Q. Tian, Z. Cheng, H. M. Yajima, S. J. Savage, K. L. Green, T. Humphries, M. E. Reynolds, S. Babu, F. Gosselin, D. Askin, I. Kurimoto, N. Hirata, M. Iwasaki, Y. Shimasaki and T. Miki, Org. Process Res. Dev., 2013, 17, 97–107.
43 P. W. Manley, M. Acemoglu, W. Marterer and W. Pachinger, Org. Process Res. Dev., 2003, 7, 436–445.

Supplementary information to A2

Electronic Supplementary Material (ESI) for Chemical Communications.

Electronic Supplementary Information

Schiff base caped gold nanoparticles for transition metal ions sensing in organic media

Miroslava Čonková,[a,b#] Verónica Montes-García,[c#] Marcin Konopka,[a,b] Artur Ciesielski,[c] Paolo Samori,*[c] and Artur R. Stefankiewicz*[a,b]*

a. Faculty of Chemistry, Adam Mickiewicz University, Uniwersytetu Poznańskiego 8, 61-614 Poznań, Poland. E-mail: ars@amu.edu.pl

b. Center for Advanced Technologies, Adam Mickiewicz University, Uniwersytetu Poznańskiego 10, 61-614 Poznań, Poland.

c. Université de Strasbourg, CNRS, ISIS, 8 alleé Gaspard Monge, 67000 Strasbourg, France.

# These authors contributed equally to this work

Table of Contents

Experimental section

Chemicals. Chemicals were purchased from commercial suppliers (Sigma-Aldrich and TriMen Chemicals) and used as received without further purification.

Characterization techniques. NMR spectroscopic data were performed on a Bruker UltraShield 300 MHz and 600 MHz spectrometers, calibrated against the residual protonated solvent signal (for ^{1}H NMR DMSO-d_6: $\delta = 2.50$; $CDCl_3$: $\delta = 7.26$ for ^{13}C NMR DMSO-d_6: $\delta = 39.52$) and are given in ppm. ESI-MS spectra were recorded on a Bruker Impact HD Q-TOF spectrometer in positive ion mode. IR spectra were obtained with a Jasco 4000 FTIR spectrophotometer, and peak positions are reported in cm^{-1}. UV–vis spectra were recorded on a Jasco V-750 UV–visible spectrophotometer. The size of AuNPs was determined through transmission electron microscopy (TEM) analysis in a Hitachi H 7500 microscope operating at an acceleration voltage of 100 kV and by dynamic light scattering (DLS) using a Zetasizer Nano S (Malvern Instruments, Malvern UK). For ICP-MS experiments concentrated HNO_3 (Suprapur, Merck, Germany) was used to prepare the blank samples, calibration standards and as a digestion reagent. Concentrated HCl (Suprapur, Merck, Germany) was used to prepare the blank samples and calibration standards. A single element Ni (Merck, Germany) standard solution of 1000 mg L^{-1} concentration and a multi-elemental standard solution STD-4 (Perkin-Elmer, USA) containing 10 mg L^{-1} Au were used to prepare the set of calibration standards with concentrations: 0.1, 1, 10, 50 µg L^{-1} in 1% HNO3 and 1% HCl for Ni and Au, respectively. Milli-Q water was used to prepare sample dilutions, blank samples and calibration standards (Direct-Q 3 UV, Merck, Germany). The ICP-MS model 7700x (Agilent, USA) operated in no-gas mode, the isotopes ^{58}Ni and ^{197}Au were measured with the following instrumental settings: Seaspray nebulizer 0.2 mL min-1, Scott double pass spray chamber,

0.1 s dwell times per isotope, 100 sweeps, 3 replicates, 1550 W plasma power and 1.05 mL min-1 nebulizer gas flow rate. The 2 min wash-in time was applied for Au measurement before each standard and sample to reduce the potential memory effects.

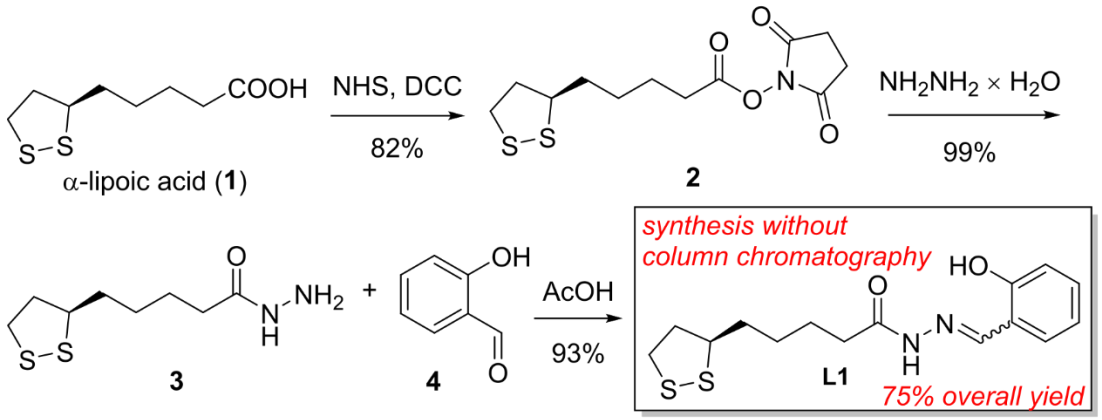

Synthesis of L1:

Scheme S1 *Reagents and conditions*: i) NHS, DCC, CH_2Cl_2, 0°C to rt, 3 h; ii) $NH_2NH_2 \times H_2O$, CH_2Cl_2, rt, 17 h; iii) AcOH, EtOH, rt, 17 h.

Active Ester 2: NHS (308 mg, 2.65 mmol, 1.1 equiv.) was added to a stirring solution of α-lipoic acid (500 mg, 2.4 mmol, 1 equiv.) in dry CH_2Cl_2 (10 mL) under an argon atmosphere and at room temperature. The resulting mixture was cooled to 0 °C by an ice-water bath and a solution of DCC (550 mg, 2.65 mmol, 1.1 equiv.) in dry CH_2Cl_2 (3 mL) was added dropwise. A few seconds after the addition of DDC solution, a white precipitate of DCU started to appear. The cooling bath was removed, and the reaction mixture was allowed to warm up to room temperature, while stirring, for 3 hours. After that, the white solid of DCU was filtered through a small pad of silica and the solvent was removed under reduced pressure. The residue was then purified via recrystallization in a mixture of chloroform (3 mL) and *n*-hexane (100 mL) to give rise to the active ester **2** (600 mg, 1.98

mmol, 82 %), as a white solid. **2**: ^{1}H NMR (600 MHz, DMSO-d_6): δ 1.41-1.52 (m, 2H), 1.54-1.75 (m, 4H), 1.85-1.93 (m, 1H), 2.38-2.46 (m, 1H), 2.68 (t, 2H, J = 7.2 Hz), 2.81 (s, 4H), 3.12 (dt, 1H, J = 6.8 Hz, J = 11.0 Hz), 3.16-3.23 (m, 1H), 3.57-3.66 (m, 1H). ^{13}C NMR (151 MHz, DMSO-d_6): δ 24.0, 25.4, 27.6, 30.0, 33.8, 38.1, 39.8, 55.9, 168.9, 170.2. The physical and spectral data are consistent with those reported.[1]

Hydrazide 3: An excess of hydrazine monohydrate (0.35 mL, 7.16 mmol, 4 equiv.) was added to a stirring solution of the active ester (544 mg, 1.79 mmol, 1 equiv.) in dry CH_2Cl_2 (15 mL). The resulting mixture was stirred at room temperature for 17 hours, after it was quenched with water (40 mL) and extracted with CH_2Cl_2 (3 × 50 mL). The combined organic layers were washed with brine (100 mL) and dried over anhydrous Na_2SO_4. After filtration, the solvent was removed under reduced pressure. Et_2O (5 mL) was added to the residue to precipitate the compound 3, which was then filtered (pale-yellow solid, 394 mg, 1.78 mmol, 99%). Compound 3 should be stored in the fridge under an argon atmosphere. **3**: ^{1}H NMR (600 MHz, DMSO): δ 1.29-1.38 (m, 2H), 1.44-1.74 (m, 4H), 1.82-1.91 (m, 1H), 2.01 (t, 2H, J = 7.4 Hz), 2.37-2.45 (m, 1H), 3.11 (dt, 1H, J = 6.8 Hz, J = 11.0 Hz), 3.16-3.21 (m, 1H), 3.56-3.63 (m, 1H), 4.14 (bs, 2H), 8.91 (bs, 1H). ^{13}C NMR (151 MHz, DMSO): δ 25.0, 28.3, 33.2, 34.1, 38.1, 39.9, 56.1, 171.4. The physical and spectral data are consistent with those reported.[2]

Ligand L1: To a stirring suspension of hydrazide **3** (100 mg, 45.4 μmol, 1 equiv.) in absolute EtOH (10 mL), salicylaldehyde **4** (50 μL, 45.4 μmol, 1 equiv.) and a catalytic amount of acetic acid (0.25 mL) were added. The resulting mixture was stirred for 2 hours at room temperature. After that, the solvent was removed under reduced pressure and to the residue, Et_2O (5 mL) was added to precipitate ligand L1 as a white solid, which was then

filtered (137 mg, 42.2 μmol, 93%). **L1:** mp = 122-123 °C; FT-IR (ATR) ν_{max} = 3186, 3080, 2926, 2849, 1666, 1605, 1580, 1461, 1396, 1206, 770 cm^{-1}; ^{1}H NMR (600 MHz, DMSO): δ 1.34–1.47 (m, 2H), 1.53–1.75 (m, 4H), 1.83–1.92 (m, 1H), 2.23 + 2.58 (2 t, 2H, *J* = 7.3 Hz), 2.36–2.45 (m, 1H), 3.07–3.15 (m, 1H), 3.15–3.22 (m, 1H), 3.58–3.66 (m, 1H), 6.83–6.93 (m, 2H), 7.20–7.30 (m, 1H), 7.49 + 7.61 (2 d, 1H, *J* = 7.5 Hz), 8.25 + 8.34 (2 s, 1H), 10.12 (s) + 11.12–11.25 (m, 1H), 11.12–11.25 (m) + 11. 58 (s, 1H).^{13}C NMR (151 MHz, DMSO): δ 23.9, 24.7, 28.3, 28.4, 31.8, 33.8, 34.1, 34.2, 38.1 (2x), 39.9, 56.1 (2x), 116.1, 116.3, 118.6, 119.2, 119.4, 120.0, 126.7, 129.4, 130.8, 131.1, 140.8, 146.4, 156.3, 157.3, 168.3, 173.7. HRMS – (ESI) calc for $C_{15}H_{21}N_2O_2S_2^+$ $[M+H]^+$ 325.1039, found 325.1042.

MS and FT-IR characterization of L1:

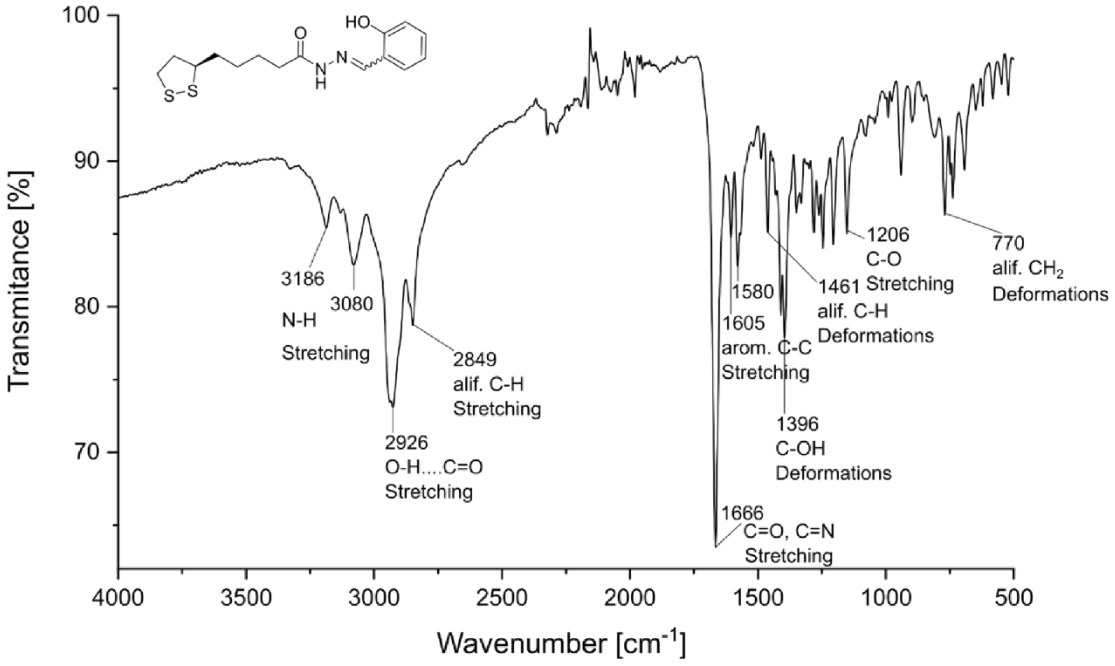

Figure S1. FT-IR (ATR) spectrum of ligand **L1.**

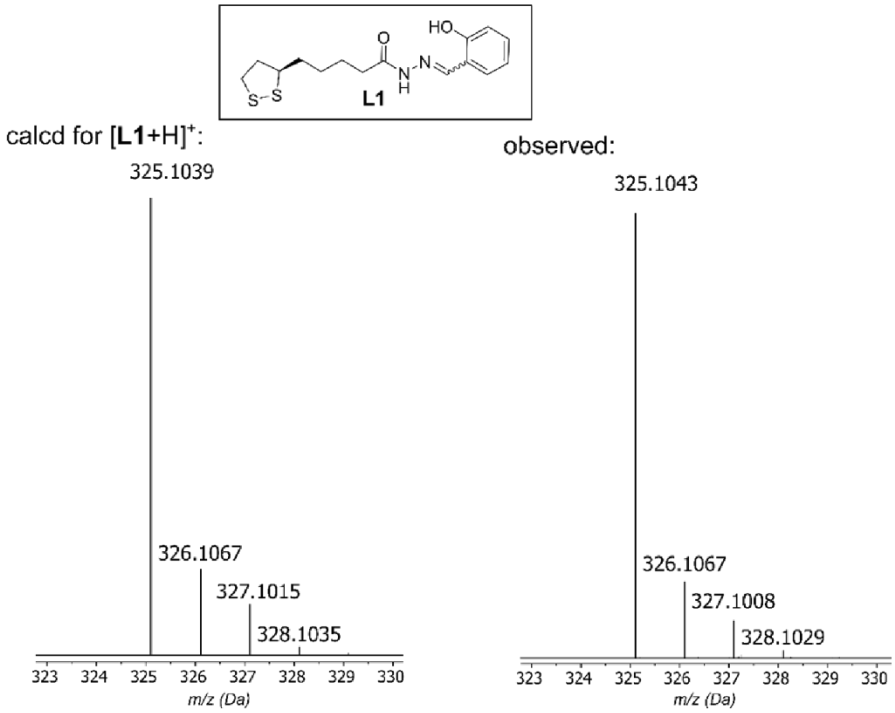

Figure S2. ESI-MS spectra (in positive mode) of ligand **L1.** Calculated on the left and observed on right.

1D and 2D NMR Spectra of L1

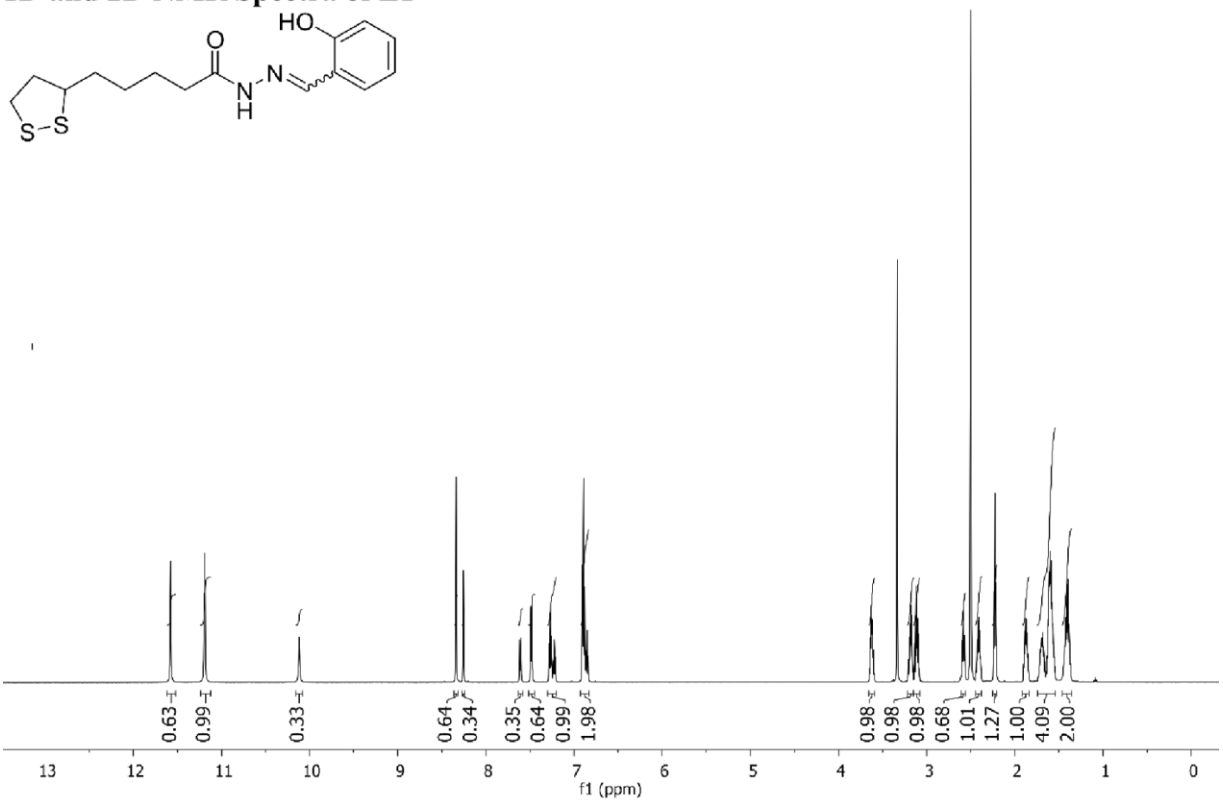

Figure S3. ^{1}H NMR spectrum (600 MHz, DMSO) of ligand **L1**.

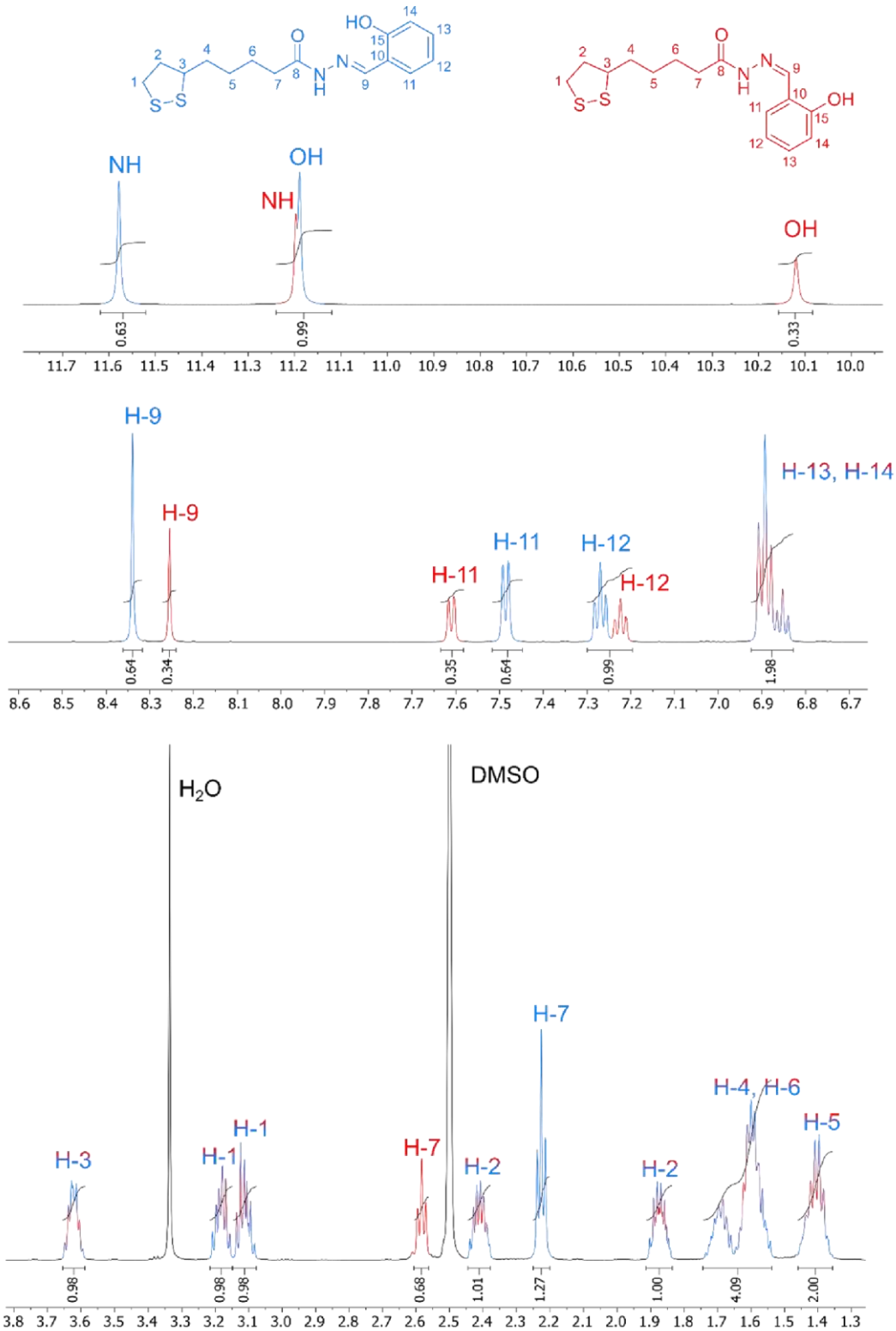

Figure S4. Zoomed areas from ^{1}H NMR spectrum (600 MHz, DMSO) of ligand **L1** with proton assignment (according to 1D and 2D NMR).

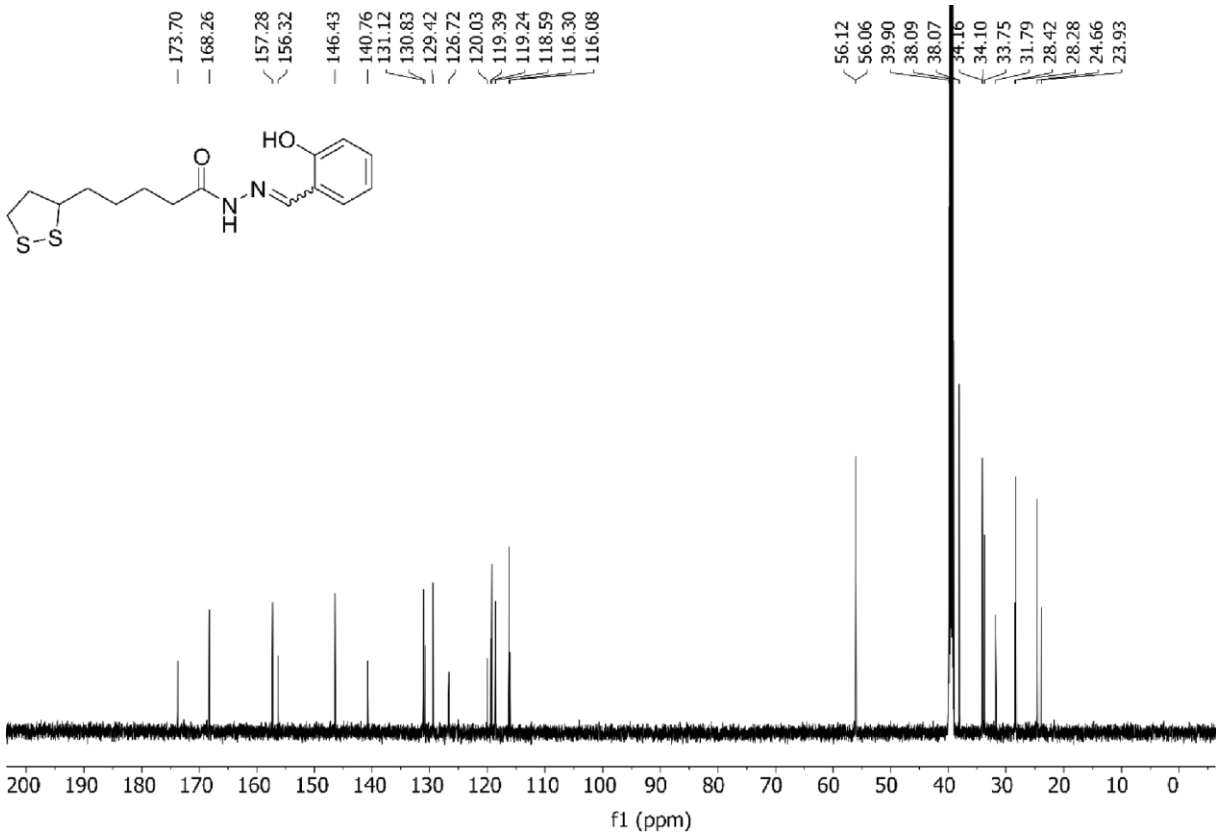

Figure S5. ^{13}C NMR spectrum (151 MHz, DMSO) of ligand **L1**.

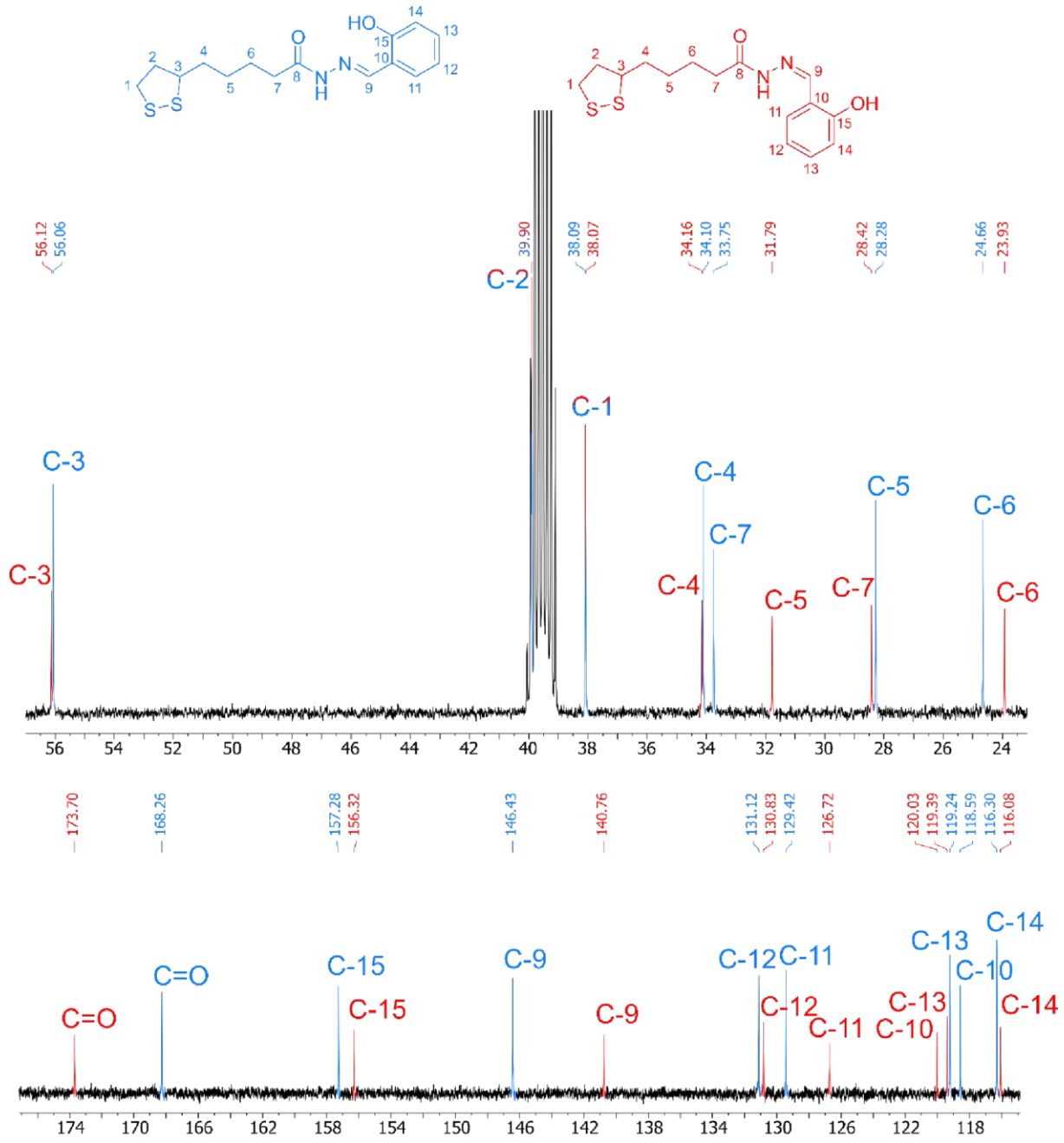

Figure S6. Zoomed areas from ^{13}C NMR spectrum (151 MHz, DMSO) of ligand **L1** with carbon assignment (according to 1D and 2D NMR).

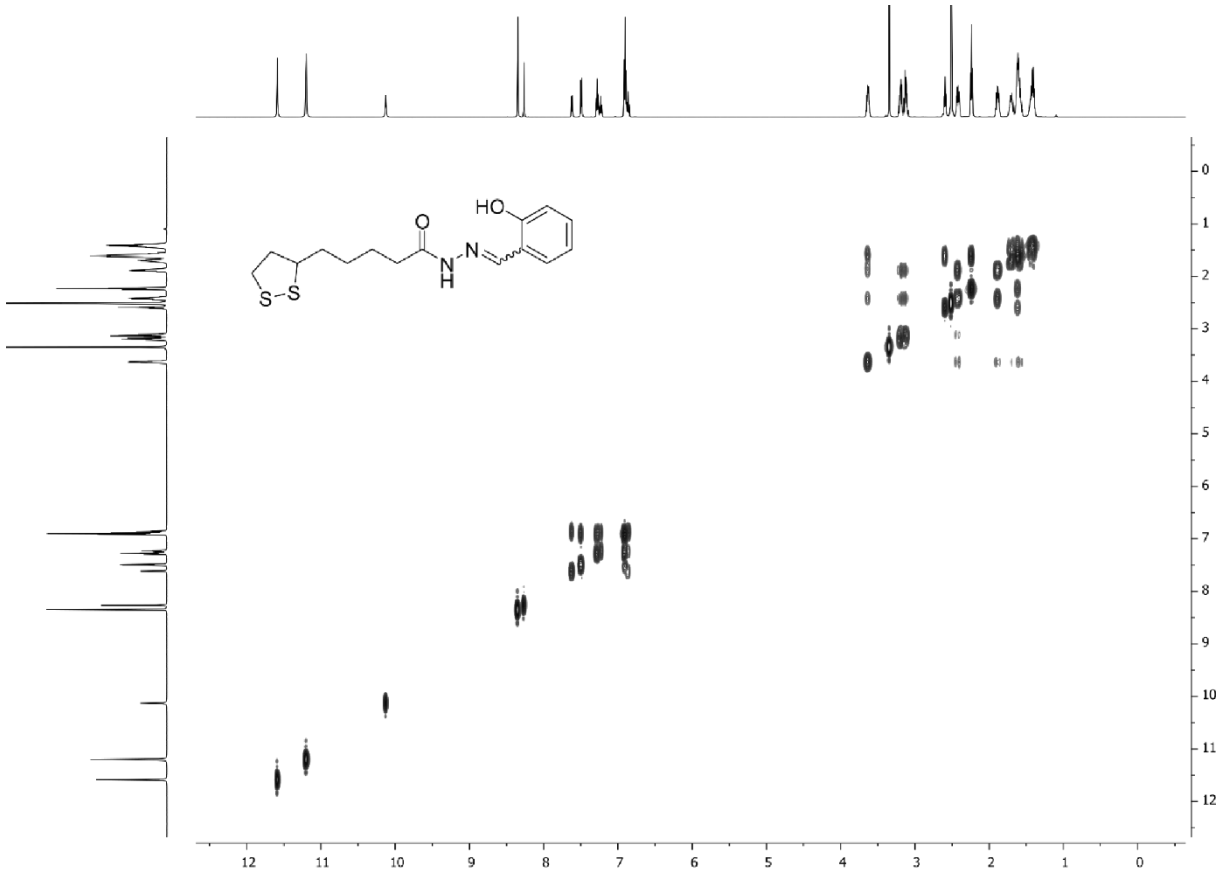

Figure S7. ^{1}H-^{1}H COSY NMR spectrum (600 MHz, DMSO) of ligand **L1**.

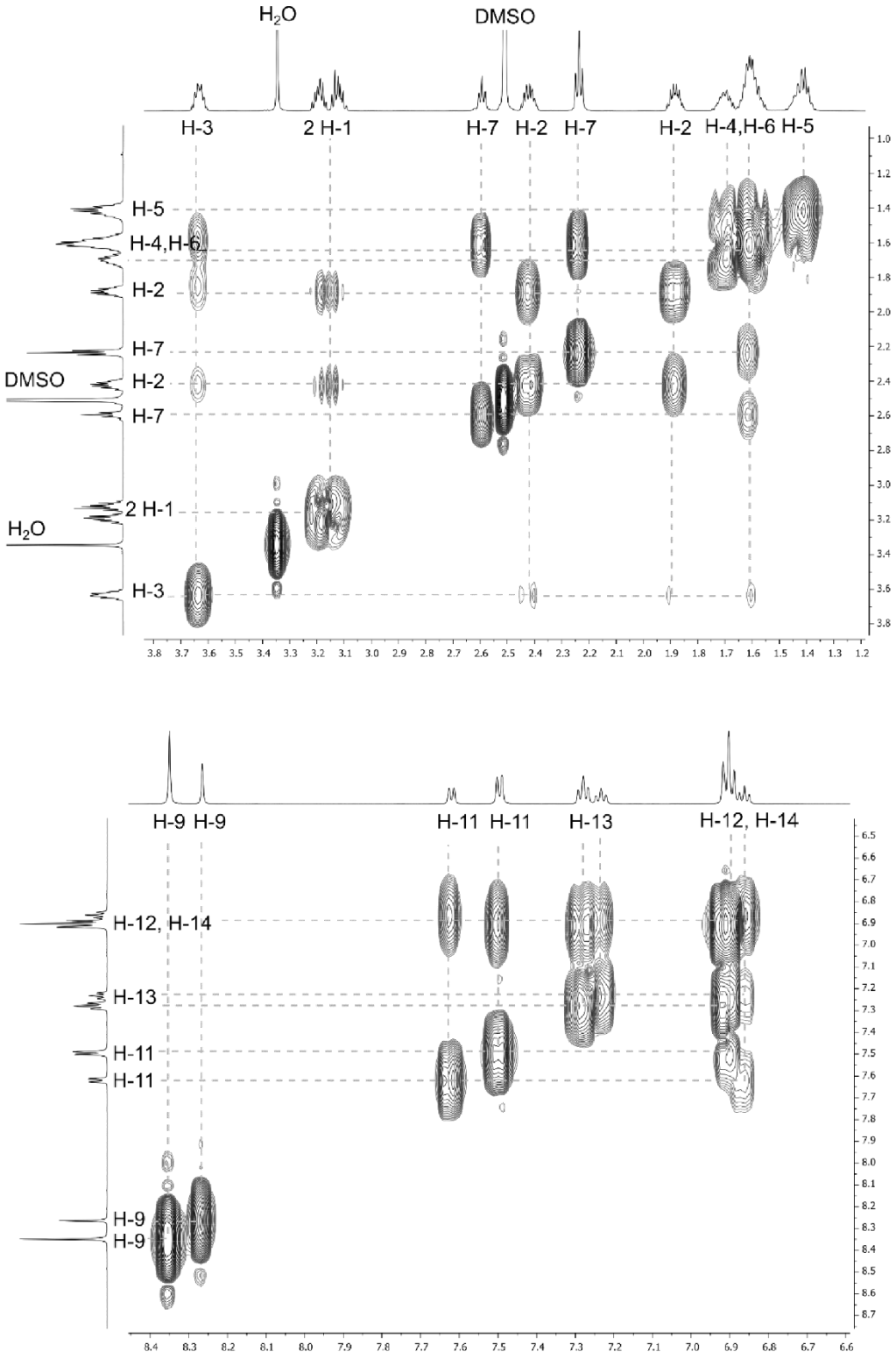

Figure S8. Zoomed areas from ^{1}H-^{1}H COSY NMR spectrum (600 MHz, DMSO) of ligand **L1** with proton assignment (according to 1D and 2D NMR).

Synthesis of L2:

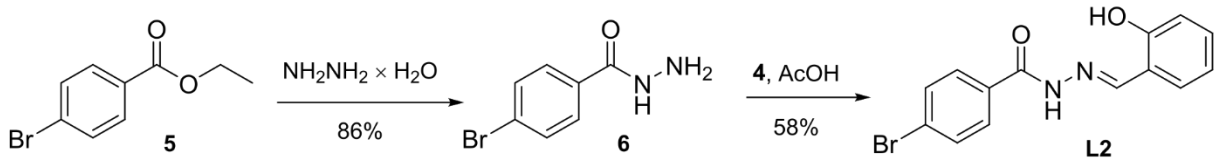

Scheme S2 *Reagents and conditions*: i) $NH_2NH_2 \times H_2O$, EtOH, reflux, 5 h; ii) AcOH, EtOH, 65 °C, 0.5 h.

Hydrazide 6: Hydrazine **6** was prepared according to a previously reported procedure.[3] To a solution of ethyl 4-bromobenzoate **5** (5 g, 21.8 mmol, 1 equiv.) in EtOH (10 mL), hydrazine monohydrate (4 mL, 82.2 mol, 3.8 equiv.) was added in one portion. The mixture was stirred under reflux for 5 hours. After cooling down to room temperature, distilled water was added (15 mL). The precipitated product was filtered and washed with distilled H_2O. Compound 6 was isolated as white solid (4.02 g, 18.7 mmol, 86%). **6**: ^{1}H NMR (300 MHz, DMSO): δ 4.51 (bs, 2H), 7.65 (d, 2H, J = 8.6 Hz), 7.76 (d, 2H, J = 8.6 Hz), 9.86 (bs, 1H). ^{13}C NMR (75 MHz): δ 124.8, 129.1, 131.4, 132.4, 164.9. The physical and spectral data are consistent with those reported.[4]

Ligand L2: To a stirring suspension of hydrazide **6** (1.85 g, 8.6 mmol, 1 equiv.) in absolute EtOH (50 mL), salicylaldehyde **4** (0.9 mL, 8.6 mmol, 1 equiv.) and a catalytic amount of acetic acid (0.15 mL) were added. The resulting mixture was stirred for 30 minutes at 65 °C. Ligand L2 (1.59 g, 5.0 mmol, 58%) was then collected as white crystals by filtration and dried under vacuum. **L2**: ^{1}H NMR (300 MHz, DMSO): δ 6.90–6.95 (m, 2H), 7.28–7.34 (m, 1H), 7.56 (d, 1H, J = 7.7 Hz), 7.77 (d, 2H, J = 8.6 Hz,), 7.89 (d, 2H, J = 8.6 Hz), 8.65 (bs, 1H), 11.21 (bs, 1H), 12.17 (bs, 1H). ^{13}C NMR (75 MHz): δ 116.4, 118.7, 119.4, 125.8, 129.4, 129.7, 131.5, 131.6, 131.9, 148.4, 157.5, 161.9. The physical and spectral data are consistent with those reported.[5]

1D NMR Spectra of L2

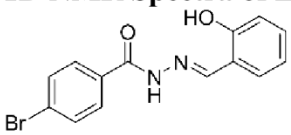

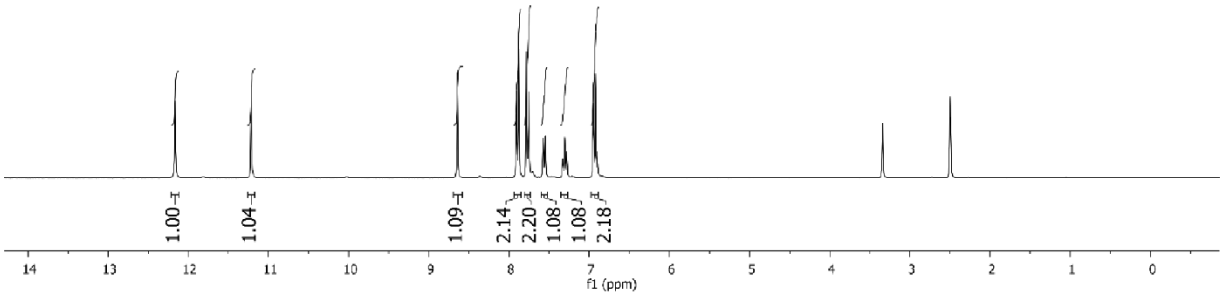

Figure S9. ^{1}H NMR spectrum (300 MHz, DMSO) of ligand **L2**.

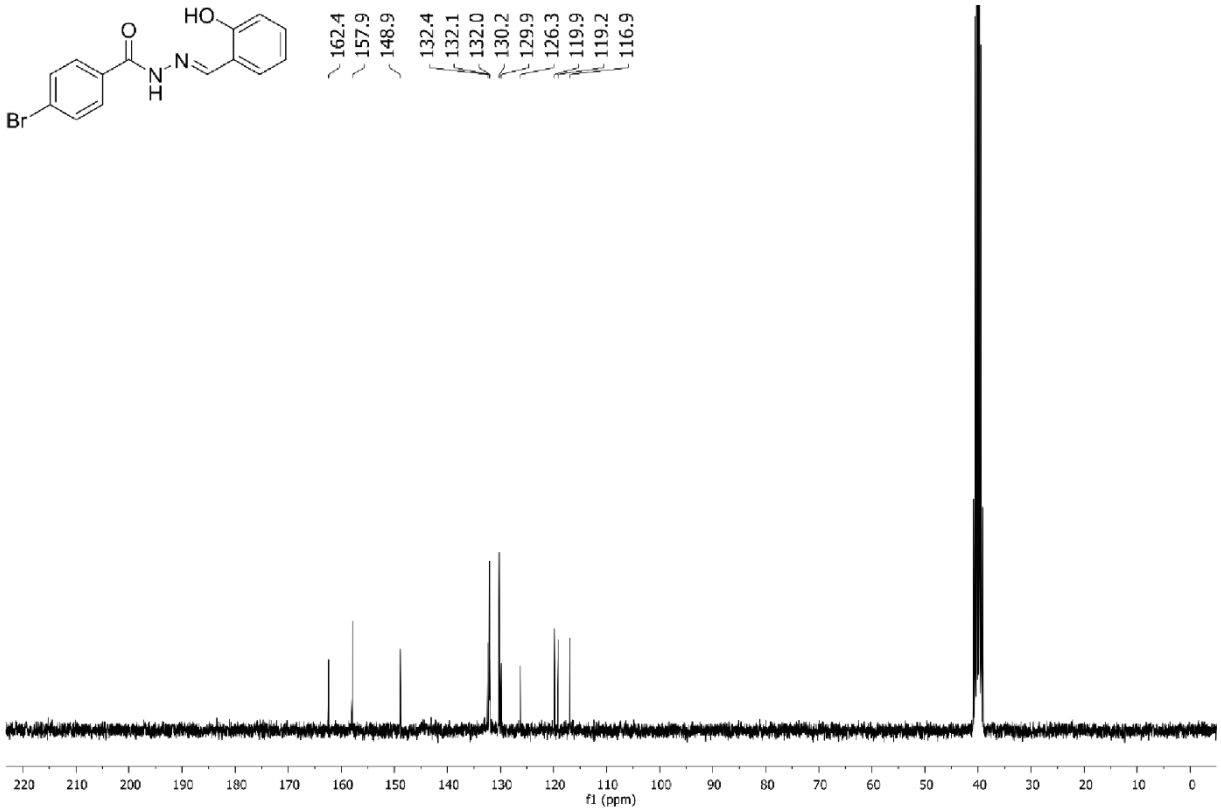

Figure S10. ^{13}C NMR spectrum (75 MHz, DMSO) of ligand **L2**.

To evaluate the effectiveness of the proposed chelating system in the coordination of the selected d-electron metal ions, ligand **L2**, in which the α-lipoic acid moiety was replaced by a –Br group, was also synthesized (Scheme S2, Fig. S9 and S10). This structural change was implemented to avoid potential competing reactions between metal ions and the unbound lipoic acid moiety, which is known to form complexes via disulphide–metal interaction.[6, 7] Complexation reactions of **L2** with several transition metal ions (Fe^{3+}, Cu^{2+}, Ni^{2+}, all as nitrate salts) were conducted in acetonitrile, followed by recrystallization of the products by addition of diethyl ether. Based on the assumptions that the ligand would function as a tridentate chelate and that the chosen metal ions would adopt octahedral coordination, the reaction mixtures were composed with an M:L2 ratio of 1 : 2. This has

been confirmed by mass spectrometry, where signals consistent with the presence of $[M(L2)_2]$ (M=Cu, Ni) and $[M(L2)_2]+$ (M=Fe) species have been found (Fig. S11).

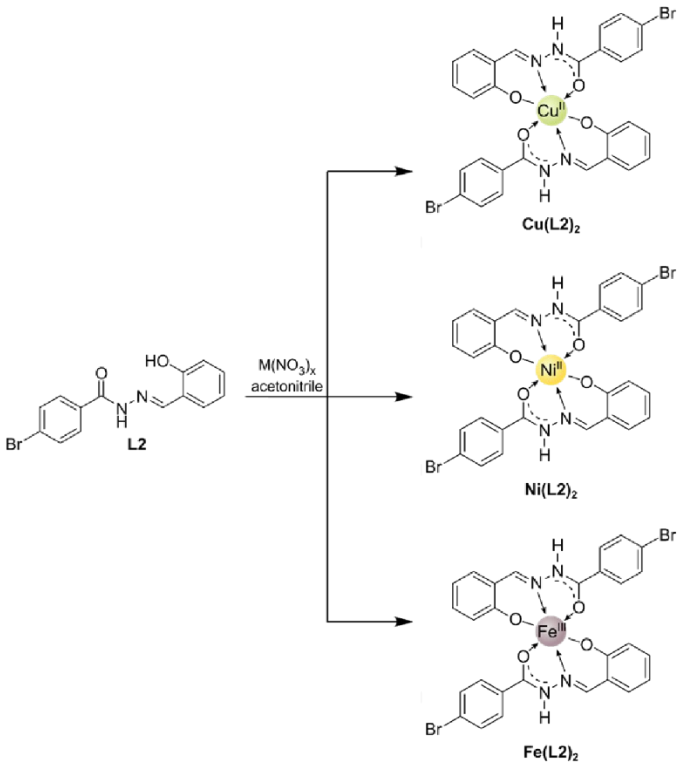

Scheme S3 Schematic representation of **$Cu(L2)_2$**, **$Ni(L2)_2$** and **$Fe(L2)_2$** synthesis.

General procedure for the complex (L2-Mx+) preparation: To the suspension of **L2** (50 mg, 0.156 mmol) in acetonitrile (5 mL) a metal salt (0.078 mmol, 0.5 equiv.) was added. The mixture was stirred for 24 hours at room temperature. After that, the solvent was evaporated, and the product was recrystallized from CH_3CN/Et_2O mixture to obtain the product (71-85 %).

MS Spectra of Complexes $Cu(L2)_2$, $Ni(L2)_2$ and $Fe(L2)_2$

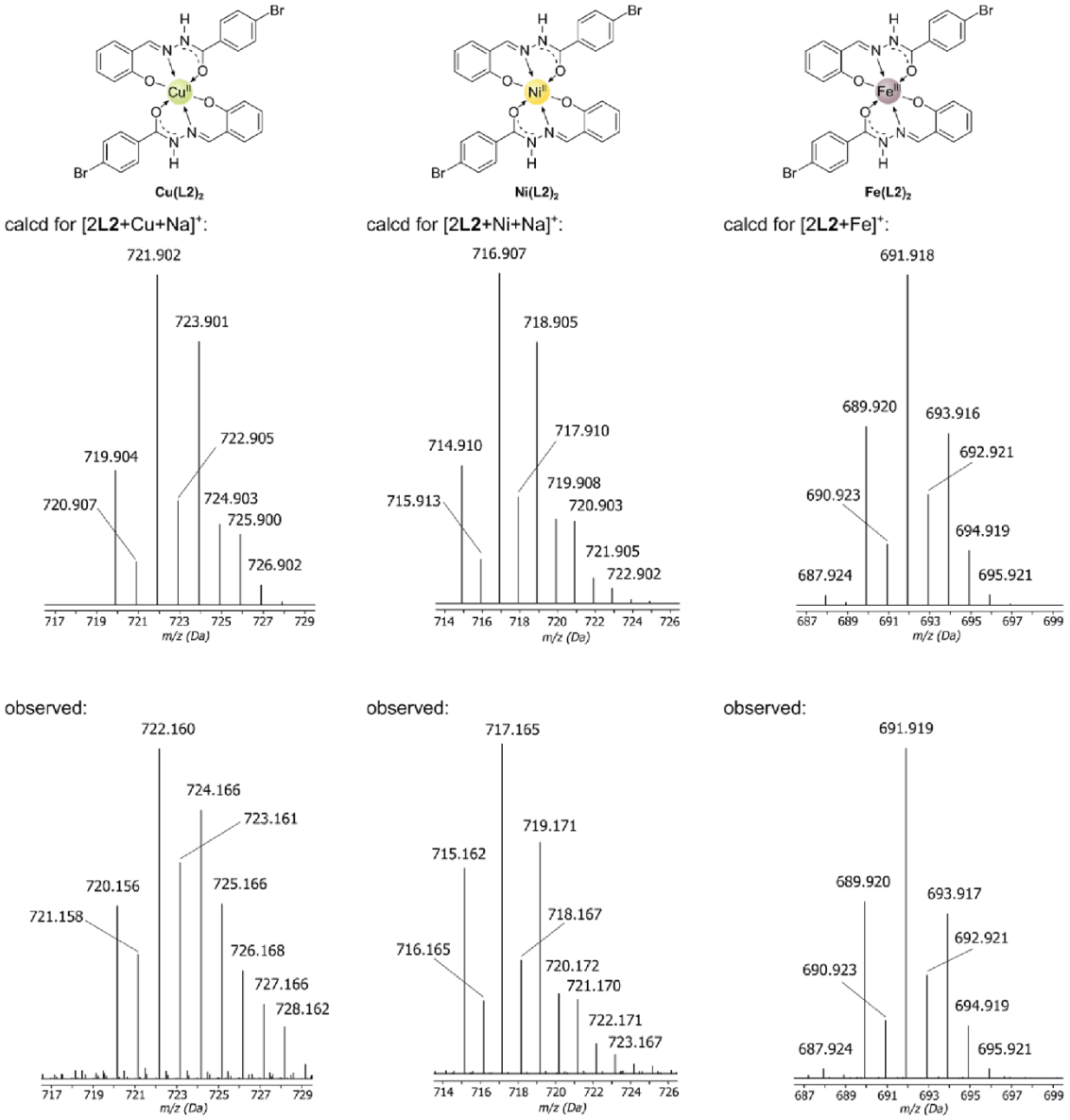

Figure S11. ESI-MS spectra (in positive mode) of complexes **$Cu(L2)_2$**, **$Ni(L2)_2$** and **$Fe(L2)_2$.** Calculated on top and observed on the bottom.

Synthesis of gold nanoparticles

Gold nanoparticles were synthesized according to a reported procedure.[8] In detail: $HAuCl_4$ $3H_2O$ (50 mg, 0.127 mmol) was dissolved in oleylamine (12.7 mL). The mixture was sonicated for 30 minutes to dissolve $HAuCl_4$ $3H_2O$ completely. Then, the solution was heated at 110 °C under vigorous stirring for 40 minutes. In a few minutes, the initial orange solution turned colourless and short after deep red. After letting the mixture cool down to room temperature, EtOH was added (30 mL) to precipitate the gold nanoparticles. The solution was then centrifuged at 384 RCF for 10 minutes to remove the excess of reactants. Toluene (3 mL) was added to re-disperse gold nanoparticles and then EtOH (20 mL) was added to precipitate the gold nanoparticles again. The solution was centrifuged at 384 RCF (Relative Centrifugal Force) for 10 minutes. This washing procedure was repeated twice. After that, toluene (12.6 mL) was added to prepare a 10 mM solution in terms of a gold metal, which is stable for up to several weeks when stored in the fridge. Au NPs concentration was determined by UV-Vis spectroscopy on the basis of extinction at 400 nm.[9] All glassware was rigorously cleaned in aqua regia before use.

General procedure for ligand exchange reaction:

To roughly estimate the needed amount of ligand **L1** needed for such a reaction we started from purely geometrical considerations: The diameter distribution of our AuNPs, roughly to ~11 nm was determined by transmission electron microscopy (Figure S14). From theoretical and experimental studies on Au/thiolated SAMs, reported the n literature, it is known that the maximum molecular density of alkanethiol SAMs, on flat Au [111], amounts ~ 4.5 molecules/nm^2. [10, 11] By considering the higher steric hindrance of ligand **L1**, compared to aliphatic chains, and

that for particles bigger than 5.2 nm the curvature radius is negligible at molecular scales[10, 12], it is possible to conclude that the upper limit for the density of molecules in the AuNPs-ligand **L1** SAM is equal 4.5 molecules/nm^2. Therefore, each nanoparticle cannot react with more than 890 ligand **L1** molecules. By knowing the concentration, size, and amount of active sites for reaction with the thiols group we could estimate an approximate stoichiometric ratio between AuNPs and ligand **L1** solution to achieve a complete ligand exchange.

These calculations were a quick and useful guide and a start point for finding the right conditions for the ligand exchange. We set up test concentrations of **L1** to 7.5 μM, 15 μM, 30 μM and 60 μM. Stock **OL**@AuNPs solution concentration was set to 1 mM (in toluene, in terms of metal) to form 0.5 mM solution after the addition the same volume of **L1** solution in toluene.

Gold nanoparticles (**OL**@AuNPs) solution in toluene (1 mM in terms of gold metal, 2 mL) was added to a solution of **L1** (7.5-60 μM, 2 mL) in toluene under vigorous stirring. After the addition, the mixture was kept in dark for 96 hours. For the evaluation of the stability UV-Vis measurements were performed in different time intervals (up to 96 hours). The resulting functionalized gold nanoparticles were diluted with toluene to a concentration of 0.25 mM (in terms of gold metal) and further used in the sensing experiments without additional purification steps due to the negligible amount of unbound **L1**.

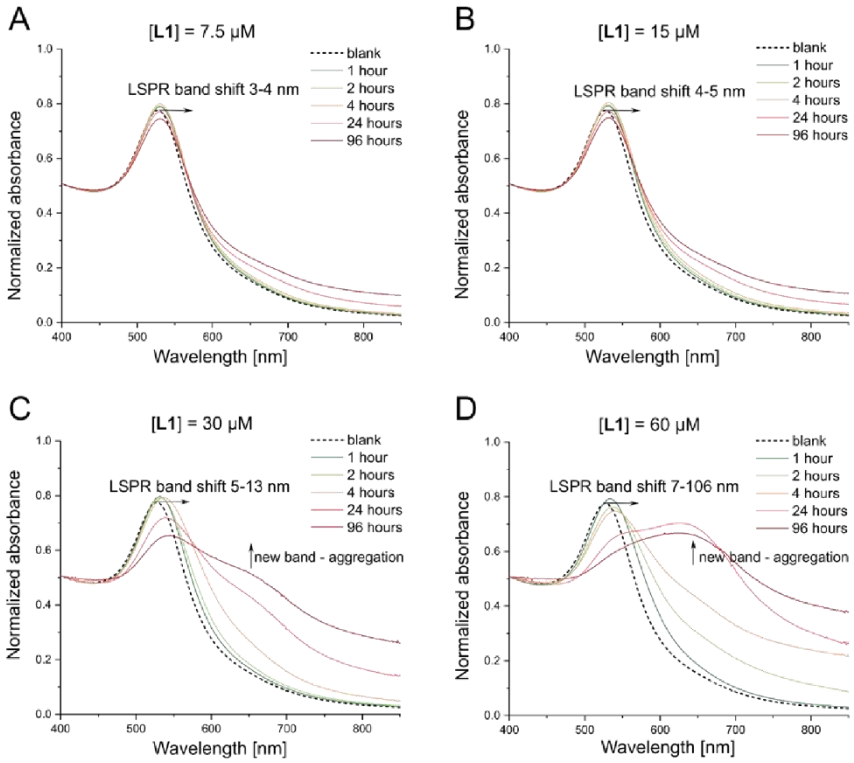

Figure S12. Time-resolved UV-Vis spectra of gold nanoparticles solution (0.25 mM) in toluene upon addition of 7.5 µM (**A**),15 µM (**B**), 30 µM (**C**), 60 µM (**D**) solution of **L1** in toluene. All spectra were normalized at 400 nm to facilitate comparison.

Morphology and Size Determination of Gold Nanoparticles

DLS measurements:

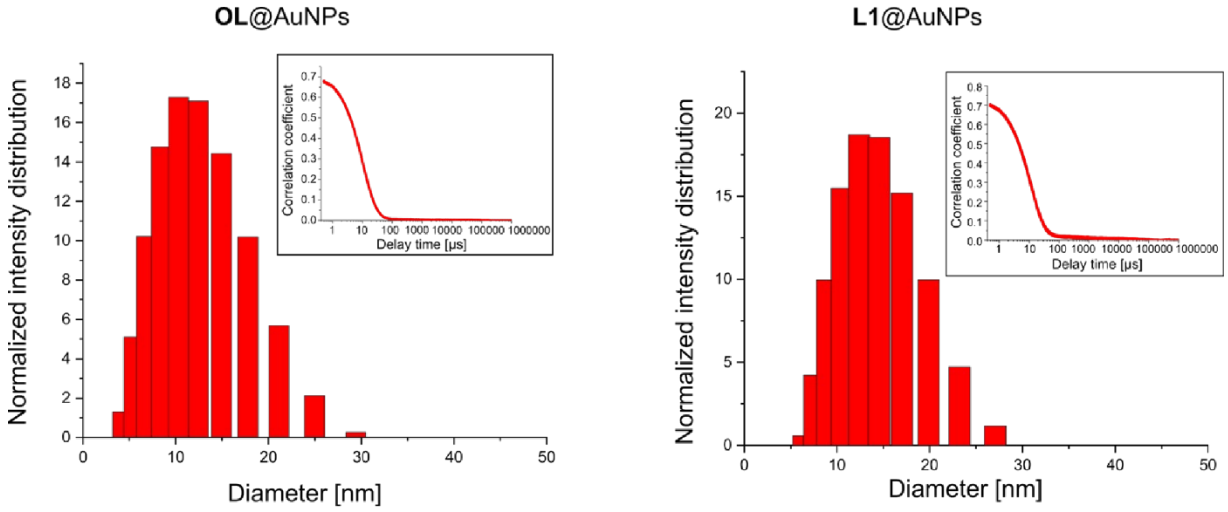

Figure S13. Representative dynamic light scattering (DLS) measurements of gold nanoparticles in toluene solution (0.25 mM) capped with oleylamine (left) showing an average hydrodynamic diameter 14.30 ± 4.38 nm (PdI: 0.186; calculated for n = 5 measurements) and gold nanoparticles in toluene solution (0.25 mM) capped with **L1** (right) showing an average hydrodynamic diameter 15.45 ± 4.26 nm (PdI: 0.243; calculated for n = 5 measurements).

TEM measurements:

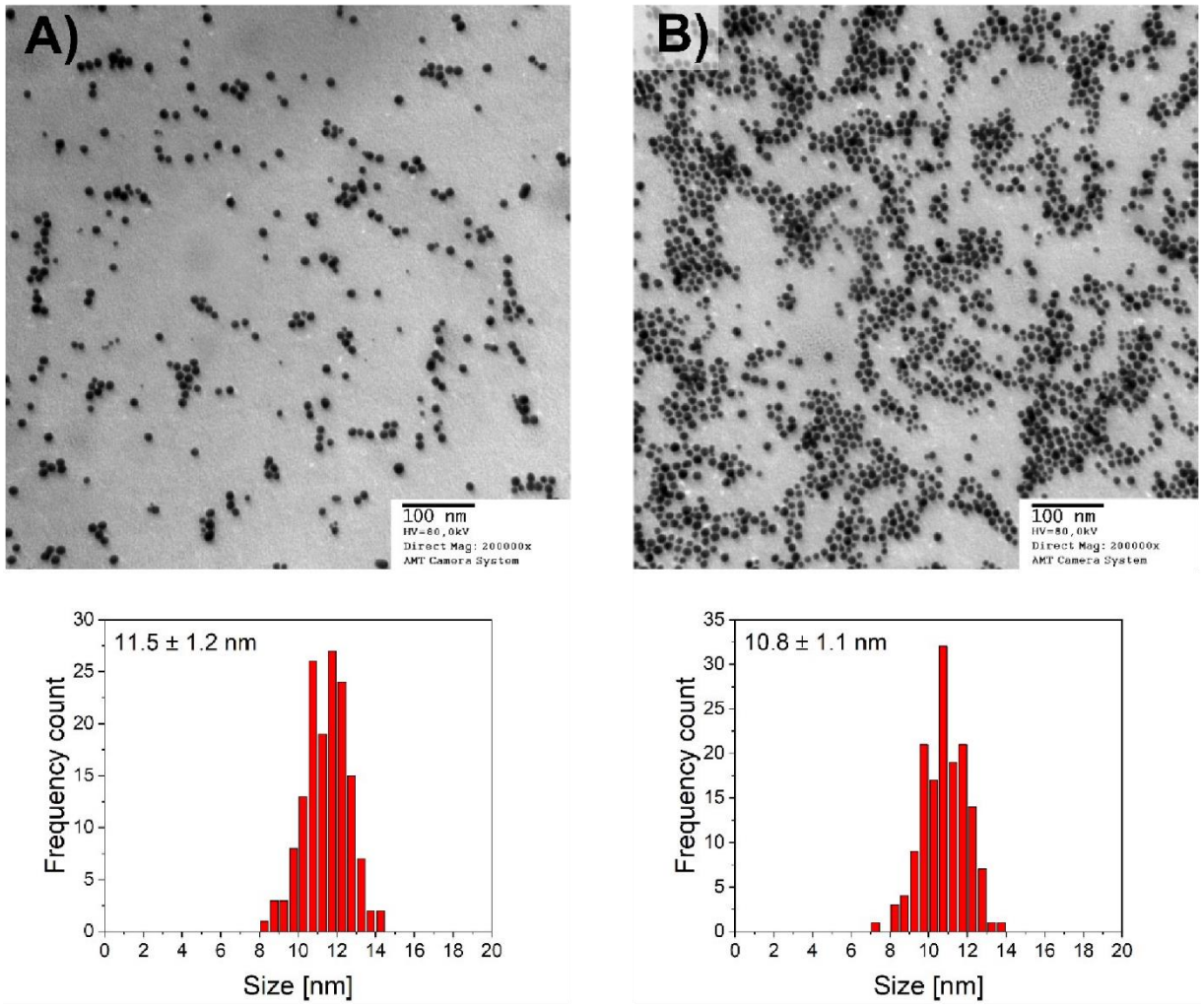

Figure S14. Representative transmission electron microscopy (TEM) images of gold nanoparticles capped by oleylamine (**A**) showing spherical, relatively monodispersed nanoparticles with mean diameter 11.4 ± 1.3 nm, n = 150; and gold nanoparticles capped by ligand **L1** (**B**) showing spherical nanoparticles with mean diameter 10.8 ± 1.1 nm, n = 150.

Sensing metal cations– Cu^{2+}, Ni^{2+}, Fe^{3+}

ICP-MS evaluation of Au content in L1@AuNPs dispersion used for sensing experiments

Sample preparation: 3.5 mL of **L1**@AuNPs dispersion was evaporated under reduced pressure to dryness. To the resulting solid, 1 mL of aqua regia was added and the volume was adjusted to 5 mL with Milli-Q water. The sample for ICP-MS measurement was appropriately diluted. The molar concentration of Au dispersion used for sensing experiments was calculated as 0.246 mM from ICP-MS results (Table S1) following the concentration calculated from UV-vis spectroscopy, 0.25mM.

Table S1. Concentration of Au in **L1**@AuNPs dispersion used for sensing experiments determined by ICP-MS (c = concentration; SD = standard deviation; CV = coefficient of variation).

dilution	c [ug/L]	SD [ug/L]	CV [%]
1000	33 955	246	0.72

General procedure for sensing experiments:

Limit of detection: To 2 mL of gold nanoparticles (in toluene, ~0.25 mM in terms of gold metal) different amounts (20-222 µL, 0.1 mM stock solutions) of metal salts were added. All spectra were measured at room temperature.

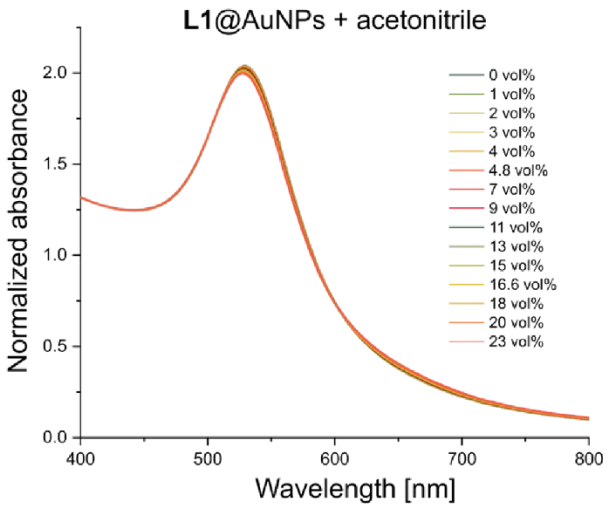

Figure S15. UV-Vis spectra of **L1**@AuNPs upon addition of acetonitrile up to 23 vol%. All spectra were normalized at 400 nm to facilitate comparison.

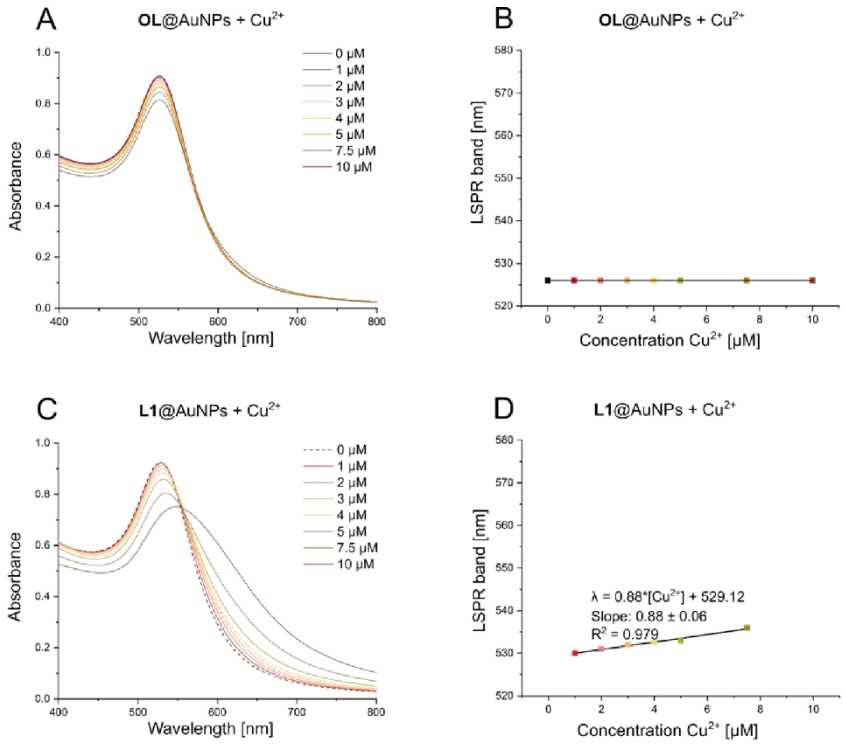

Figure S16. **A** blank experiment: UV-vis spectra of **OL**@AuNPs in toluene upon the addition of $Cu(NO_3)_2$ in acetonitrile; **B** blank experiment: SPR band shift depending on concentration of Cu^{2+} salt; **C** UV-vis spectra of **L1**@AuNPs in toluene upon the addition of $Cu(NO_3)_2$ in acetonitrile; **D** LSPR band shift depending on concentration of Cu^{2+} salt in linear range.

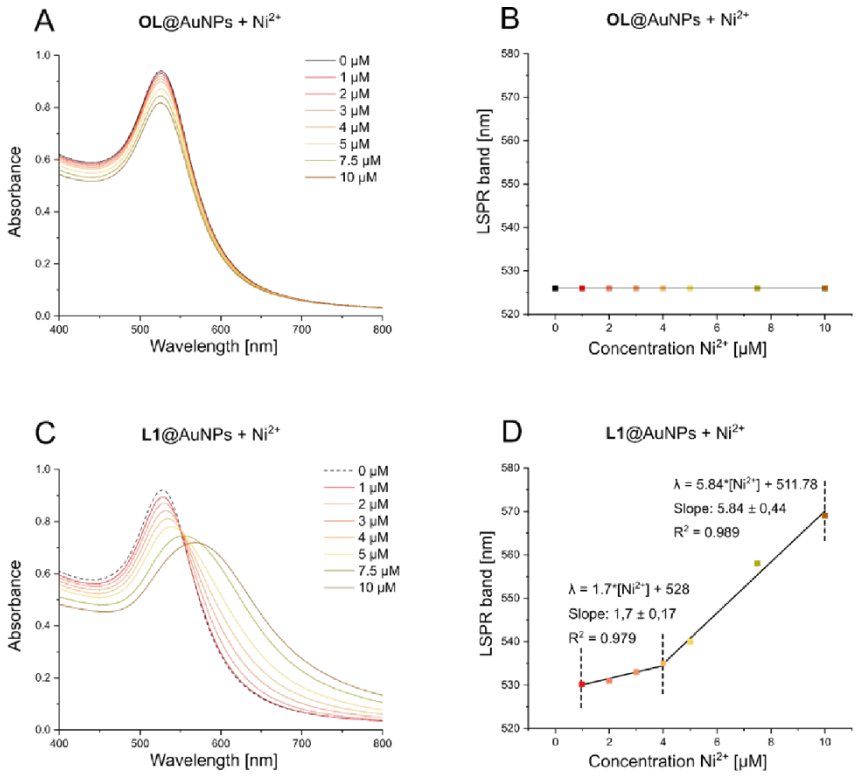

Figure S17. A blank experiment: UV-vis spectra of **OL**@AuNPs in toluene upon increment addition of $Ni(NO_3)_2$ in acetonitrile; **B** blank experiment: SPR band shift depending on concentration of Ni^{2+} salt; **C** UV-vis spectra of **L1**@AuNPs in toluene upon increment addition of $Ni(NO_3)_2$ in acetonitrile; **D** LSPR band shift depending on concentration of Ni^{2+} salt in linear range.

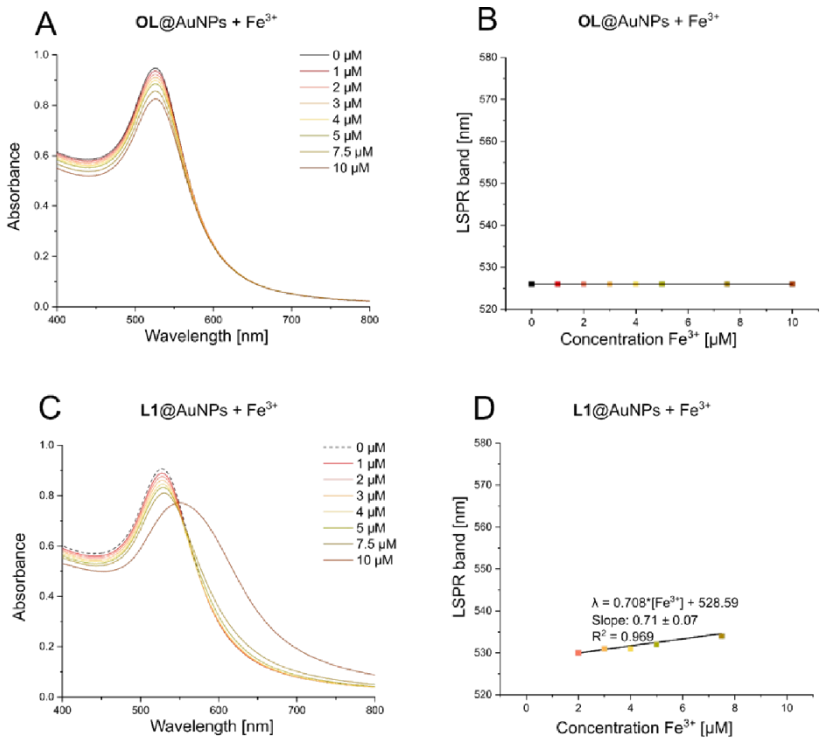

Figure S18. **A** blank experiment: UV-vis spectra of **OL**@AuNPs in toluene upon increment addition of $Fe(NO_3)_3$ in acetonitrile; **B** blank experiment: SPR band shift depending on concentration of Fe^{3+} salt; **C** UV-vis spectra of **L1**@AuNPs in toluene upon increment addition of $Fe(NO_3)_3$ in acetonitrile; **D** LSPR band shift depending on concentration of Fe^{3+} salt in linear range.

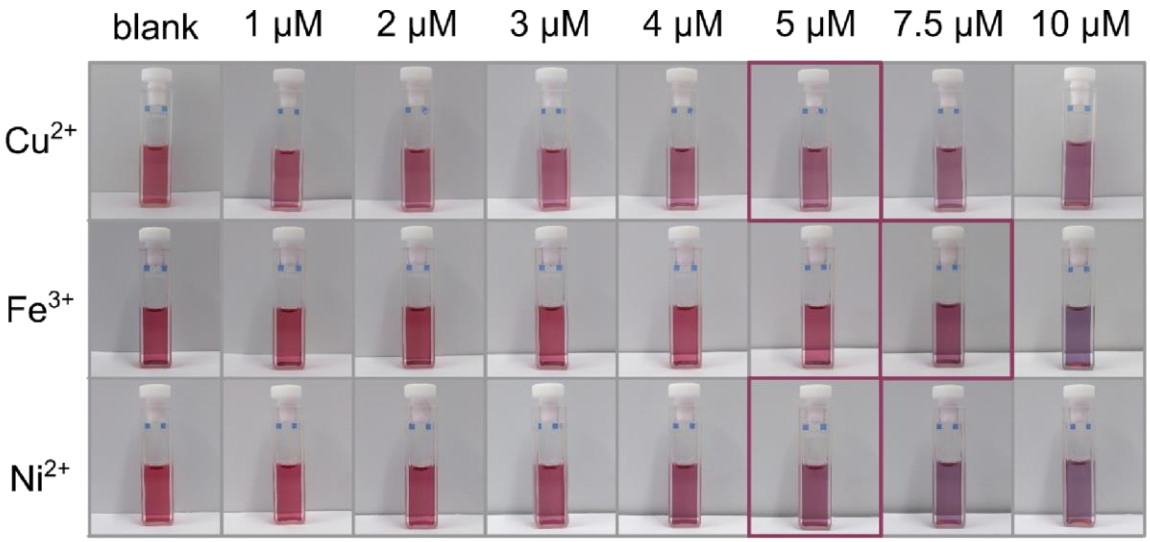

Figure S19. Photographs of **L1**@AuNPs upon incremental addition of transition metal salt solution. Highlighted photographs correspond to the concentration in which visible colour change was noted.

Table S2. Calculated limit of detection (LoD) of **L1**@AuNPs

Analyte	**LoD[13]**	**Linear range [μM]**	**Calibration equation [y = $LSPR_{max}$, x = μM]**	**R^2**
Fe^{3+}	11.2	2-7.5	y = 0.708x + 528.59	0.969
Cu^{2+}	9.0	1-7.5	y = 0.88x + 529.12	0.979
Ni^{2+}	-	1-4	y = 1.7x + 528	0.979
	1.4	4-10	y = 5.84x + 511.78	0.989

Real sample analysis

Synthesis of PDE472 intermediate

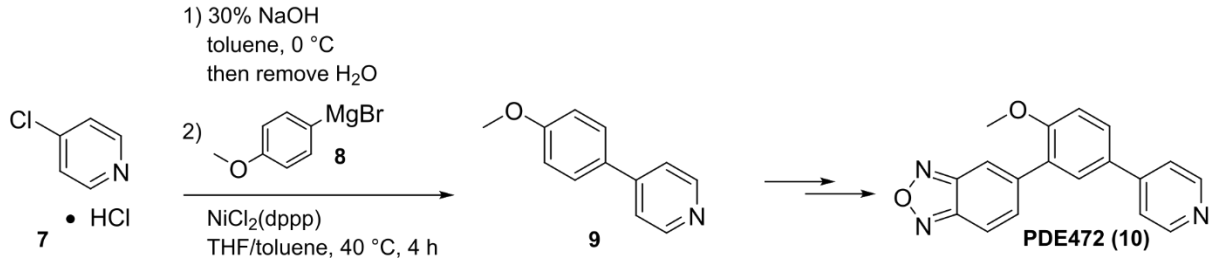

Scheme 4. Synthesis of PDE472 intermediate, via nickel catalysed Kumada coupling[14]

4-(4-Methoxyphenyl)pyridine 9: The intermediate 9 was prepared on a laboratory scale according to the reported procedure.[14]

In detail: 4-bromoanisole (1.5 g, 8.06 mmol) in toluene (1.13 mL) was slowly added in a dropwise manner to Mg turnings (210 mg, 8.62 mmol) and iodine (sublimated, 1.9 mg) activated by heat in THF (3 mL) at 35 °C. After the reaction was initiated, the whole solution was added at such a rate to maintain the temperature of 35 °C. After 3 hours at 45 °C, the mixture was cooled and used for the coupling reaction.

30% NaOH (aqueous solution, 1.05 g, 7.87 mmol) was added to a stirred solution of **7** (1.125 g, 7.5 mmol) in toluene (3.75 mL) and water (4.13 mL) at 0 °C, at such rate that the mixture did not reach more than 5 °C. After another 10 min, the layers were separated and the organic layer was heated under reflux (150 mbar, 50 °C) using a Dean-Stark water trap, for azeotropic water removal. [Safety remark: removal of toluene by distillation can lead to a strongly exothermic autopolymerisation of the free base of **7**]. $NiCl_2$(dppp) (5.6 mg, 0.01 mmol) was then added to the dried base solution of **7** in toluene at ambient temperature. Solution of **8** prepared in the first step

was added dropwise to keep the initial exothermic reaction below 45 °C. After 3 hours at 45 °C reaction was completed, and the mixture was cooled to ambient temperature. Next, a solution of citric acid (1.31 g) in water (2.6 mL) and concentrated HCl (0.38 mL) was prepared, and the reaction mixture was added dropwise over several minutes. The flask was rinsed with toluene (1.13 mL), water (2.63 mL) and concentrated HCl (0.38 mL) and the fractions were added to the reaction mixture. The mixture was then heated to 30 °C and the layers were separated. ***The organic layer, which represents the organic waste from the reaction was put aside for ICP-MS and sensing experiments.*** To the water layer, containing the hydrochloride of **9**, toluene (5.6 mL) and 30 % NaOH (aqueous solution, 3 mL) were added. Layers were separated and the toluene phase was evaporated to dryness, under reduced pressure to yield crude **9**. Spectral data were consistent with the literature.[15] ^{1}H NMR (600 MHz, $CDCl_3$): δ 3.87 (s, 3H), 7.01 (d, 2H, J = 8.7 Hz), 7.47 (d, 2H, J = 6.2 Hz), 7.60 (d, 2H, J = 8.7 Hz), 8.62 (d, 2H, J = 6.2 Hz).

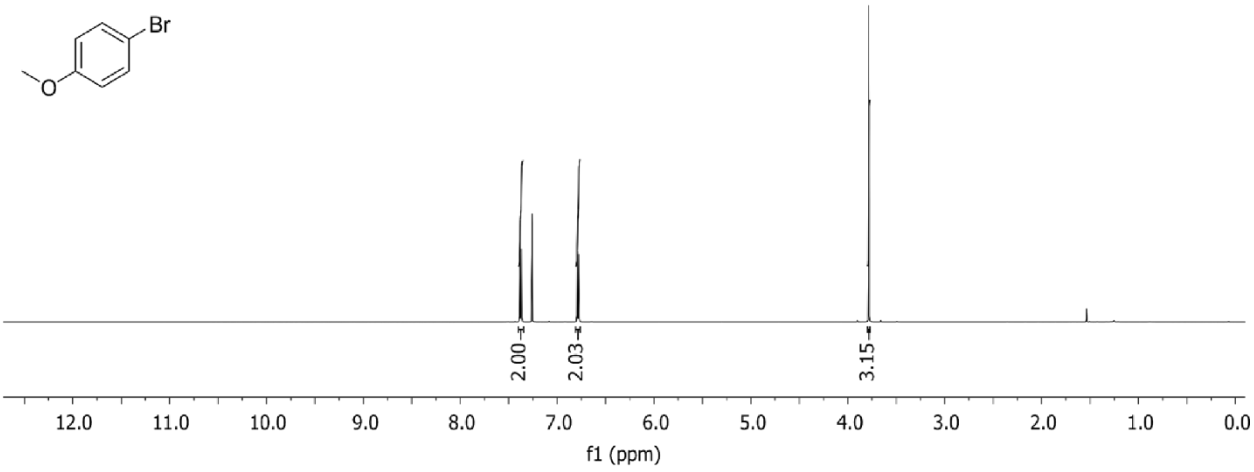

Figure S20. ^{1}H NMR of 4-bromoanisole – substrate to the Kumada coupling leading to **9**, PDE472 intermediate.

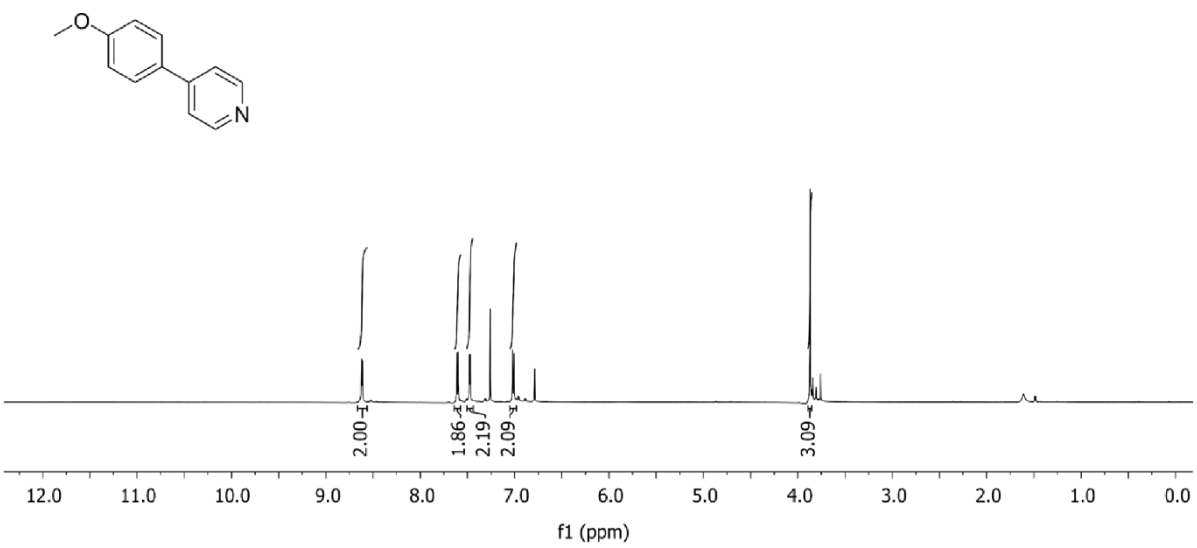

Figure S21. ^{1}H NMR of crude PDE472 intermediate **9**.

Sensing – organic waste sample (Kumada coupling)

Procedure: To 2 mL of gold nanoparticles (in toluene, 0.25 mM in terms of gold metal) different amounts (20-50 µL) of organic waste were added. All spectra were measured at room temperature.

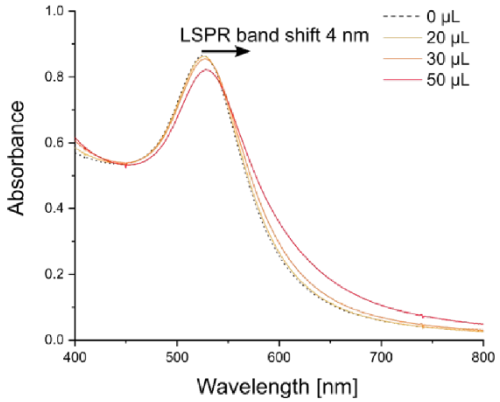

Figure S22. UV-Vis spectra of **L1**@AuNPs upon addition of organic waste.

ICP-MS evaluation of Ni content in organic waste

Sample preparation: 300 µL of organic waste was evaporated under reduced pressure to dryness and was additionally dried under reduced pressure. 50 mg (from resulting 57 mg) of the dried organic waste was mineralized in the following way: The sample digestion was carried out in a microwave-assisted digestion system (Ethos One, Milestone Srl, Italy). About 50 mg of the sample was placed in quartz vessels with 2 mL 65% nitric acid. The digestion program was performed in 3 stages: 20 minutes ramp time to 200 °C, 30 minutes hold time at 200 °C and cooling down for 60 min. The final step in sample preparation was the quantitative transfer of the digested sample to Falcon tubes and 1000-fold dilution with 1% HNO_3.

Evaluation of concentration in organic waste used in sensing experiments: Based on the ICP-MS results (Table S3), Ni^{2+} concentration 44.44 µg/g in 50 mg of solid sample corresponds to 0.143 mM of Ni^{2+} ions in the toluene solution before mineralization. That represents concentration of the solution used for sensing experiments. Adding 50 µL of this stock solution into 2000 µL of **L1**@AuNPs in toluene, result in 3.49 µM Ni^{2+} ion solution.

Table S3. Evaluation of Ni content in organic waste sample determined by ICP-MS (m = weight; c = concentration; SD = standard deviation; CV = coefficient of variation).

m [g]	c [ug/g]	SD [ug/g]	CV [%]
0.050	44.44	0.68	1.5

Time	Sensor	Analyte	Reference
10 min	Phyto extract GNP	Cd(II)	[16]
NR (rapid)	Schiff base GNP	Hg(II)	[17]
10 sec	Schiff base GNP	Al(III)	[18]
20 sec	Nitriloacetic acid and His GNP	Ni(II)	[19]
1 min	Cys GNP	Sc(III)	[20]
NR	Schiff base GNP	Fe(III)	[21]
NR (rapid)	Vitamin B6 GNP	Cr(III)	[22]
20 min	Mo hydrogel	As(III)	[23]
6 min	GSH and Cys Silver nanoplates	Ni(II)	[24]
95 min	Schiff base	Fe(III)	[25]
10 min	PAM AgBr NCs	Pb(II), Cu(II)	[26]
1 min	Peptide GNP	Co(II), Hg(II), Pb(II), Pd(II), Pt(II)	[27]

Table S4. Response time for colorimetric sensors.

NR = not reported

References:

1. R. J. Stokes, A. Macaskill, J. A. Dougan, P. G. Hargreaves, H. M. Stanford, W. E. Smith, K. Faulds and D. Graham, *Chem Commun,* 2007, DOI: 10.1039/b705873j, 2811-2813.
2. N. E. Pollok, C. Rabin, L. Smith and R. M. Crooks, *Bioconjug Chem*, 2019, **30**, 3078-3086.
3. *USA Pat.,* US2008/286607, 2008.
4. A. J. Fugard, B. K. Thompson, A. M. Slawin, J. E. Taylor and A. D. Smith, *Org Lett*, 2015, **17**, 5824-5827.
5. A. M. Johnson, M. C. Young, X. Zhang, R. R. Julian and R. J. Hooley, *J Am Chem Soc*, 2013, **135**, 17723-17726.
6. M. R. Baumgartner, H. Schmalle and E. Dubler, *Inorganica Chim Acta*, 1996, **252**, 319-331.
7. H. Sigel, B. Prijs and D. B. McCormick, *J Inorg Nucl Chem*, 1978, **40**, 1678-1680.
8. X. Huang, A. J. Shumski, X. Zhang and C. W. Li, *J Am Chem Soc*, 2018, **140**, 8918-8923.
9. V. Montes-García, S. Rodal-Cedeira, M. J. Cordero-Ferradás, B. Gómez, L. García-Río, I. Pastoriza-Santos and J. Pérez-Juste, *Isr J Chem*, 2018, **58**, 1251-1260.
10. M. J. Hostetler, J. E. Wingate, C.-J. Zhong, J. E. Harris, R. W. Vachet, M. R. Clark, J. D. Londono, S. J. Green, J. J. Stokes, G. D. Wignall, G. L. Glish, M. D. Porter, N. D. Evans and R. W. Murray, *Langmuir*, 1998, **14**, 17-30.
11. X. Liu, M. Atwater, J. Wang and Q. Huo, *Colloids Surf B Biointerfaces*, 2007, **58**, 3-7.

12. J. C. Love, L. A. Estroff, J. K. Kriebel, R. G. Nuzzo and G. M. Whitesides, *Chem Rev*, 2005, **105**, 1103-1169.
13. X. Jia, D. Chao, L. He, H. Liu, T. Zheng, C. Zhang and C. Wang, *Macromol Res*, 2011, **19**, 1127-1133.
14. P. W. Manley, M. Acemoglu, W. Marterer and W. Pachinger, *Org Process Res Dev*, 2003, **7**, 436-445.
15. S. Panda, A. Coffin, Q. N. Nguyen, D. J. Tantillo and J. M. Ready, *Angew Chem Int Ed Engl*, 2016, **55**, 2205-2209.
16. K. Singh, V. Kumar, B. Kukkar, K. H. Kim and T. R. Sharma, *Int J Environ Sci Technol*, 2021, DOI: 10.1007/s13762-021-03331-0.
17. F. Amourizi, K. Dashtian, M. Ghaedi and B. Hosseinzadeh, *Anal Methods*, 2021, **13**, 2603-2611.
18. P. Huang, J. Li, X. Liu and F. Wu, *Microchim Acta*, 2015, **183**, 863-869.
19. Z. Krpetic, L. Guerrini, I. A. Larmour, J. Reglinski, K. Faulds and D. Graham, *Small*, 2012, **8**, 707-714.
20. H.-H. Deng, K.-Y. Huang, Q.-H. Fang, Y.-P. Lv, S.-B. He, H.-P. Peng, X.-H. Xia and W. Chen, *Sens Actuators B Chem*, 2020, **311**, 127925.
21. A. A. Jimoh, A. Helal, M. N. Shaikh, M. Abdul Aziz, Z. H. Yamani, A. Al-Ahmed and J.-P. Kim, *J Nanomater*, 2015, **2015**, 1-7.
22. Y. Upadhyay, S. Bothra, R. Kumar and S. K. Sahoo, *ChemistrySelect*, 2018, **3**, 6892-6896.
23. J. Das and P. Sarkar, *Environ Sci Water Res Technol*, 2016, **2**, 693-704.
24. T. Kiatkumjorn, P. Rattanarat, W. Siangproh, O. Chailapakul and N. Praphairaksit, *Talanta*, 2014, **128**, 215-220.
25. T.-B. Wei, P. Zhang, B.-B. Shi, P. Chen, Q. Lin, J. Liu and Y.-M. Zhang, *Dyes Pigm*, 2013, **97**, 297-302.
26. A. K. Yetisen, Y. Montelongo, M. M. Qasim, H. Butt, T. D. Wilkinson, M. J. Monteiro and S. H. Yun, *Anal Chem*, 2015, **87**, 5101-5108.
27. J. M. Slocik, J. S. Zabinski, Jr., D. M. Phillips and R. R. Naik, *Small*, 2008, **4**, 548-551.

Declaration letters of co-authors

Poznań, 20/09/2023

mgr. Miroslava Čonková
Institute of Organic Chemistry,
Karlsruhe Institute of Technology (KIT),
Fritz-Haber-Weg 6,
76131 Karlsruhe

DECLARATION

I hereby declare that in following papers:

[A1] Miroslava Čonková, Wojciech Drożdż, Zygmunt Miłosz, Piotr Cecot, Jack Harrowfield, Mikołaj Lewandowski, Artur R. Stefankiewicz* *Influencing prototropy by metal ion coordination: supramolecular transformation of a dynamer into a Zn-based toroidal species*, Journal of Materials Chemistry C, **2021**, *9*, 3065-3069.

[A2] Miroslava Čonková#, Verónica Montez-Garcia#, Marcin Konopka, Artur Cieselski*, Paolo Samori*, Artur R. Stefankiewicz* *Schiff base caped gold nanoparticles for transition metal cations sensing in organic media*, Chemical Communications, **2022**, *58 (38)*, 5773-5776.

[A3] Filip Perlitius, Anna Walczak, Miroslava Čonková, Grzegorz Markiewicz, Jack Harrowfield, Artur R. Stefankiewicz* *Dimeric capsule vs. columnar polymer: structural factors determining the aggregation behavior of amino acid-functionalized BTA derivatives in solution and in the solid-state*, Journal of Molecular Liquids, **2022**, *367*, 120511.

my own contribution includes:
in [A1, A2]

- synthesis of target compounds
- characterization of target compounds using various spectroscopy methods
- acquiring experimental data, data analysis, and interpretation of results
- co-interpreting results acquired by co-authors and services
- co-creating the concept of the study
- preparing the first drafts of manuscripts, including all graphics
- preparing supplementary information for manuscripts, including graphics
- taking part in the revision of the manuscript
- taking part in correspondence with editors of journals and referees

in [A3]:

- co-creating the concept of the study
- planning experiments
- taking part in revision of the manuscript

mgr. Miroslava Čonková

Prof. dr hab. Artur R. Stefankiewicz
Zakład Syntezy Nanostruktur Funkcjonalnych
Wydział Chemii
Uniwersytet im. Adama Mickiewicza w Poznaniu
Uniwersytetu Poznańskiego 8,
61-614 Poznań

Poznań, 27.09.2023

OŚWIADCZENIE

Niniejszym oświadczam, że w poniższych artykułach:

A1. [1] Miroslava Čonková, Wojciech Drożdż, Zygmunt Miłosz, Piotr Cecot, Jack Harrowfield, Mikołaj Lewandowski, Artur R. Stefankiewicz* *Influencing prototropy by metal ion coordination: supramolecular transformation of a dynamer into a Zn-based toroidal species,* Journal of Materials Chemistry C, **2021**, *9*, 3065-3069.
IF = 7.393

A2. Miroslava Čonková[#], Verónica Montez-Garcia[#], Marcin Konopka, Artur Cieselski*, Paolo Samori*, Artur R. Stefankiewicz* *Schiff base caped gold nanoparticles for transition metal cations sensing in organic media*, Chemical Communications, **2022**, *58 (38)*, 5773-5776.
IF = 6.065

byłem bezpośrednim opiekunem naukowym i promotorem mgr Miroslavy Conkovej, a mój udział obejmował:

- opracowanie koncepcji pracy,
- współudział w interpretacji i analizie danych,
- współudział w przygotowaniu ostatecznej wersji manuskryptu oraz korespondencji z edytorem i recenzentami.

Prof. dr hab. Artur R. Stefankiewicz

Poznań, 21/09/2023

mgr Piotr Cecot
cecot.piotr@gmail.com

DECLARATION

I hereby declare that in the following paper:

Miroslava Čonková, Wojciech Drożdż, Zygmunt Miłosz, Piotr Cecot, Jack Harrowfield, Mikołaj Lewandowski, Artur R. Stefankiewicz* *Influencing prototropy by metal ion coordination: supramolecular transformation of a dynamer into a Zn-based toroidal species,* Journal of Materials Chemistry C, **2021**, *9*, 3065-3069.

my own contribution includes:

- Molecular Modeling of Monomeric Species and Polymeric Assemblies
- Structural Characterization of Optimized Molecular Structures
- Energy and Shape Calculations of Frontal (HOMO-LUMO) Orbitals
- Integration of Molecular Models with STM Images through Frontal Orbital Analysis

21.09.23 .....

mgr Piotr Cecot

Poznań, 21/09/2023

dr Wojciech Drożdż
Zakład Syntezy Nanostruktur Funkcjonalnych,
Uniwersytet im. Adama Mickiewicza w Poznaniu,
Uniwersytetu Poznańskiego 8,
61-614 Poznań

DECLARATION

I hereby declare that in the following paper:

Miroslava Čonková, Wojciech Drożdż, Zygmunt Miłosz, Piotr Cecot, Jack Harrowfield, Mikołaj Lewandowski, Artur R. Stefankiewicz* *Influencing prototropy by metal ion coordination: supramolecular transformation of a dynamer into a Zn-based toroidal species,* Journal of Materials Chemistry C, **2021**, *9*, 3065-3069.

my own contribution includes:

- Synthesis and characterization of selected compounds
- co-writing the manuscript

Wojciech Drożdż

……..
dr Wojciech Drożdż

Strasbourg, 21/09/2023

Prof. Jack M. Harrowfield
Institut de Science et d'Ingénierie Supramoléculaires,
Université de Strasbourg,
8 allée Gaspard Monge,
67083 Strasbourg

DECLARATION

I hereby declare that in following papers:

[A1] Miroslava Čonková, Wojciech Drożdż, Zygmunt Miłosz, Piotr Cecot, Jack Harrowfield, Mikołaj Lewandowski, Artur R. Stefankiewicz* *Influencing prototropy by metal ion coordination: supramolecular transformation of a dynamer into a Zn-based toroidal species,* Journal of Materials Chemistry C, **2021**, *9*, 3065-3069.

[A3] Filip Perlitius, Anna Walczak, Miroslava Čonková, Grzegorz Markiewicz, Jack Harrowfield, Artur R. Stefankiewicz* *Dimeric capsule vs. columnar polymer: structural factors determining the aggregation behavior of amino acid-functionalized BTA derivatives in solution and in the solid-state*, Journal of Molecular Liquids, **2022**, *367,* 120511.

my contributions involved:

- Assistance in the analysis of the coordination chemistry involved
- Co-interpreting and description of crystallographic data involved
- Assistance in the preparation of the final text

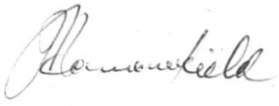

.....
Prof. Jack M. Harrowfield

Poznań, 26.09.2023

Dr hab. Mikołaj Lewandowski, Prof. UAM
Centrum NanoBioMedyczne
Uniwersytet im. Adama Mickiewicza w Poznaniu
Wszechnicy Piastowskiej 3
61-614 Poznań
Tel.: +48737474700
E-mail: lewandowski@amu.edu.pl

OŚWIADCZENIE WSPÓŁAUTORA PUBLIKACJI NAUKOWEJ

Oświadczam, że w pracy:

Miroslava Čonková, Wojciech Drożdż, Zygmunt Miłosz, Piotr Cecot, Jack Harrowfield, Mikołaj Lewandowski, Artur R. Stefankiewicz*, *Influencing prototropy by metal ion coordination: supramolecular transformation of a dynamer into a Zn-based toroidal species,* Journal of Materials Chemistry C 9 (2021) 3065–3069

mój oryginalny wkład był związany z badaniami realizowanymi przy użyciu skaningowej mikroskopii tunelowej (STM) i uwzględniał:

- nadzór merytoryczny nad pomiarami STM;
- wsparcie realizacji pomiarów STM;
- częściową analizę i interpretację wyników pomiarów STM;
- współudział w dyskusji wyników STM ze współautorami;
- współudział w przygotowywaniu fragmentów publikacji dotyczących przebiegu eksperymentów STM i interpretacji uzyskanych wyników;
- zgłoszenie uwag do całości manuskryptu.

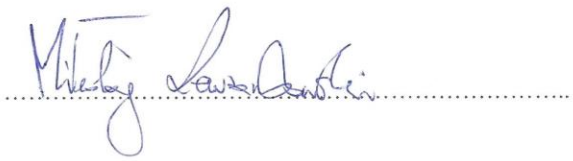

Poznań, 21/09/2023

dr Zygmunt Miłosz
Centrum NanoBioMedyczne,
Uniwersytet im. Adama Mickiewicza w Poznaniu,
Wszechnicy Piastowskiej 3,
61-614 Poznań

DECLARATION

I hereby declare that in the following paper:

Miroslava Čonková, Wojciech Drożdż, Zygmunt Miłosz, Piotr Cecot, Jack Harrowfield, Mikołaj Lewandowski, Artur R. Stefankiewicz* *Influencing prototropy by metal ion coordination: supramolecular transformation of a dynamer into a Zn-based toroidal species,* Journal of Materials Chemistry C, **2021**, *9*, 3065-3069.

my own contribution includes:

- STM measurements,
- STM data analysis.

Zygmunt Miłosz

dr Zygmunt Miłosz

Brussels, 21/09/2023

Dr. Marcin Konopka
Engineering of Molecular NanoSystems
Université libre de Bruxelles,
Avenue Franklin Roosevelt 50,
1050 Brussels

DECLARATION

I hereby declare that in the following paper:

Miroslava Čonková[#], Verónica Montez-Garcia[#], Marcin Konopka, Artur Cieselski*, Paolo Samori*, Artur R. Stefankiewicz* *Schiff base caped gold nanoparticles for transition metal cations sensing in organic media*, Chemical Communications, **2022**, *58 (38)*, 5773-5776.

my own contribution includes:

- Development of a method for the synthesis of ligand **L1** from lipoic acid.
- Ligand **L1** synthesis and characterization.

Marcin Konopka

Dr. Marcin Konopka

Dr. Verónica Montes García
Laboratoire de Nanochimie
8, Allée Gaspard Monge, BP 70028
67083 STRASBOURG Cedex, France

Strasbourg, 21th September 2023

DECLARATION

I hereby declare that in the following paper:

Miroslava Čonková[#], Verónica Montez-Garcia[#], Marcin Konopka, Artur Cieselski*, Paolo Samori*, Artur R. Stefankiewicz* *Schiff base caped gold nanoparticles for transition metal cations sensing in organic media*, Chemical Communications, **2022**, *58 (38)*, 5773-5776.

My own contribution includes:

- Investigation
- Data curation
- Manuscript writing

Verónica Montes

Verónica Montes García

Tél. : +33 3 68 85 51 87 montesgarcia@unistra.fr

Dr. Artur Ciesielski
Directeur de recherche
Nanochemistry Laboratory
8, Allée Gaspard Monge
F - 67000 Strasbourg, France

Prof. Artur Ciesielski
Visiting Professor
Center for Advanced Technology,
Adam Mickiewicz University, Uniwersytetu
Pozna n´skiego 10, 61-614 Poznan´, Poland

Strasbourg, 21th September 2023

DECLARATION

I hereby declare that in the following paper:

Miroslava Čonková#, Verónica Montez-Garcia#, Marcin Konopka, Artur Cieselski*, Paolo Samori*, Artur R. Stefankiewicz* *Schiff base caped gold nanoparticles for transition metal cations sensing in organic media*, Chemical Communications, **2022**, *58 (38)*, 5773-5776.

My own contribution includes:

- Conceptualization
- Manuscript writing

Artur Ciesielski

Tél. : +33 3 68 85 51 41 Fax : +33 3 68 85 51 61 ciesielski@unistra.fr

ISIS
Institut de Science et d'Ingénierie Supramoléculaires

Université de Strasbourg

cnrs

Professeur Paolo SAMORI
Laboratoire de Nanochimie
8, Allée Gaspard Monge, BP 70028
67083 STRASBOURG Cedex, France

Strasbourg, 21th September 2023

DECLARATION

I hereby declare that in the following paper:

Miroslava Čonková[#], Verónica Montez-Garcia[#], Marcin Konopka, Artur Cieselski*, Paolo Samori*, Artur R. Stefankiewicz* *Schiff base caped gold nanoparticles for transition metal cations sensing in organic media*, Chemical Communications, **2022**, *58 (38)*, 5773-5776.

My own contribution includes:

- Conceptualization
- Manuscript writing

Paolo Samorì

Tél. : +33 3 68 85 51 60 Fax : +33 3 68 85 51 61 samori@unistra.fr

Poznań, 28/09/2023

Dr Anna Walczak
Zakład Syntezy Nanostruktur Funkcjonalnych,
Uniwersytet im. Adama Mickiewicza w Poznaniu,
Uniwersytetu Poznańskiego 8,
61-614 Poznań

DECLARATION

I hereby declare that in the following paper:

Filip Perlitius, Anna Walczak, Miroslava Čonková, Grzegorz Markiewicz, Jack Harrowfield, Artur R. Stefankiewicz* *Dimeric capsule vs. columnar polymer: structural factors determining the aggregation behavior of amino acid-functionalized BTA derivatives in solution and in the solid-state*, Journal of Molecular Liquids, **2022**, *367,* 120511.

my own contribution includes:

- Diffractometric measurements of all crystals
- Solution and description of crystal structures

Walczak Anna

.....

Poznań, 28/09/2023

Filip Perlitius
Zakład Syntezy Nanostruktur Funkcjonalnych,
Uniwersytet im. Adama Mickiewicza w Poznaniu,
Uniwersytetu Poznańskiego 8,
61-614 Poznań

DECLARATION

I hereby declare that in the following paper:

Filip Perlitius, Anna Walczak, Miroslava Čonková, Grzegorz Markiewicz, Jack Harrowfield, Artur R. Stefankiewicz* *Dimeric capsule vs. columnar polymer: structural factors determining the aggregation behavior of amino acid-functionalized BTA derivatives in solution and in the solid-state*, Journal of Molecular Liquids, **2022**, *367,* 120511.

my own contribution includes:

- synthesis of all target compounds
- characterization of all target compounds using various spectroscopy methods
- acquiring experimental data, data analysis, and interpretation of results co-interpreting results acquired by co-authors and services
- co-creating the concept of the study
- preparing the first drafts of manuscripts, including all graphics
- preparing supplementary information for manuscripts, including graphics
- taking part in the revision of the manuscript

Filip Perlitius

Poznań, 01/10/2023

Dr Grzegorz Markiewicz
Center for Advanced Technology
Adam Mickiewicz University
Uniwersytetu Poznańskiego 10
61-614, Poznań, Poland

DECLARATION

I hereby declare that in the following paper:

Filip Perlitius, Anna Walczak, Miroslava Čonková, Grzegorz Markiewicz, Jack Harrowfield, Artur R. Stefankiewicz* *Dimeric capsule vs. columnar polymer: structural factors determining the aggregation behavior of amino acid-functionalized BTA derivatives in solution and in the solid-state*, Journal of Molecular Liquids, **2022**, *367,* 120511.

my own contribution includes:

- design and acquisition of the NMR experiments (thermodynamics, DOSY)
- design of the FT-IR experiments
- Co-interpreting and data analysis
- Co-authoring and revision of the manuscript text

Dr Grzegorz Markiewicz